Microwave control of atomic motion in a spin dependent optical lattice

Dissertation
zur Erlangung des Doktorgrades (Dr. rer. nat.)
der Mathematisch-Naturwissenschaftlichen Fakultät
der Rheinischen Friedrich-Wilhelms-Universität Bonn

vorgelegt von
Leonid Förster
aus
Astrachan

Bonn (2010)

Angefertigt mit Genehmigung
der Mathematisch-Naturwissenschaftlichen Fakultät
der Rheinischen Friedrich-Wilhelms-Universität Bonn

1. Gutachter: Prof. Dr. Dieter Meschede
2. Gutachter: Prof. Dr. Martin Weitz

Tag der Promotion: 10. Mai 2010

Summary / Zusammenfassung

In this thesis I present my results concerning the coherent control of the quantized motional state of trapped neutral Cesium atoms. This is accomplished using microwave radiation in combination with a spin dependent potential confining the atoms. I present both cooling of atoms close to the motional ground state and the preparation of nonclassical motional states. In total, our apparatus is thus capable to control the spin, the position along the periodic potential and the vibrational state of the atoms.

In chapter 1 I give an overview of the experimental apparatus. Our setup is designed to trap and to store on the order of ten atoms in a one dimensional optical lattice. Fluorescence imaging in conjunction with a microscope lens system is used to determine both the number and the position of the atoms. The spin degree of freedom is manipulated using microwave radiation and the trapping potential allows to shift the atoms to the 'left' or to the 'right' along the potential axis, depending on their spin orientation.

In chapter 2 I discuss the coupling mechanism between the spin and the motional degree of freedom. A microwave spectrum with a slightly displaced lattice exhibits sideband peaks corresponding to a change of the vibrational quantum number. For the full quantitative understanding I compare the experimental results with a theoretical model, which is also used to quantify possible decoherence mechanisms.

Based on this investigations, in chapter 3 I present the results for our ground state cooling scheme, whereby the focuss lies on the peculiarities of our system. A model based on master equations is used to analyze the present cooling limits. In chapter 4, finally, two detection schemes for arbitrary motional states of an atomic ensemble are presented. In particular, they are employed to verify the preparation of nonclassical states.

In meiner Arbeit befasse ich mich mit der Manipulation der quantenmechanischen Ortswellenfunktion von neutralen Cäsiumatomen, die sich wohl lokalisiert in dem Potential einer Dipolfalle befinden. Dazu verwenden wir eine wenig untersuchte Methode, die auf der Kopplung des äußeren Freiheitsgrades an den Spin der Atome mittels Mikrowellenstrahlung in Kombination mit einem spinabhängigen Potential beruht. Insgesamt bietet unser experimenteller Aufbau damit die Kontrolle über den

Spinfreiheitsgrad, über die Position der Atome entlang des periodischen Potentials und über die atomare Ortswellenfunktion in einem einzelnen Potentialtopf.

Kapitel 1 ist der Beschreibung des experimentellen Aufbaus gewidmet. Der Aufbau ist dafür konzipiert worden, etwa zehn Atome in einem eindimensionalen optischen Gitter zu speichern. Die Anzahl der Atome und deren Position entlang der Potentialachse wird durch Abbildung des Fluoreszenzlichts mittels eines Mikroskoplinsensystems bestimmt. Während der atomare Spin mittels Mikrowellenpulse präpariert wird, erlaubt die Dipolfalle den Transport von Atomen nach 'links' oder nach 'rechts', abhängig von deren Spinausrichtung.

In Kapitel 2 wird die Kopplung zwischen dem Spinfreiheitsgrad und dem vibronischen Zustand genauer untersucht. Ein Mikrowellenspektrum in einer Konfiguration mit leicht versetzten spinabhängigen Potentialen weist Seitenbänder auf, die von einem Wechsel der vibronischen Quantenzahl herrühren. Um den Mechanismus quantitativ zu verstehen, vergleiche ich die experimentellen Resultate mit einem theoretischen Modell, was außerdem zur Charakterisierung von Dekohärenzmechanismen verwendet wird.

Basierend auf diesen Untersuchungen beschreibt das Kapitel 3 unser Kühlschema, das wir dazu verwenden Atome in den Grundzustand zu kühlen. Der Schwerpunkt wird dabei auf die Besonderheiten unseres System gelegt. Mithilfe eines Modells, was auf Mastergleichungen basiert, lege ich weiterhin dar, wo derzeitige Limitierungen liegen und wie das Schema erweitert werden kann. In Kapitel 4 schließlich, präsentiere ich Resultate zur Präparation einiger nichtklassischer Bewegungszustände, und deren Detektion mittels zweier verschiedener Methoden.

Publications

Parts of this thesis have been published in the following papers:

1. M. Karski, L. Förster, W. Alt, D. Meschede, A. Widera, *Nearest-Neighbor Detection of Atoms in a 1D Optical Lattice by Fluorescence Imaging*, Phys. Rev. Lett. **102**, 053001 (2009)

2. L. Förster, M. Karski, J. Choi, A. Steffen, W. Alt, D. Meschede, A. Widera, E Montano, J. Lee, W. Rakreungdet, P. Jessen, *Microwave control of atomic motion in optical lattices*, Phys. Rev. Lett. **103**, 233001 (2009)

Table of Contents

Introduction

Full control over a quantum system, or "quantum engineering", is subject of ongoing theoretical and experimental research in quantum optics. Such systems are on the way to serve as quantum simulators for more complex physical phenomena in a well controlled environment [1], and envision quantum information processing in the future [2]. A very active part of the field is based on neutral atoms trapped in optical lattices [3, 4]. In these systems quantum control concerns the internal state of the atoms [5], the atomic position [6, 7, 8] including their quantum mechanical center-of-mass motion [9, 10], the atom-atom interaction [11, 12, 13, 14, 15, 16] (or the interaction between atoms and external fields), and, the possibility to selectively manipulate each individual particle within a large ensemble [17, 18, 19].

The experimental setup built up during my work pursues the line of a bottom-up approach. It comprises a deep one dimensional optical lattice which serves as a storage place for on the order of 10 neutral Cesium atoms each confined to one lattice site. Their positions along the lattice axis can be determined with single site resolution using fluorescence imaging [20]. Moreover, atomic patterns can be prepared by selectively removing atoms from an initially highly but irregularly filled lattice [21]. Similar to the work presented in [17] we coherently manipulate the spin of each atom using resonant microwave radiation. In the sense of quantum computing, this corresponds to imprinting the information of one qubit with the basis $|0\rangle$ and $|1\rangle$ onto two dedicated spin states. The entire atom string thus corresponds to a quantum register where the information is stored in the internal states.

The goal of our setup is the investigation of coherent atom-atom interactions mediated via cold collisions on a few particle scale. Such collisions provide the physical means for entangling the internal state of several atoms [11, 12, 13, 14], which is the basis for quantum information processing. An intrinsic requirement for their realization is the ability to controllably place two atoms into the same lattice site and to separate them again after the contact. Therefore, we employ the technique of a spin dependent transport presented in [7], where the optical lattice possesses the capability to transport an atom to the 'left' or to the 'right' depending on its spin state. Performing the transport with an atom prepared in a spin superposition results in an atom interferometer or in a quantum walk (the

quantum analog of the random walk [22]), when the spin rotation and the transport are successively iterated several times [8, 23].

For the achievement of reproducible atom-atom interaction however, one further degree of freedom must be brought under control, and this is the quantized center-of-mass motion within a lattice site. An approved method for cooling close to the ground state also working with a small number of atoms is the so-called sideband cooling technique. It originates from the field of trapped ions where it was developed to perfection [24] and it was early on successfully transferred to the neutral atom field [9, 25, 26]. It is a variant of laser cooling exploiting a narrow linewidth laser transition which allows to resolve the energetic spacing between the quantized vibrational states of the trapping potential. The technique moreover provides an experimental tool for the coherent control of the vibrational state and plays a key role in the realization of entanglement between several trapped ions [27, 28].

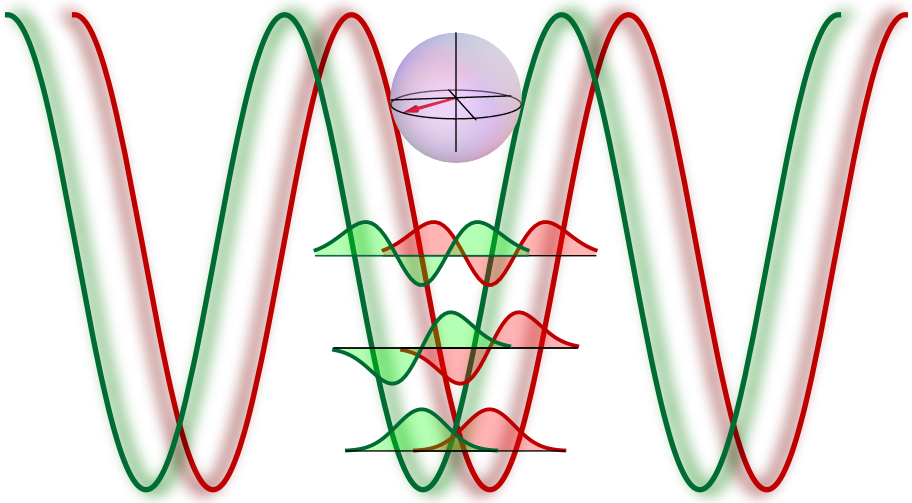

Within my work I have implemented a conceptually equivalent sideband cooling scheme based on microwave radiation, which in contrast to lasers possesses a negligible photon recoil [29]. Instead, it employs the spin dependent lattice which provides the required mechanical impact onto the atomic center-of-mass motion. Using this cooling scheme I prepared and verified a 1D ground state population of 97% along the lattice axis, which is limited by residual heating mechanisms and which is fully competitive to previously reported results. An advantage of our scheme is the reduced number of required lasers which simplifies the experimental setup and which is attractive for setups with a limited optical access [30, 31].

Starting from such a well defined initial state, I have demonstrated the coherent control of the vibrational degree of freedom. The spin dependent lattice thereby provides a simple mean to tune this operations, as they are directly related to the overlap between different atomic wave functions (also called Franck-Condon

factor). In particular, I present results of motional state manipulation beyond the so-called Lamb-Dicke regime [32, 33, 34], where the displacement between two coupled wave functions is equal to, or even exceeds the size of the motional ground state. My investigations include a detailed analysis of present decoherence sources. The presented tools allow to store qubits in a purely motional state [35] which potentially is less susceptible to technical noise sources [36].

The detection of the motional state is accomplished by methods adopted from the ion community [37, 24] which rely on coherent mapping of the motional state onto the internal state of the atom. I finally present the results of a modified detection procedure where atoms are removed from the lattice depending on their vibrational quantum number. This method is less stringent to decoherence processes and promises a more robust operation. As it is a projective measurement of the motional energy eigenstate it moreover allows to investigate quantum thermodynamical properties [38, 39] in a well controlled environment.

Our new approach of motional control is appealing because of its experimental robustness, and represents an alternative technique which offers a large degree of flexibility and which can be employed in many existing setups.

Chapter 1

Experimental setup

1.1 Overview of the experimental apparatus

At the beginning the experimental setup is outlined at which the data presented in this work are obtained. It is built for the controlled quantum mechanical manipulation of single or a hand full of neutral ^{133}Cesium atoms. The control methods have been developed in the last few decades and are shortly summarized in this chapter. A schematic view of the setup is shown in figure 1.1.

Vacuum chamber and optical table As usual in this kind of experiments, the gas of the atomic species under investigation is isolated from the environment using a vacuum chamber at room temperature. The ultra high vacuum of 3 10^{-11} mBar is maintained by an ion-getter-pump. During the construction we payed attention to place the ion-getter-pump with its strong permanent magnets as far as possible from the trap position. To not reduce the pumping cross-section, we use large tube diameters. The low pressure is a prerequisite for a negligible loss caused by collisions between trapped atoms and atoms from the background gas.

In order to ensure a good optical access for the lasers and for the detection lens system, the experimental region is situated in a glass-cell. The outer facets of the glass-cell are anti-reflection coated in order to suppress laser power losses and spurious laser reflections. Unfortunately, it was not possible to coat the inner facets. Other, metallic, components of the vacuum chamber are fabricated out of very low-magnetic stainless steel of the SAE-grade '316LN'. The glass to metal junction of the glass-cell is as well manufactured out of low-magnetic steel. This is done for the purpose of a well defined magnetic field in the vicinity of the atomic sample, as a spurious field affects the Zeeman levels of the atoms. For the same reason, the optical table forming the platform for the main setup is built from '316LN'-

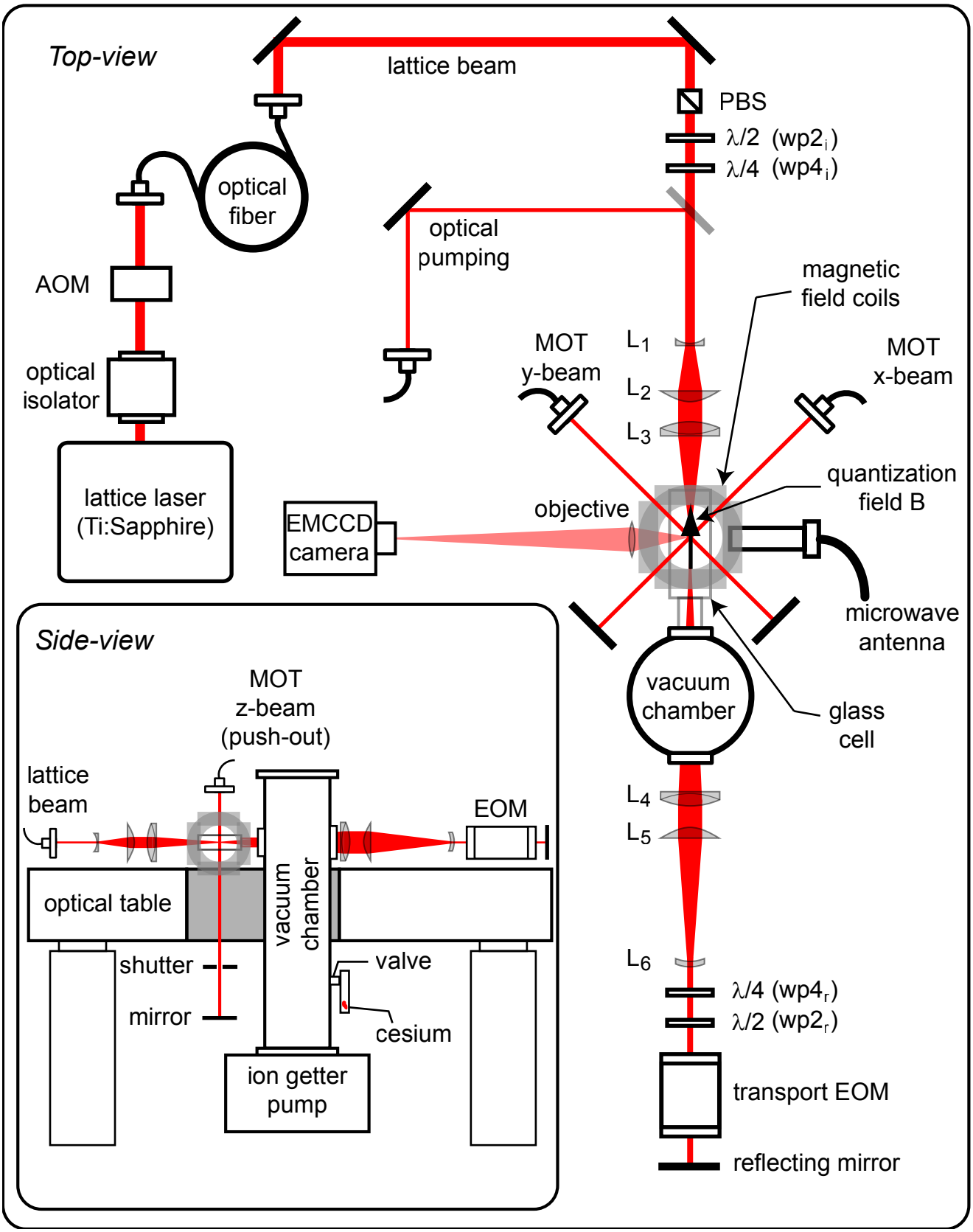

Fig. 1.1: Schematic experimental setup (not to scale). Abbreviations: MOT=Magneto optical trap, EMCCD=Electron multiplying CCD camera, EOM=Electro-optic modulator, AOM=Accuousto-optic modulator, PBS=polarizing beam splitter cube, wpX_{x}=quarter or half wave plate

steel. The whole table is supported by self leveling legs which provide vibrational isolation in order to ensure interferometric stability of the laser setup. This turned out to be important for the nanometer precision of the atomic position detection and manipulation [21]. All components including vacuum chamber and magnetic field coils are rigidly mounted with respect to the table in order to achieve a common frame of reference.

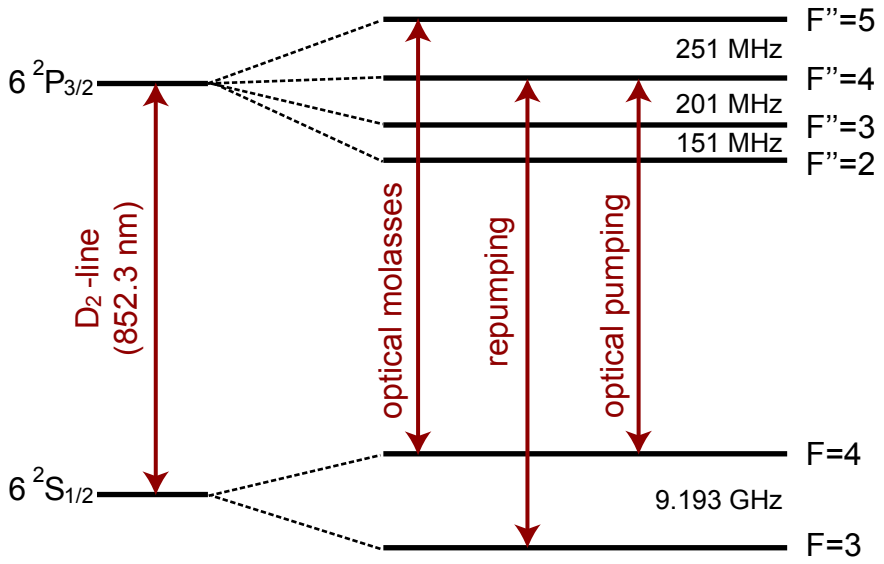

Fig. 1.2: Term scheme for the cesium D2-transition.

Magneto optical trap The magneto-optical trap (MOT) is nowadays the working horse in experiments with cold neutral atom clouds [40]. Since its first experimental realization [41] it is reliably used in many experiments for capturing atoms at room temperature and providing a Doppler-cooled atomic sample in the sub-millikelvin regime. We have built up a retro-reflecting three-arm configuration where two horizontal axes intersect with one vertical axis in the zero-field-point of the magnetic quadrupole field. The MOT-coils in anti-Helmholtz configuration above and below the glass cell generate a magnetic field gradient of up to 37 G/cm along the symmetry axis of the coils[1].

Both, the molasses laser and the repumping laser (see the term scheme in figure 1.2) required for the MOT are generated by external cavity diode lasers[2] [42, 43]. They are frequency stabilized using Doppler-free polarization spectroscopy [44], resulting in a linewidth of ∼1 MHz which is smaller than the natural line width

[1] Current supply: Delta Elektronika SM70-45 D
[2] Self made laser heads controlled by a Toptica DC110 unit

(Γ_{Cs}=5 MHz FWHM) of Cesium [45]. The diode laser setup is situated on a separate optical table and the lasers are guided using polarization maintaining fibres right to the vicinity of the glass-cell. The short paths ensure a stable MOT alignment over months. The frequency of the molasses laser can be tuned around the $F = 4 \rightarrow F'' = 5$ resonance using an acousto-optic modulator. It is additionally used for a fast power regulation.

The beam waist radii at the position of the atoms amount to ∼1.4 mm, but the retro-reflected beams are slightly smaller in order to compensate for the losses after passing the glass-cell surfaces. The power of each molasses laser amounts to 180 μW which corresponds to a peak laser intensity of approximately five times the saturation intensity (1.1 mW/cm^2). The molasses detuning is set to 10 MHz≈$2\Gamma_{Cs}$ with respect to the $F = 4 \rightarrow F''$=5 transition and is experimentally optimized for a fast MOT loading. The repumper required for returning atoms back to the cooling cycle is resonant with the free atom $F = 3 \rightarrow F'' = 4$ transition, its power is 15 μW and it co-propagates with the vertical molasses beam.

Optical setup for the lattice potential After the atoms have been captured by the MOT within a few hundreds of milliseconds (this depends on the present partial cesium pressure and on the number of required atoms) the atoms are transferred into the dipole trap [46]. This trap is generated by a far off-resonant Titanium:Sapphire laser beam [3] with a wavelength of λ_{lat}=865.900 nm. The incoming and the reflected beam form a linearly polarized standing wave. An optical isolator[4] prevents the reflected beam from entering into the laser resonator. Due to the polarizability of Cesium, the atoms are attracted towards the antinodes of the standing wave (see section 1.2). It thus forms a one-dimensional conservative lattice potential

$$U(z) \propto I_0 \cos^2(k_{lat} z). \tag{1.1.1}$$

Here, $U(z)$ labels the trapping potential, I_0 is the peak intensity at the position of the antinodes and k_{lat} labels the wave vector of the trapping laser.

Laterally to the beam axis the atoms are confined by the Gaussian profile of the trapping laser. For tight confinement the laser is focused down to a e^{-2} waist radius of 20 μm. This is accomplished by a lens system which apart from the custom-made meniscus lens, is built up from standard spherical lenses[5]. Their details are listed in table 1.1 and have been tested and optimized in advance with a lens simulation software[6]. The lens system has to fulfill the boundary conditions defined by the size

[3] Coherent MBR 110 pumped by a Coherent V18
[4] Linos FI 660/110-8 SI
[5] Thorlabs Inc. and Lens-Optics GmbH
[6] OSLO optical design software, Lambda Research Corporation

Tab. 1.1: Specification of the lens system for the lattice beam

lens type/focal length (mm)	srfc. nb.	radius of curvtr. (mm)	distnc. to next srfc. (mm)	material
L_1: plano-concave	1	-51.0	4.0	BK7
-100	2	∞	68.47	air
L_2: plano-convex	3	∞	6.7	BK7
175	4	-90.1	arbitrary	air
L_3: doublet	5	121.22	6.6	BAFN10
250	6	-146.14	2.6	SFL6
	7	1235.9	243.19 +496.97	air/vacuum
L_4: doublet	8	1132.4	2.6	SFL6
500	9	259.41	4.5	LAKN22
	10	-346.7	arbitrary	air
L_5: plano-convex	11	154.5	5.1	BK7
300	12	∞	270.11	air
L_6: meniscus	13	-8.956	3.0	BK7
-30	14	-22.96	500	air

of the vacuum chamber and, for the retro-reflecting part, by the free aperture of the electro-optic modulator. A proper lens alignment turned out to be important for the achievement of long coherence times of the trapped atomic sample (see page 18). The verification of the alignment was checked using atoms as a probe for the generated potential by measuring their radial and axial oscillation frequencies (see page 33 and [47]). Within experimental uncertainty the measurement reproduced the simulated beam waist and on-axis intensity.

The power of the lattice beam laser is actively stabilized by a servo loop acting on an acousto-optic modulator (AOM). The servo has a bandwidth of ∼30 kHz and provides an analog input port for the definition of the set-point which controls the lattice depth. During the atom transfer and for atom detection the lattice depth is set to 400 μK which requires a single-pass laser power of 100 mW. The pointing of the lattice beam is passively stabilized by shortening the free beam path using a fiber line. Additionally, air turbulences have been suppressed by covering the experimental table with curtains and by closing the brake-through in the table around the vacuum chamber. From the measurement of the radial position fluctuation of the trapped atoms the pointing fluctuation in the focal plane is expected to be smaller than $\pm 1\mu$m [23].

The main feature of the lattice is its capability to transport atoms state dependent to the 'left' or to the 'right' along the lattice axis. This is accomplished by controlling the polarization of the trapping laser. While the polarization of the incoming beam is fixed by a polarizing beam splitter cube (PBS) the linear polarization of the reflected beam can be rotated by a combination of an electro-optic modulator[7] (EOM) and a quarter wave plate $wp4_r$ in the retro-reflected path of the lattice beam (see below). All other wave-plates[8] are installed for convenience which will be explained in more detail in section 1.2.

Observation optics and computer control After the atoms have been transferred from the MOT into the optical lattice, they are continuously illuminated by the optical molasses. This firstly provides continuous cooling in order to counteract present heating mechanisms, and secondly, the presence of atoms can be verified by imaging their fluorescence onto an electron-multiplying-CCD camera (EMCCD[9]). The magnification of the objective lens system amounts to 55.6 [20, 23, 48]. An exemplary image of atoms trapped in the optical lattice is shown in figure 1.3. Such images form one of the pillars of our experiment as they provide the information about the number of trapped atoms and their positions along the trap axis down to a single site resolution. Successive images of the same atomic sample additionally provide information about the fluctuation of the lateral trap position and thus about the pointing stability of the lattice beams.

In order to obtain images of good quality, first of all the molasses parameters and the lattice depth are experimentally optimized for highest fluorescence rate, but at the same time the atoms are not allowed to hop between the lattice sites. The power typically used for the molasses lasers amounts to 60 μW per beam and leads to $\sim$1.8 times the saturation intensity at the position of the atoms. The optimal molasses detuning is found to be 25 MHz red-detuned with respect to the $F = 4 \rightarrow F''=5$ transition. For the experimental data in this work the position information is discarded because in first place only the atom number before and after manipulations is important (see below). Furthermore, for the atom counting a compromise between short experimental time and detection accuracy is made by choosing an illumination time of 200 ms and by loading $\sim$20 atoms per shot. With these settings the accuracy of the number determination is $\pm$1 atom for each image.

The camera is read out by a computer software [23] which deduces the number of detected atoms. The same computer is also responsible for the timing of the experimental sequence for almost all devices. The PCIe-card[10] provides analog and

[7] Conoptics 350-80BK driven by the high voltage amplifier Conoptics 302RM
[8] Custom-made zero order wave plates (specified for 867$\pm$0.3 nm; not true zero order)
[9] Andor iXon DV887DCS-FI
[10] National Instruments PCIe-6259

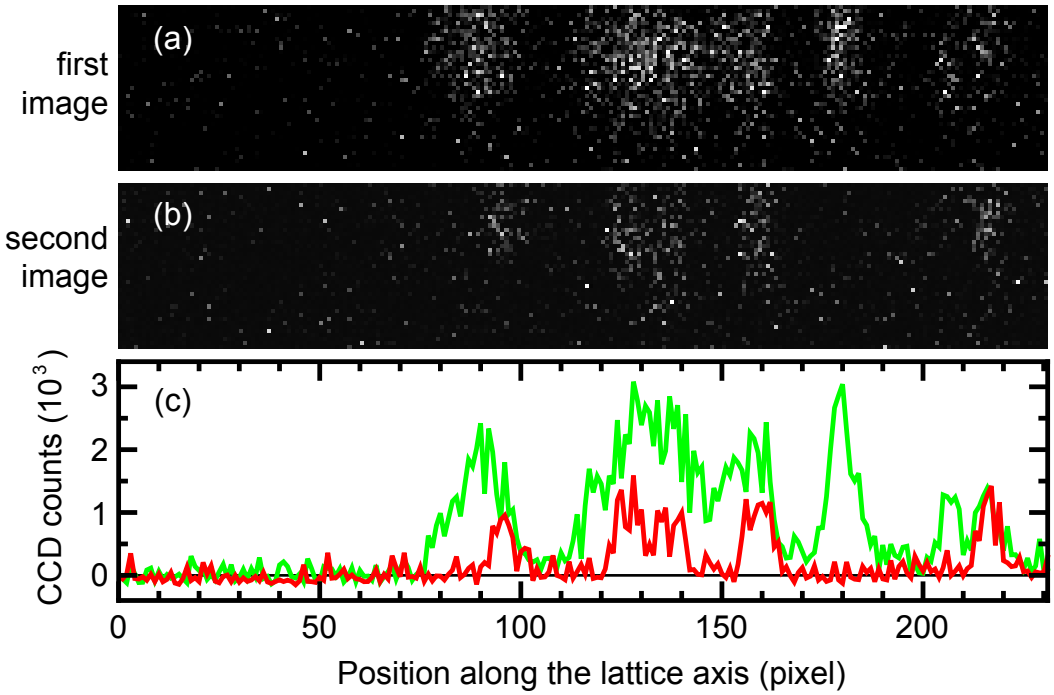

Fig. 1.3: Image of atoms (a) before the microwave pulse and (b) after the state-selective detection (200 ms exposure time). Panel (c) shows the corresponding histograms after the images have been vertically binned. The analysis of the histograms reveals that each atom equally contributes to the total count number and that 5 out of ∼15 atoms have survived the manipulation.

digital outputs with a maximum time resolution of 2 μs/sample. In some cases the noise performance of the analog outputs is important. Fortunately, most of the spurious signals lay far above 300 kHz and in addition most of them are correlated with the cycles of the sample clock. For simplicity we specify a noise level of ± 5 mV. In some cases more serious is the crosstalk between different output channels which in addition are affected by the EMCCD control card. This disturbances have been suppressed by optimizing the grounding connections of all devices and by using a buffer amplifier, but they could not be completely eliminated. Eventually, the mean voltage of a given analog output channel can vary up to ∼10 mV , depending on the load of the other channels. The shift of the output voltages is usually not checked but it is static within the experimental sequences and thus leads to small systematic deviations.

Preparation and detection of the atomic spin state The relevant hyperfine structure of the Cesium is sketched in figure 1.4. A homogeneous magnetic field

of 3 G along the trap axis defines the quantization axis[11] and lifts the degeneracy between the Zeeman levels. Three pairs of mutually orthogonal coil pairs compensate residual magnetic fields at the position of the atoms. For the initialization of a pure spin state the atoms are optically pumped to $|F = 4, m_F = 4\rangle$. The two lasers required for optical pumping are guided by a single fiber and are overlapped with the axis of the lattice beam using an uncoated glass plate. A small residual angle between the beam axes allows to block the optical pumping beam after it passes the vacuum chamber so that it gets not reflected by the optics of the lattice beam. The reflection of the circularly polarized optical pumping beam would otherwise be strongly affected by the polarization optics of the lattice beam and would prevent the preparation of a pure spin state. Eventually, with a power of 30 nW for the $F = 4 \rightarrow F'' = 4$ laser and of 7 nW for the $F = 3 \rightarrow F'' = 4$ laser, the dark state is populated with ≈98% of atoms within 10 ms. We attribute the remaining initialization impurity to the angle between the quantization axis and the axis of the optical pumping beams.

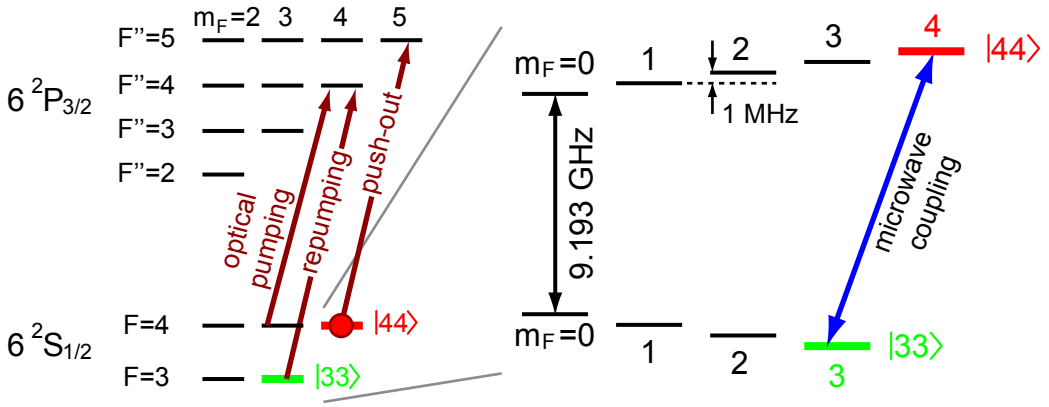

Fig. 1.4: The Zeeman-levels of the $6^2S_{1/2}$ hyperfine ground states of cesium with applied quantization field. The state $|F = 4, m_F = 4\rangle \equiv |44\rangle$ is initially prepared by optical pumping. Then microwave radiation coherently couples this state to the $|F = 3, m_F = 3\rangle \equiv |33\rangle$.

The detection of the atomic spin is accomplished by removing all atoms in the $F = 4$ hyperfine state using the vertical molasses beam which performs the 'push-out' (see figure 1.4, repumper is switched off) [6]. The duration of the state-selective push-out pulse is set to 150 μs, its power amounts to 15 μW and it is set on resonance with the $F = 4 \rightarrow F'' = 5$ transition. In the lattice with a depth of 80 μK (see below) almost 100% of the atoms in the $F = 4$ hyperfine state are removed within a timescale significantly shorter than the radial oscillation period of the trapped

[11] Current supply Toellner TOE-8733

atoms. At the same time almost all atoms in the $F = 3$ state remain trapped. Using the push-out technique a basic characteristic parameter can immediately be determined: By varying the waiting period between initialization and state-selective detection we determine a spin relaxation time of T_1 ∼100 ms. This value is limited by off-resonant photon scattering of the trapping laser.

As indicated in figure 1.4, the outermost Zeeman-states $|F = 4, m_F = 4\rangle \equiv |44\rangle$ and $|F = 3, m_F = 3\rangle \equiv |33\rangle$ form the two-level qubit subsystem where all our spin manipulations are performed. The spin rotation is accomplished by a magnetic dipole transition in the microwave regime with a frequency around 9.2 GHz. The microwave radiation is generated using a self assembled setup (see also [49] for more details) basically consisting of a local oscillator[12] at 9.04 GHz which is mixed[13] with the output of a vector generator[14] delivering ∼160 MHz. Both are referenced to the 10 MHz signal of an atomic clock[15]. The power of the resulting signal can be controlled using a PIN-diode attenuator[16] and is subsequently amplified[17] to a maximum power of 41 dBm. Thereafter, the signal passes an isolator[18] and a bidirectional coupler[19]. Using a low-loss cable[20], it is guided to a cut waveguide[21] which finally irradiates the atoms. Eventually, the turnkey setup permits arbitrary scans of frequency and phase and allows for arbitrary pulse shapes, in particular a Gaussian pulse envelope.

1.1.1 Experimental sequence

All sequences begin with capturing Cesium atoms from the background gas within 100-500 ms whereafter on average 1-30 atoms are transferred into the optical lattice. The MOT and the optical lattice are operated simultaneously for 50 ms. During this period atoms loaded into the same potential well undergo light-induced collisions [50] so that multiply occupied wells do not occur in the final atom string. Next, the magnetic field gradient necessary for the MOT is switched off within 50 ms.

A first image with an illumination time of 200 ms provides their exact initial number. Subsequently, the molasses parameters are changed to optimize cooling within the lattice. Typically, the power of the molasses beams is continuously reduced to

[12] MITEQ, PLDRO-10-09040-3-15P
[13] MITEQ, SSM0812LC2CDC
[14] Agilent, E4432B
[15] Stanford Research System, PRS10
[16] MITEQ, MPAT-08001200-60-10
[17] MITEQ, AMF-6B-08500950-40-41P-TTl
[18] DITOM, DF6859
[19] MITEQ, CD-702-1242-30s
[20] Spectrum Elektrotechnik GmbH, 300-1300-11-11)
[21] FLANN, 15040

30 μW within 20 ms while their red-detuning is increased to 30 MHz. In the lattice with a depth of 400 μK the achieved temperature of the atomic ensemble amounts to $\sim$ 20 μK. The temperature is determined by measuring atom loss after adiabatic lowering of the lattice depth [51]. For coherent manipulation of the atoms, the lattice depth is ramped to 80 μK (20 mW laser power) within 20 ms. The lowering of the trap depth adiabatically cools the atomic sample so that the final temperature amounts to $\sim$ 10 μK. The depth of 80 μK is chosen by reducing the lattice depth as far as possible, but leaving a conservative safety margin in order to prevent atom losses. A shallow lattice leads to a lower off-resonant photon scattering rate, and moreover, technical decoherence sources are suppressed (see section 2.4).

Thereafter, the atoms are manipulated by means of magnetic fields, microwave radiation and laser light. For spin rotations, e.g., the quantization magnetic field is switched on within 100 ms. An optical pumping stage with a duration of 20 ms initializes all atoms in the $|44\rangle$ state. When microwave cooling is applied (see section 3.1) most of the atoms additionally are cooled to the axial ground state. Subsequently, microwave pulses with a defined frequency, duration and pulse shape induce Rabi oscillations between the states $|44\rangle$ and $|33\rangle$. Atoms remaining in the $|44\rangle$ state are removed from the lattice and its depth is ramped up again to the initial value of 400 μK. Finally, a second image detects the number of remaining atoms.

In order to decrease statistical fluctuations, the entire sequence is repeated typically five times with identical parameters. The five repetitions yield five values for the ratio between the initial and final atom number. Their mean value defines the measured survival probability and their standard deviation determines the confidence interval for the survival probability. This way, the error bar takes into account the binomial distribution due to the statistical fluctuation of the atomic number, errors of atom counting and fluctuating experimental parameters. By scanning one experimental parameter, e.g. the microwave frequency, the survival probability for each sample point is measured and finally yields e.g. a complete microwave spectrum.

1.1.2 Microwave operations

In this work, all spin operations are restricted to the two level subspace spanned by the hyperfine ground states $|44\rangle$ and $|33\rangle$. The Schrödinger equation for this system including the microwave coupling reads [52, 53, 54]

$$\begin{pmatrix} E_{44} & \hbar\,\Omega_\mathrm{R}/2 \\ \hbar\,\Omega_\mathrm{R}^*/2 & E_{33}+\hbar\,\omega_\mathrm{mw} \end{pmatrix} \begin{pmatrix} \psi_{44} \\ \psi_{33} \end{pmatrix} = i\hbar\frac{d}{dt}\begin{pmatrix} \psi_{44} \\ \psi_{33} \end{pmatrix}. \tag{1.1.2}$$

Here, E_{44} and E_{33} denote the eigenenergies of the hyperfine states and ψ_{44} and ψ_{33} label the corresponding quantum mechanical coefficients. The microwave field is characterized by its frequency ω_{mw} which can be tuned in resonance with the atomic transition $\omega_0 = E_{44} - E_{33}$, and by its Rabi frequency Ω_{R} (the asterisk denotes the complex conjugate). The Rabi frequency and the magnetic field amplitude $\vec{B}_{\mathrm{mw}}$ of the microwave radiation are related via the transition matrix element

$$\Omega_{\mathrm{R}} = \frac{1}{\hbar}\langle 44|\hat{\mu}\vec{B}_{\mathrm{mw}}|33\rangle, \tag{1.1.3}$$

where $\hat{\mu}$ labels the magnetic dipole moment operator. In case of a constant Rabi frequency (rectangular pulse shape) the solution of the Schrödinger equation is the well known Rabi oscillation between the two states (for a two level system Ω_{R} can be chosen to be real)

$$P_{33}(t) = \frac{\Omega_{\mathrm{R}}^2}{\Omega_{\mathrm{R}}^2 + \delta^2} \sin\left(\sqrt{\Omega_{\mathrm{R}}^2 + \delta^2}\, t\right). \tag{1.1.4}$$

Here, $P_{33}(t) = |\psi_{33}(t)|^2$ is the probability to find the atom in the state $|33\rangle$ and $\delta = \omega_{\mathrm{mw}} - \omega_0$ is the detuning of the microwave field. In particular, this solution can be found by calculating the eigenstates of the time independent Hamiltonian in equation 1.1.2. This is the so-called dressed state picture of the combined atom plus field system [54]. The time evolution of the eigenstates thereby becomes trivial and formula 1.1.4 is immediately obtained by the transformation back to the original basis. For more complicated pulse shapes the Schrödinger equation can be solved numerically. An example of the measured microwave spectrum and Rabi oscillation is shown in figure 1.5.

The model of the coherent evolution can be extended by phenomenological decay constants in order to take into account decoherence effects [52]. The longitudinal time constant $T1 \approx$100 ms, modeling the lifetime of the pure spin state, was already mentioned above. The dephasing constant $T2 = (196 \pm 3)$ μs is measured by a Ramsey experiment [23]. The homogeneous contribution to the dephasing constant is measured by a multiple spin-echo technique, which eliminates all inhomogeneous dephasing sources, is found to be $T2^* = (879 \pm 5)$ μs. In our experiment, homogeneous dephasing is caused by fluctuations of the lattice potential and of the magnetic field. Inhomogeneous dephasing mostly originates from the thermal motion of the atoms. In my thesis I will not consider this global decoherence constants. Instead, as discussed in the next chapter, the Schrödinger equation 1.1.2 will be extended in order to take into account the quantized axial motional. In this system, decoherence

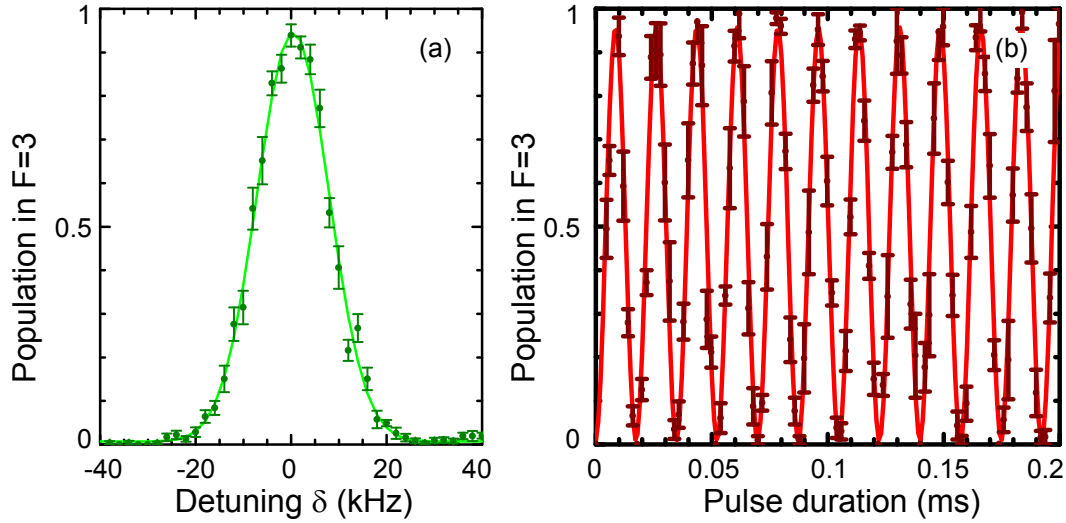

Fig. 1.5: A spectrum (a) of a Gaussian microwave pulse showing the resonance peak for the $|44\rangle \leftrightarrow |33\rangle$ transition. The $1/\sqrt{e}$ width of the pulse amounts to 15 μs. The resulting $1/\sqrt{e}$ frequency width of (15.0±0.1) kHz is only slightly broader than the Fourier limit of 14.1 kHz. (b) Rabi oscillation at full microwave power with $\Omega_{\mathrm{R}} = 2\pi\, 59$ kHz.

will be investigated for each individual microwave transition affecting both the spin and the vibrational state.

1.2 The spin-dependent optical lattice

1.2.1 The magic wavelength

When the theory of the AC-Stark shift is applied to a simple two level atom which is driven by an off-resonant laser field, one finds that atoms in the ground state are attracted towards the intensity maxima of the laser for the red-detuned case (negative potential (well)), and are repelled from them in the blue-detuned case (positive potential (hill)) [46]. For multilevel atoms, due to their vector polarizability [55, 56, 57], the lattice potential becomes spin dependent (proportional to the m_{F} quantum number), once circularly polarized components are present. For alkali atoms this effect is particularly pronounced for a lattice laser with a wavelength in-between the two D-transitions. In the perturbative calculation of the lattice potential the AC-stark shift (also called light shift) of an unperturbed state is computed

by taking into account the coupling to all other unperturbed states whereby selection rules are considered. As the contributions are scaled with the detuning of the lattice frequency with respect to the considered transition, only the most 'resonant' transitions are relevant. In our case, only the first excited states $6^2P_{1/2}$ and $6^2P_{3/2}$ are taken into account for the calculation of the light shift of the $6^2S_{1/2}$-ground state. In detail, perturbation theory is used up to second order whereby only the dipole transitions are taken into account for which the rotating wave approximation is used. Additionally, the calculation exploits experimental data on transition strengths (more details can be found in [58]). In figure 1.6 the situation for a purely circularly polarized lattice beam is presented. Qualitatively, in case the hyperfine structure is disregarded, a 'magic' wavelength can be found. For this wavelength the two ground states $|-1/2\rangle$ and $|1/2\rangle$ experience a light shift potential exclusively generated by one of the circularly polarized components. This is due to the fact that for the 'wrong' polarization the blue detuned and the red detuned light shifts cancel each other.

For an intuitive picture of our lattice potential, the linearly polarized counter-propagating laser fields can be decomposed into their circular components. This decomposition is more convenient, as the quantization axis is oriented along the lattice beam propagation and the two components induce $\sigma^{+/-}$-transitions, respectively. For each Zeeman state and for each circular component the light shift can thus be computed independently and the total potential is obtained by a simple sum over both polarization components.

The same approach can be used when the hyperfine structure is taken into account. The calculation of the two potential contributions for our qubit states is shown on the right side of figure 1.6. Unfortunately, for this states there is no unique wavelength any more satisfying the 'exclusive potential' condition. All data presented in this thesis are measured using the 'magic' wavelength for the $|44\rangle$ state (865.900 nm) so that it is exclusively trapped by the σ^+ polarized component. For this wavelength the potential for each qubit state can be written as

$$\begin{aligned} U_{44} &= c_{44_+} I_{\sigma^+} + c_{44_-} I_{\sigma^-} \approx c_{44}(\frac{8}{8} I_{\sigma^+} + \frac{0}{8} I_{\sigma^-}) \\ U_{33} &= c_{33_-} I_{\sigma^-} + c_{33_+} I_{\sigma^+} \approx c_{33}(\frac{7}{8} I_{\sigma^-} + \frac{1}{8} I_{\sigma^+}). \end{aligned} \tag{1.2.1}$$

The coefficients $c_{xx,\rho}$ denote the scaling factors between the light intensity and the trapping potential for each Zeeman state xx and each polarization ρ. The approximation holds when the hyperfine splitting of 9.2 GHz between the ground states $|F=4\rangle$ and $|F=3\rangle$ is neglected with respect to optical transitions. The ratios between the scaling factors are then determined by the Clebsch-Gordon coefficients.

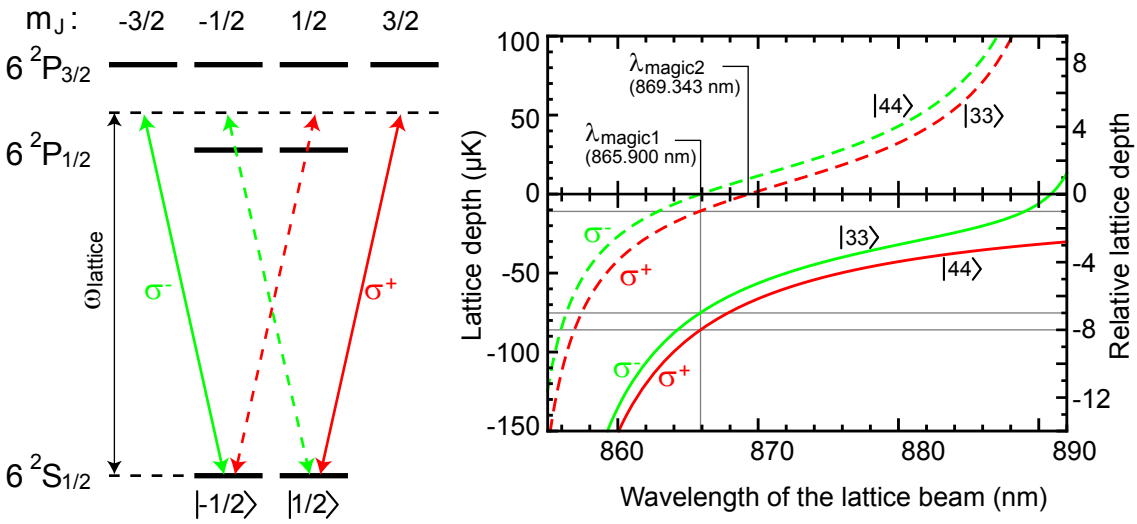

Fig. 1.6: (left) When the lattice laser is red-detuned with respect to the D2 transition but at the same time blue-detuned with respect to the D1 transition their light shift contributions can cancel each other. (right) Wavelength dependent calculation of the spin dependent potential contributions (taking into account the hyperfine structure) for the two circularly polarized components (for a lattice beam power of 20 mW). In contrast to the fine structure approximation on the right side, no wavelength exists for which the states $|44\rangle$ and $|33\rangle$ possess exactly complementary coupling strengths.

In the experiment, each of the circular components forms a standing wave. As long as the linear polarizations of the incoming and the retro-reflected lattice beams are parallel to each other both standing waves identically overlap. Thus, the dipole trap potential is (almost) identical for any ground state $|F, m_F\rangle$ because the sum of the left handed and the right handed contribution is always the same. This is important, as during the illumination of the atoms by the near resonant optical molasses the hyperfine state is changed continuously. Despite this fact each atom remains trapped in its initial potential well. Once the polarizations of the counter-propagating beams encloses a finite angle ϑ, the spin dependent nature of the lattice potential, immediately becomes evident.

1.2.2 Controlled shift of the potentials

By means of the setup sketched in figure 1.7 the two circularly polarized standing waves can be shifted with respect to each other [7]. In the linearly polarized basis this corresponds to a relative rotation of the polarization planes of the counter

propagating laser beams. The linear basis is more convenient for the experimental purpose as the polarization is analyzed by 'linear' beam splitters (unfortunately, there's no beam splitter which works directly in the circular basis).

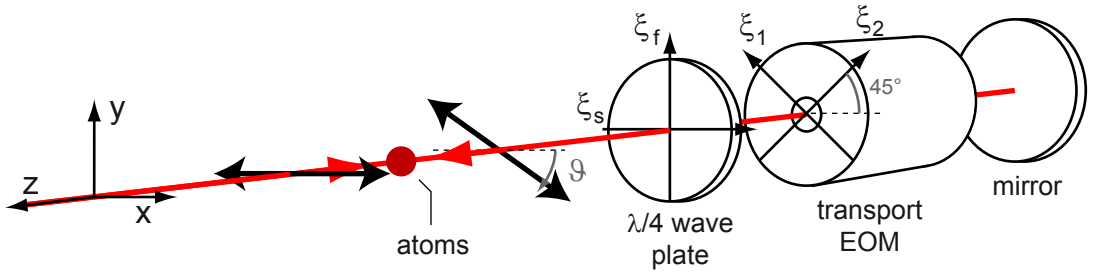

Fig. 1.7: The setup which performs the lattice shift by rotating the angle of the linear polarization of the reflected beam. The principle axes of the electro-optic modulator (EOM) are labeled by ξ_1 and ξ_2, those of the quarter wave plate by ξ_f and ξ_s (fast and slow axis). The polarization angle ϑ between the counter-propagating beams is related to the voltage controlled retardation phase of the EOM by $\vartheta = \phi_\mathrm{EOM}$.

When talking about the lattice potential the more intuitive picture is drawn using the circular basis. In this picture the incoming laser beam is a superposition of two circularly polarized light fields with equal field amplitudes. Moreover, the relative phase between both fields is zero. After passing the quarter wave plate $\mathrm{wp4_r}$ each of the components is transformed into linearly polarized fields. They are mutually orthogonal and exhibit a rotational angle of 45° with respect to the (fast and slow) axes of the quarter wave plate. The axes of the subsequent electro-optic modulator (EOM) are aligned to be collinear with one of the linear field components, respectively. According to the applied voltage the EOM retards one of the components with respect to the other, so that the two transmitted fields exhibit a defined phase difference ϕ_EOM. After retro-reflection the phase difference is doubled which is one of the advantages of this setup. Subsequently, the quarter wave plate $\mathrm{wp4_r}$ acts again as a converter between the linear and the circular basis. Altogether, the described setup introduces a well controllable phase shift between the circular components of the reflected beam and accordingly the standing wave intensity pattern I_{σ^+/σ^-} of both components is shifted with respect to each other

$$\begin{aligned} I_{\sigma^+/\sigma^-} &= c\,\varepsilon_0 \left\langle (E_0 \cos(k_\mathrm{lat} z - \omega_\mathrm{lat} t) + E_0 \cos(-k_\mathrm{lat} z - \omega_\mathrm{lat} t \pm \phi_\mathrm{EOM}))^2 \right\rangle_t \\ &= 2\,c\,\varepsilon_0\, E_0^2\, \cos^2(k_\mathrm{lat} z \mp \frac{1}{2}\phi_\mathrm{EOM}/2). \end{aligned} \tag{1.2.2}$$

Here, E_0 labels the electric field amplitude of the trapping laser, which is assumed to be the same for both circularly polarized components and for the incoming and the reflected beams; k_{lat} and $\omega_{\mathrm{lat}} = c\,k_{\mathrm{lat}}$ label the wave vector and the frequency of the trapping laser, respectively (c is the speed of light), and $\langle\rangle_t$ denotes the time average over optical frequencies. The phase ϕ_{EOM} labels the single-pass retardation introduced by the EOM whereby the sign is opposite for both components. For the definition of the standing wave shift, let us assume that without applied voltage two marked antinodes lay on top of each other. Their separation is then defined by the relation

$$\Delta x/(\lambda_{\mathrm{lat}}/2) = \phi_{\mathrm{EOM}}/\pi. \tag{1.2.3}$$

When the retardation becomes equal to $\pi/2$, the nodes of one standing wave is exactly at the position of the antinodes of the other standing wave. They overlap again when the retardation amounts to π.

In the picture of the linear polarization we note that, in the ideal case, the reflected circular components have still equal amplitudes. They thus add up to a single purely linearly polarized field. The phase difference between the circular components, however, results in a rotated polarization plane. The relative angle between the incoming and the reflected polarization planes is defined by the relation

$$\vartheta = \phi_{\mathrm{EOM}}. \tag{1.2.4}$$

The advantage of using the presented EOM setup for the control of the lattice shift is first of all, that the optical path for both circularly polarized components is identical. This means that apart from the controlled retardation induced by the EOM their relative phase is not sensitive to e.g. mirror positions. Alternative shift setups can be realized using interferometers which would require a stability close to $\lambda_{\mathrm{lat}}/1000$ in order to be competitive. The Faraday effect could also be exploited for the realization of a dynamic polarization rotation, but, at present, there are no commercial devices which satisfy the requirements of high speed and large rotation angles.

The one-dimensional lattice potential is defined by the equation 1.2.1 whereby the standing wave intensity distribution from equation 1.2.2 has to be inserted. For our wavelength the potential U_{44} is just proportional to the intensity profile I_{σ^+} and thus directly follows its movement along the lattice axis (see figure 1.8). For the potential U_{33}, though, due to the mixing of I_{σ^+} and I_{σ^-} the shift of the intensity pattern is accompanied by a wobbling of its depth. Hereby the total trap depth must be distinguished from the axial trap depth U_{ax} (also called trap contrast). The first value defines the depth with respect to a free atom and thus is identical to the radial confinement. It varies between 1 (in terms of maximum depth) in case of zero

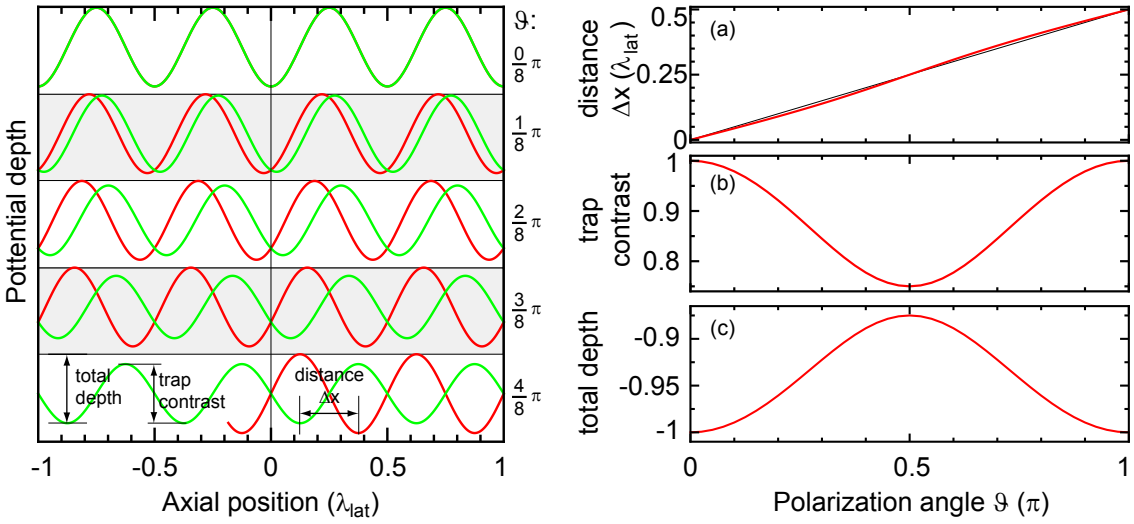

Fig. 1.8: (left) Axial shift of the potentials U_{44} and U_{33} depending on the polarization angle ϑ. (right) (a) The distance between neighboring potential minima of U_{44} and U_{33}. Due to the mixing of the polarization contributions for U_{33} the distance evolves slightly nonlinearly. This also entails a wobbling of the U_{33} potential resulting in a change of its contrast (b) and its total depth (c) during the shift.

shift and 7/8 when the polarization angle is $\vartheta = 90\,°$. The second value characterizes the axial confinement which varies between 1 and 3/4 and thus is different from the radial depth. The mixing of the intensities moreover introduces a nonlinearity for the shift Δx and the polarization angle ϑ. All these effects are measurable in the atomic microwave spectrum as will be presented in section 2.

Alignment of the polarization optics By design, due to the choice of the wavelength and the orientation of the quantization axis, our lattice potential is dependent on the atomic spin. For this reason the potential strongly affects the microwave transitions between the light-shifted atomic states and thus their coherence. For comparison: The trap depth of 80 μK corresponds to 1.6 MHz in terms of frequency, but the microwave resonances are measured with sub-kHz precision. A small elipticity of the trapping laser polarization immediately shifts the position of the microwave spectrum. The common experimental figure of merit for the purity of the linear polarization is the extinction ratio of two polarizers when a 'probe' is placed between them. It is defined by the ratio between the power of the incident and the transmitted laser light, after the analyzing beam splitter is rotated to the minimum transmission. It turns out that at the current status of the experiment a variation of the extinction ratio of the order 10^{-5} shifts the microwave spectrum by

several kHz (compare figure 1.9 to the spectrum in figure 1.5) [59].

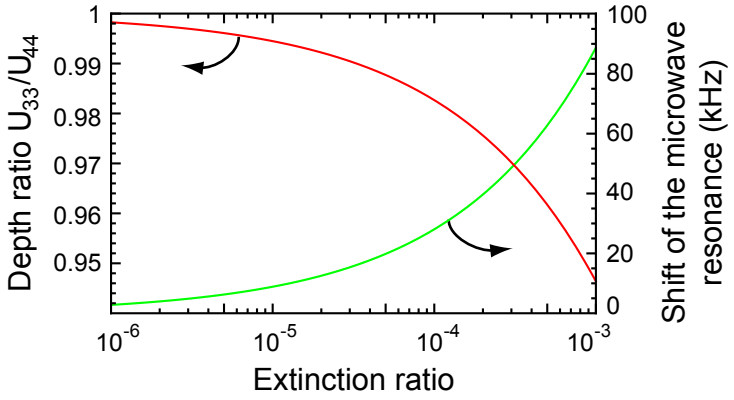

Fig. 1.9: A significant change of the relative depth of the potentials U_{44} and U_{33} can easily be introduced by a slightly elliptically polarized trapping laser. As an example, the trap depth ratio (left axis) depending on the extinction ratio of the reflected beam is presented. A change of the trap depth ratio directly alters the resonance frequency of a microwave transition (right axes). See also section 2.4.

Note that in the setup, apart from the retro-reflected mirror, there are no further mirrors installed in the path of the lattice beam after the polarizing beam splitter cube which defines the polarization of the incoming beam. This is because mirrors in general introduce a phase shift between the horizontal and the vertical (in the reference frame of the mirror) polarization components when the angle of incidence is not exactly zero. Thus a mirror would potentially convert a pure linear polarization into an elliptical one, which moreover varies with the polarization angle of the incident beam.

In order to be able to achieve a precise alignment of the EOM, it thus must be mounted on its own fine adjustable holder. The holder used provides the control over the translational, as well as yaw and pitch degrees of freedom (no roll degree of freedom). The half wave plate $\mathrm{wp2_r}$ is used for a precise rotation of the incident linear polarization components with respect to the principle axes of the EOM. Eventually, the best extinction ratio measured for a beam transmitted through the EOM is on the order of 0.5×10^{-3} which agrees well with the specification of the manufacturer. The limit for the polarization purity is thereby defined by its inhomogeneity after passing the EOM. This can be verified by imaging the beam onto a beam profile camera after it has passed the analyzing beam splitter cube (see figure 1.10).

The effect of the polarization inhomogeneity onto the atoms is in principle significant and, in combination with the finite size of the cloud, contributes to inhomogeneous broadening (see section 2.4). The inhomogeneity in the focal plane of the

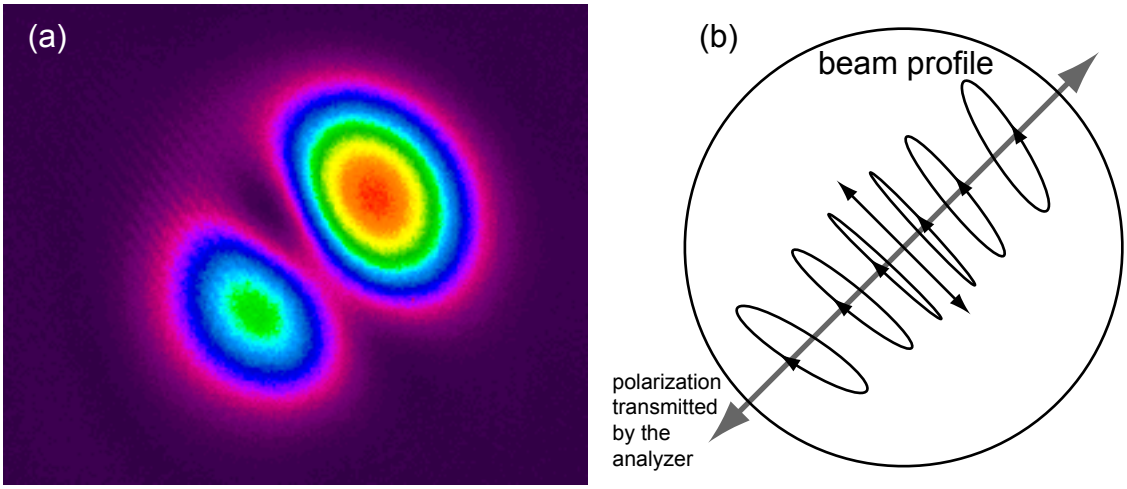

Fig. 1.10: (a) An image of the lattice beam profile after it has passed the EOM and a subsequent analyzing beam splitter cube. When the analyzer is slightly rotated the double spot profile becomes asymmetric. (b) This behavior can be interpreted in terms of polarization inhomogeneity caused by the EOM.

lattice lens system, and thus at the position of the atoms, has though a different profile with respect to the main beam. In order to clarify this, let us assume that the lattice beam can be modeled by a superposition of a purely polarized Gaussian mode and a first order Hermite-Gaussian mode carrying the polarization impurity. At the position of the EOM both modes overlap, which means that according to the scaling of the Hermite-Gaussian profiles, the faulty mode has a smaller waist. In the focal plane of the lens system the waist ratio is inverted so that the faulty mode lies outside the Gaussian profile. This assumption is supported by the experimentally observed improvement/deterioration of the microwave spectrum depending on the exact alignment of the lens system. The quality of the spectrum was finally used as a criterion for the lens positioning (only the last meniscus lens was moved along the beam axis). All data presented in this thesis are obtained with this final alignment and are in very good agreement with a beam waist of 20 μm expected from the lens design. The data could, though, also be explained assuming slightly different focal points of the counter-propagating beams.

During the step by step alignment of the polarization optics an additional polarization distortion caused by the vacuum windows was discovered: Depending on the polarization angle of the incoming beam the extinction measurement of the transmitted beam yields values in the range of 10^{-5} (best case) to 10^{-3} (worst case). We attribute this observation to the stress-induced birefringence within the facet of the glass cell (or, less probably, within the vacuum window on the opposite side).

This distortion shows a similar polarization inhomogeneity as that caused by the EOM. Experimentally, this effect is suppressed by rotating the polarization of the incoming beam parallel to one of the principle axes of the vacuum windows. This is done using the half wave plate $wp2_i$ right after the polarizer. For complete control of the incoming polarization we added the quarter wave plate $wp4_i$.

The last issue for the polarization optics concerns the retardation stability of the EOM. Here, two time scales need to be considered. First, a fast response is desired in order to perform the lattice shift on a time scale of few tens of microseconds. This is mostly a demanding task for the high voltage driver which, in our case, exhibits a -3dB-bandwidth of 370 kHz and at the same time provides an output voltage of 750 V_{p-p}. However, almost all electro-optic materials used for manufacturing EOMs also possess nonzero piezoelectric coefficients which manifest themselves in a resonance like response of the optical signal [49]. For this reason we decided to choose an EOM with specially modified crystals, for which the piezoelectric resonances are suppressed. The dynamic optical response for this EOM nicely follows the electric control signal within the bandwidth of the driver [23].

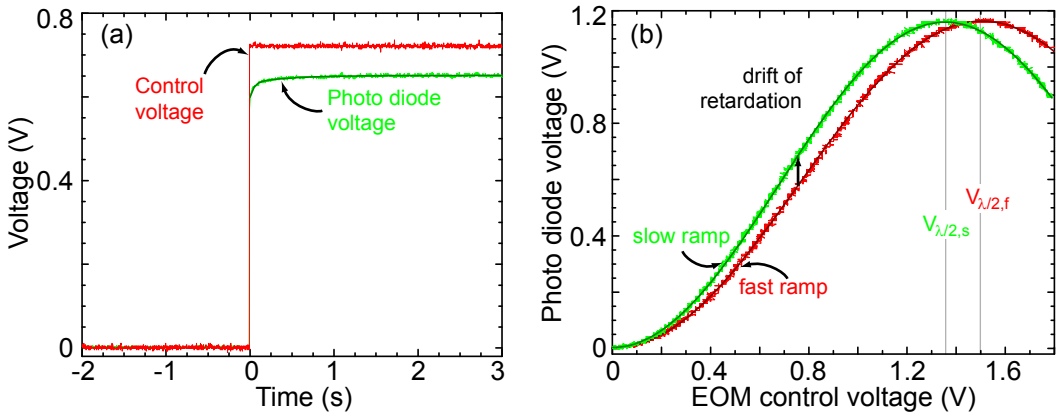

Fig. 1.11: (a) Laser power transmitted by two crossed polarizers with an EOM between them, depending on the linearly ramped EOM control voltage. The response of the EOM depends on the ramp speed: $V_{\lambda/2,f} = 1.489$ V for a 200 μs ramp and $V_{\lambda/2,s} = 1.355$ V for a quasi static 10 s ramp. (b) The time scale for the retardation drift is determined by quickly ramping the control voltage to the vicinity of the quarter wave voltage, and by measuring the $1/e$-time required to reach the stationary state (0.45 s).

The second unexpected and not yet understood phenomenon is a slow drift of the EOM retardation after it has been ramped to a new set-point. It's time scale is on the order of the duration of one experimental sequence. The drift becomes observable in the optical signal of an EOM placed between two crossed polarizers when the drive is quickly ramped to, e.g., the quarter wave voltage and is hold

constant for a few seconds (see figure 1.11(a)). The laser power measured behind the analyzing beam splitter drifts exponentially with a time constant of 0.45 s towards its stationary value. Phenomenologically, our explanation is based on an EOM response which depends on the ramp speed (see figure 1.11(b)). The reason for this could not even be provided by the manufacturer as they usually do not recommend to use a high steady state driving voltage (because of the degradation of the electro-optic crystals). Possibly, the electro-optic coefficients are frequency dependent although the research focus mostly lies in the high frequency domain [60]. We bypass the problem by avoiding long high voltage hold times [23].

Model of the lattice potential The alignment of the polarization optics must be done very carefully in order to eliminate residual circular polarization components which strongly affects both the position of the microwave transitions and their coherence. For the accurate prediction of this influence I perform a simulation of the lattice potential which models the experimental setup as precise as possible. In this way, it is straightforward to investigate the characteristic effects of different experimental misalignments and imperfections. The simulation takes into account the profile of the Gaussian mode both in the radial and in the axial direction. This allows for taking into account the position distribution of the atomic sample. The polarization of the trapping laser is simulated using the Jones matrix formalism and by explicitly considering every wave plate used. Here, not only their rotation degree of freedom is considered but also a possible error of their retardation (a small tilting angle with respect to the beam axis can easily cause a retardation error on the order of 1% of the ideal value). Finally, even the calculated magic wavelength is not assumed to be perfect. For simplicity the wavelength dependent proportionality factors $c_{xx,\rho}$ in equation 1.2.1 are computed only once. A wrong calculation of the magic wavelength is simply mimicked by varying the wavelength of the trapping laser and using the changed scaling factors (see figure 1.6), although the lattice wavelength is very well known experimentally.

The simulation of the full potential is used in the models presented in the next chapters and helps to identify the most critical experimental parameters.

Chapter 2

How microwave photons affect atomic motion

In our and in many other experiments microwave radiation is one of the standard tools for coherent manipulation of the spin state of trapped atoms. Concerning their motion, radio frequency or microwave fields are also employed for dressing an existing magnetic or optical potential. This approach is often used e.g. in evaporative cooling during the creation of a Bose-Einstein condensate [61, 62]. In recent experiments, dressed potentials are applied for the generation of more complex trapping topologies or state-dependent potentials [63, 64, 65, 66]. All these techniques work in the limit of strong radiation fields, where the Rabi frequency is much larger than the frequency spacing between the quantized vibrational states supported by the underlying potential. In particular, the above techniques are not aiming at the manipulation of atomic motion in the sense of coherent control of the populations of different vibrational states.

This kind of control is instead typically accomplished exploiting optical transitions. When the driving field is tuned in resonance with a so-called sideband transition, the motional state of the trapped atom undergoes a change of the vibrational quantum number according to the order of the sideband [67]. This technique, employing either a narrow bandwidth laser or two phase-locked lasers in Raman configuration, is popular for cooling trapped ions [24] and neutral atoms [9] close to the motional ground state. Starting from the ground state, it furthermore allows to arbitrarily manipulate and diagnose the vibrational state of trapped ions [37, 68, 69] and of neutral atoms trapped in optical lattices [70, 71, 72]. The motional control even lies at the heart of experimental procedures for entangling the internal states of a string of ions [27, 28]. Alternatively, the vibrational state can be manipulated by directly varying the trapping potential [73, 74, 75]

In the following I will show that the quantum mechanical motion of trapped neutral atoms can be manipulated using microwave radiation in combination with

spin dependent trapping potentials. Similarly to the laser-based technique, our system is probed via sideband spectroscopy. In fact, microwave-induced sideband spectra have already been observed for neutral atoms in a one-dimensional optical lattice [76] as well as for trapped ions [77]. In [78] coherent sideband transitions have been performed with neutral atoms in a three-dimensional lattice where, as in our experiment, the tunability of the sideband strength has been exploited to map the wave functions of the vibrational states. Our results are closely related to those presented in [78] but are obtained in a deeper optical lattice revealing the multilevel vibrational structure of the lattice potential.

2.1 Spectrum of trapped atoms

Transitions between quantized motional states Due to the Doppler effect, the center-of-mass motion of an atom has a great impact onto its interaction with electromagnetic radiation. Trapped atoms which periodically oscillate in a conservative potential consequently experience a periodically varying Doppler shift. Effectively, the atoms interact with a phase modulated electromagnetic field. Presuming the proper conditions the absorption and emission spectra exhibit a multiply peaked structure [67].

Quantum mechanically a more intuitive picture of the absorption/emission process can be drawn [67]. Here, the center-of-mass motion is modeled using discrete vibrational states of the trapping potential. The total Hilbert space relevant for the electromagnetic transitions is spanned by the product states of spin and motional degrees of freedom

$$|F, m_\mathrm{F}\rangle \otimes |n\rangle_{F,m_\mathrm{F}} =: |F, m_\mathrm{F}, n_{F,m_\mathrm{F}}\rangle. \tag{2.1.1}$$

Here, F and m_F label the atomic hyperfine states and n enumerates the vibrational states of the trapping potential. Note that in general atoms in different hyperfine states are trapped by different potentials as the trapping mechanism might itself dependent on the electronic state. This means that the vibrational states $|n\rangle_{F,m_\mathrm{F}}$ and $|n'\rangle_{F',m'_\mathrm{F}}$ are not necessarily identical even if their quantum numbers might be equal ($n = n'$). The energy of a product state is defined by the sum $E_{F,m_\mathrm{F}} + E_{n_{F,m_\mathrm{F}}}$. Figure 2.1 illustrates the energy level scheme in case of Cesium trapped in our 1D lattice potential.

In general, an electromagnetic field $\mathcal{F}$ which couples two internal states may also change the vibrational state. If the linewidth of the electromagnetic transition is much smaller than the energetic spacing between vibrational states, the field can be tuned in resonance with any transition between the initial state $|F, m_\mathrm{F}, n_{F,m_\mathrm{F}}\rangle$ and the final state $|F', m'_\mathrm{F}, n'_{F',m'_\mathrm{F}}\rangle$ (see figure 2.1). In addition to the carrier transition,

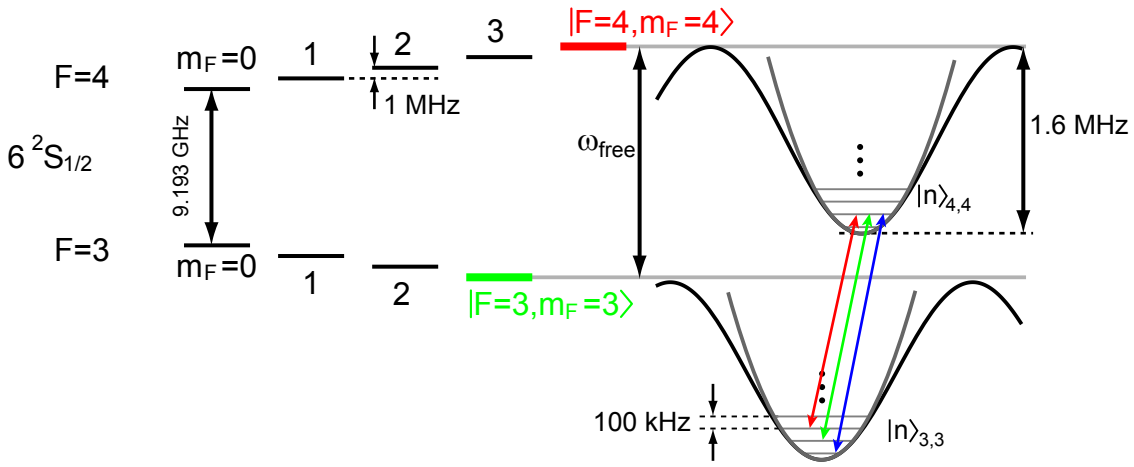

Fig. 2.1: Energy level scheme for the combined system consisting of internal atomic states $|F, m_\mathrm{F}\rangle$ and vibrational states $|n\rangle_{F,m_\mathrm{F}}$. Each of the hyperfine states now possesses a relatively dense energetic substructure. The frequency scales indicate the parameters used in our experiment. For simplicity, the sinusoidal optical lattice can be approximated by a harmonic potential with its well known eigenstates. When the linewidth of the driving field is narrow enough, it can be selectively tuned to a sideband transition with a desired $\Delta n =$, e.g. $+1$ (red), 0 (green), -1 (blue).

for which the motional quantum number does not change ($\Delta n = n' - n = 0$), sideband resonances with $\Delta n \neq 0$ can be observed on the blue and on the red side of the carrier. Their frequency spacing is defined by the energetic ladder of the vibrational states. This yields the explanation for a multiply peaked sideband spectrum, in agreement with the energy conservation law.

The strength of any sideband transition is determined by matrix elements describing the interaction between light and atom similar to that in equation 1.1.3. They now, however, take into account the external degree of freedom of the atomic center-of-mass motion [67, 54]

$$\begin{aligned}\hbar\Omega_{\mathrm{R}_{n,n'}} &= \langle F', m'_\mathrm{F}, n'_{F',m'_\mathrm{F}}|\hat{H}_\mathcal{F}\,\exp(i\Delta k\,\hat{x})|F, m_\mathrm{F}, n_{F,m_\mathrm{F}}\rangle \\ &= \langle F', m'_\mathrm{F}|\hat{H}_\mathcal{F}|F, m_\mathrm{F}\rangle\,\langle n'_{F',m'_\mathrm{F}}|\exp(i\Delta k\,\hat{x})|n_{F,m_\mathrm{F}}\rangle \\ &= \hbar\,\Omega_\mathrm{bare} \times \text{Franck-Condon factor}, \end{aligned} \tag{2.1.2}$$

The atom field interaction hamiltonian $\hat{H}_\mathcal{F}$ acts exclusively onto the internal degree of freedom. For an optical electric (microwave-induced magnetic) dipole transition

it reads $\hat{H}_{\mathcal{F}} = \hat{\boldsymbol{d}}\,\boldsymbol{E}$ ($\hat{H}_{\mathcal{F}} = \hat{\boldsymbol{\mu}}\,\boldsymbol{B}$). The atomic electric (magnetic) dipole moment operator is labeled by $\hat{\boldsymbol{d}}(\hat{\boldsymbol{\mu}})$ and $\boldsymbol{E}(\boldsymbol{B})$ is the electric (magnetic) component of the driving field. The field amplitude is considered to be spatially constant across the size of the atom. The first matrix element on the right hand side thus determines the coupling strength between the internal states in case the atomic motion is neglected or in case of a free atom. The coupling is quantified by the corresponding Rabi frequency which is denoted by Ω_{bare}.

The field-induced mechanical action on the external degree of freedom is described by the second matrix element where $\hat{x}$ is the position operator of the atomic center-of-mass motion. This matrix element acts as a scaling factor which specifies the relative strength of all possible sideband transitions. It thus also imposes selection rules when the corresponding spatial wave function overlap vanishes. In analogy to molecular physics the scaling factor due to the wave function overlap is often named Franck-Condon factor [79]. For molecules, according to the Born-Oppenheimer approximation [80], the wave function for the center-of-mass motion of the constituent atoms and that for their internal constituents (electrons and the atomic core), can also be factorized.

Sidebands due to photon recoil A prominent example for a radiation-induced mechanical impact is the recoil of an absorbed laser photon followed by the reemission of a second photon. After each scattering event the expectation value for the atomic momentum changes by $\hbar\Delta k$, where $\Delta k = k_{\text{abs}} - k_{\text{em}}$ is the difference between the wave vectors of the absorbed and the emitted photon (see equation 2.1.2). This is the basis of laser cooling which provides cold atomic samples for a variety of precision measurements. For atoms already trapped by a conservative potential the recoil process provides the required mechanism for the manipulation of the vibrational state. Identifying the operator $\exp(i\,\Delta k\hat{x})$ as the momentum translation operator $T_{\Delta p}$ with

$$T_{\Delta p}|\psi(p)\rangle = \exp(i\,\Delta k\hat{x})|\psi(p)\rangle = |\psi(p-\hbar\Delta k)\rangle = |\psi(p-\Delta p)\rangle \tag{2.1.3}$$

leads to a simple interpretation of the matrix element defining the Franck-Condon factor. Due to the recoil $\Delta p = \hbar\Delta k$ the initial center-of-mass wave function $\psi(p)$ is shifted in momentum space (see figure 2.2 (a)). The overlap of the shifted wave function with the vibrational eigenstates of the target potential then acts as a scaling factor for the Rabi frequency of each transition $|n_{F,m_{\text{F}}}\rangle \leftrightarrow |n'_{F',m'_{\text{F}}}\rangle$. Note that recoil-induced sidebands can be generated even when $|n_{F,m_{\text{F}}}\rangle = |n_{F',m'_{\text{F}}}\rangle$ holds, corresponding to the case where the trapping potential is not state-dependent.

For the experimental observation of resolved sideband transitions employing

lasers a significant effort must be expended for the realization of a suitable narrow linewidth transition. This is achieved by either choosing a dipole-forbidden transition driven by a well stabilized laser [69], or by driving a two-photon transition between long-lived atomic hyperfine states in the ground state employing two phase-locked lasers in Raman configuration [68, 81].

2.1.1 Microwave-induced sidebands

For neutral atoms the choice of the long-lived states is basically limited to the ground state manifold. In this case, a direct transition between them has a frequency in the radio frequency or microwave domain. Turnkey microwave generators providing very narrow line widths can easily be used for the experimental manipulation of the hyperfine state (see section 1.1.2). But, compared to optical photons, microwave photons possess a recoil which is five orders of magnitude smaller. This is the reason why optical transition are preferred for the generation of sidebands. Nevertheless, microwaves may influence the center-of-mass motion of trapped atoms, in case, a state-dependent potential is present.

Sidebands due to a state-dependent potential When the recoil of the photon is negligible the momentum translation operator is equal to unity and the Franck-Condon factors in equation 2.1.2 read $\langle n'_{F',m'_\mathrm{F}} | \, n_{F,m_\mathrm{F}} \rangle$. If the two potentials U_{F,m_F} and U_{F',m'_F} are identical this equation evaluates to zero for all transitions which change the vibrational quantum number. If they are not identical the corresponding energy eigenstates are per definition non-orthogonal which yields finite Franck-Condon factors.

In general, the spatial wave function overlap can be directly calculated using a specific representation of the wave functions, e.g. in position space. In the special case, when the potentials U_{F,m_F} and U_{F',m'_F} are displaced relative to each other by the distance Δx but otherwise possess the same shape the wave function overlap can be cast into a form equivalent to that of the recoil case (see figure 2.2 (a)). To illustrate this we define the spatial translation operator

$$\begin{aligned} &T_{\Delta x}|\psi(x)\rangle := \exp(-i\,\Delta x\,\hat{p}/\hbar)|\psi(x)\rangle = |\psi(x-\Delta x)\rangle \\ &\text{with } \; T^\dagger_{\Delta x} = T_{-\Delta x} \end{aligned} \tag{2.1.4}$$

where $\hat{p}$ labels the atomic center-of-mass momentum operator and † denotes the conjugate transpose operation.

In fact, the matrix for the shift operator at the same time provides the matrix

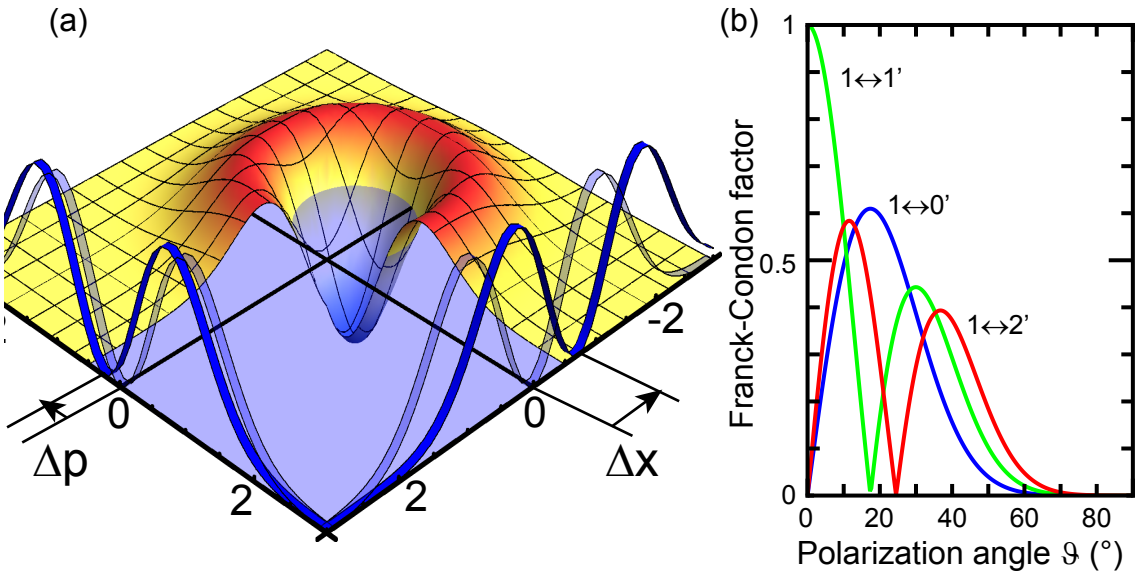

Fig. 2.2: (a) Wigner function representation of original and displaced 1D harmonic oscillator $|n=1\rangle^{\mathrm{ho}}$-wave functions. The corresponding usual probability distributions in the spatial and in the momentum domain are illustrated by thick silhouettes. For comparison the probability distributions of the unshifted state is indicated by pale silhouettes. The scales are given in terms of the size of the ground state x_0 and p_0, respectively. (b) The absolute value of the Franck-Condon factor depending on the polarization angle of the lattice for the same sideband transitions as indicated in figure 2.1.

for the basis transformation $|n_{F',m'_{\mathrm{F}}}\rangle = T_{\Delta x}|n_{F,m_{\mathrm{F}}}\rangle$. Using this operator the Franck-Condon factor for the case of displaced potentials can be written as

$$\langle n'_{F',m'_{\mathrm{F}}}|n_{F,m_{\mathrm{F}}}\rangle = (T_{\Delta x}|n'_{F,m_{\mathrm{F}}}\rangle)^{\dagger}\,|n_{F,m_{\mathrm{F}}}\rangle = \langle n'_{F,m_{\mathrm{F}}}|T^{\dagger}_{\Delta x}|n_{F,m_{\mathrm{F}}}\rangle. \tag{2.1.5}$$

For the general case, a combined translation operator

$$T_{\Delta x,\Delta p} := \exp(i(-\Delta x\,\hat{p}/\hbar + \Delta k\,\hat{x})) \equiv T_{\Delta x}T_{\Delta p}\,\exp(i\,\Delta x\Delta k/2) \tag{2.1.6}$$

can be defined which describes an arbitrary translation in phase space. Here, the operator identity $e^{A+B} = e^{A}e^{B}e^{-[A,B]/2}$ was used. Up to the phase factor $\exp(i\,\Delta x\Delta k/2)$ the general translation operator is identical to a successive application of $T_{\Delta x}$ and $T_{\Delta p}$.

In the usual Schrödinger picture the quantum mechanical states are defined either by their spatial or their momentum representation. In these bases it is difficult to illustrate the action of the $T_{\Delta x,\Delta p}$ operator. A more convenient formalism for the description of the quantum mechanics in phase space can be given using Wigner functions [82]. For a pure state $|\psi(x)\rangle$ in the spatial representation the corresponding Wigner function is defined by

$$W(x,p) = \frac{1}{2\pi\hbar}\int_{-\infty}^{\infty} d\xi\, \exp(-i\,\frac{p}{\hbar}\xi)\,\psi^*(x-\xi/2)\,\psi(x+\xi/2). \tag{2.1.7}$$

As an example, the Wigner function of the $n = 1$ 1D harmonic oscillator state is depicted in figure 2.2 (a). The meaning of the Wigner function is that of a pseudo probability distribution (pseudo because it can take on negative values). The usual probability distributions in the spatial and in the momentum domain are obtained by integrating over the respective conjugate degree of freedom. Figure 2.2(a) illustrates the simultaneous shift of the wave function in the spatial and in the momentum domain. It also points towards the fact that the overlap of the shifted and the unshifted wave functions depends on the total shift defined by the quadratic sum of the spatial and the momentum displacement.

Generalized Lamb-Dicke-parameter In case of a harmonic oscillator potential the Franck-Condon factor between two eigenstates which are shifted with respect to each other can be calculated analytically. For illustration, we consider a 1D harmonic oscillator potential which is a very good approximation for the lowest vibrational states of individual wells in our optical lattice. The explicit formulas for the orthonormal vibrational eigenstates $|n_{\rm ho}\rangle$ in the spatial and in the momentum representation read

$$|n_{\rm ho}\rangle = (2^n n!\sqrt{\pi}\,x_0)^{-1/2}\exp(-\frac{1}{2}(\frac{x}{x_0})^2)\mathrm{H}_n(\frac{x}{x_0}) \tag{2.1.8}$$

$$= (-i)^n(2^n n!\sqrt{\pi}\,p_0)^{-1/2}\exp(-\frac{1}{2}(\frac{p}{p_0})^2)\mathrm{H}_n(\frac{p}{p_0}) \tag{2.1.9}$$

$$\text{with}\;\; x_0 = \sqrt{\hbar/(M\omega)}\;\; \text{and}\;\; p_0 = \sqrt{\hbar M\omega}, \tag{2.1.10}$$

where $\hbar$ denotes the Planck-constant, M is the mass of the atom, ω is the oscillation frequency of the harmonic potential and $\mathrm{H}_n(x)$ is the $n^{\rm th}$ order Hermite-polynomial. The abbreviations x_0 and p_0 denote the e^{-1}-probability-spread of the ground state wave function in position and in momentum space, respectively.

The calculation of the Franck-Condon factor following the analytic procedure presented in [67] (see also [32, 83]) yields (up to the phase factor for the combined phase space shift operator mentioned above)

$$\begin{aligned} \langle n'_{\mathrm{ho}}|T_{\Delta x,\Delta p}|n_{\mathrm{ho}}\rangle &= \exp(-\frac{|\eta|^2}{2})\sqrt{\frac{n_<!}{n_>!}}\,(i\,\eta^*)^{|\Delta n|}\,\mathrm{L}_{n_<}^{|\Delta n|}(|\eta|^2)\,(-1)^{\max(\Delta n,0)} \\ \eta &:= \frac{\Delta k\,\hbar}{\sqrt{2}\,p_0}+i\,\frac{\Delta x}{\sqrt{2}\,x_0} = \frac{\Delta k\,x_0}{\sqrt{2}}+i\,\frac{\Delta x\,p_0}{\sqrt{2}\,\hbar}\,. \end{aligned} \tag{2.1.11}$$

Here, $\mathrm{L}_n^a(x)$ denote the generalized Laguerre-polynomials, $n_< = \min(n', n)$, $n_> = \max(n', n)$ and $\Delta n = n' - n$. The parameter η is the generalization of the Lamb-Dicke parameter which is typically used to quantify the strength of sideband transitions. It relates the displacement of the wave function caused by the recoil of a photon to the momentum size, and the potential displacement to the spatial size of the vibrational ground state, respectively. Due to the definition of η as a complex number, the two degrees of freedom enter the Franck-Condon factor as conjugate variables as was suggested by the phase space representation in figure 2.2. Note that the common definition of the η-parameter reads $\eta = \Delta k\,\tilde{x}_0$ with $\tilde{x}_0 = x_0/\sqrt{2}$. The definition of the wave function size as in equation 2.1.10 is however more symmetric in the variables x and p.

In our experimental setup the η-parameter due to the recoil of a molasses photon amounts to a maximum of $\eta = 0.13$ with respect to the axial degree of freedom (using $\Delta k = 2\pi/\lambda_{\mathrm{molasses}}$). This η-value has the typical order of magnitude also present in other experiments [9, 37] where sideband transitions of up to the third order are observable [84]. In this so-called Lamb-Dicke regime obeying the condition $\eta \ll 1$, formula 2.1.11 is usually approximated by its first order Taylor-series with respect to η [67, 77]. Typically, only the first order sidebands are used in this regime for which the Franck-Condon factors scale as $\langle n+1|n\rangle = \sqrt{n}\,\langle 1|0\rangle$.

For comparison, the maximum separation possible between two adjacent potential wells in our experiment is limited by the periodicity of the optical lattice. Taking the value $\Delta x = \lambda_{\mathrm{lat}}/4$ leads to the maximum value of $\eta = 6$. For such large values the full formula 2.1.11 must be used for the calculation of the Franck-Condon factors. For typical experimental parameters, Figure 2.2(b) illustrates the dependence of the Franck-Condon factor on the polarization angle ϑ for the carrier and the first red and blue sideband transitions starting in the initial state $|n = 1\rangle$. It shows that the lattice displacement can be adjusted such, that the Rabi frequency for the sidebands is as large as half of the maximum value given by Ω_{bare}. Furthermore, the distance between adjacent potential wells can be set significantly larger than the size of the deeply bound vibrational states. This allows for a scan of the entire motional wave

function (see section 2.5).

2.1.2 Measured sideband spectrum

For the experimental observation of the sideband spectrum the same experimental sequence as described in section 1.1.1 is used. The only modification is a fixed lattice displacement during the microwave pulse. Without displacement only one resonance peak appears which marks the position of the carrier for overlapped potentials (see figure 2.3 (a)). Two additional resonances on the red and on the blue side appear (panels (b) and (c)) when the polarization angle is rotated to $\vartheta = 11.6°$ so that the potential shift during the microwave pulse amounts to $\Delta x = 24\,\mathrm{nm}$. As the atoms are initially prepared in the upper hyperfine ground state $|44\rangle$ the blue (red) sideband corresponds to a reduction (increase) of the motional quantum number by one.

The starting condition for the spectrum in panel (b) is a thermal ensemble with a temperature of about $10\,\mu\mathrm{K}$ so that the mean vibrational quantum number along the axial direction amounts to $\bar{n} = 1.2$. This implies, that due to the distribution of the atomic ensemble over the vibrational states every observed resonance peak incorporates a contribution from several transitions each starting from a different vibrational state. For all transitions contributing to one peak the change of the vibrational quantum number is the same but due to different Franck-Condon factors the respective strengths are nonequal. The applied microwave pulse fulfills the π-pulse condition only for the $|44, n = 0\rangle \leftrightarrow |33, n = 1\rangle$ transition. All other transitions thus exhibit other pulse areas and the observed peak heights result from a thermally weighted sum over the individual transitions. As will be described in section 2.2.1 sideband transitions of the same order also exhibit slightly different resonance frequencies. This explains the slightly larger width and a small shift of the peaks compared to the spectrum in panel (c).

After cooling the motion along the lattice axis using the technique described in section 3.1 the blue sideband is strongly suppressed (see panel (c)). When almost all atoms are initially in the ground state $|44, 0\rangle$ and only few of them in the first excited state $|44, 1\rangle$ the carrier is dominated by the $|44, 0\rangle \leftrightarrow |33, 0\rangle$, the red sideband by the $|44, 0\rangle \leftrightarrow |33, 1\rangle$ and the blue sideband by the $|44, 1\rangle \leftrightarrow |33, 0\rangle$ transition, respectively. The reduction of the blue sideband is thus reasonable, as there is no transition existing which still reduces the vibrational quantum number starting from the ground state. The height of the red sideband is maximized by choosing the π-pulse condition for the $|44, n = 0\rangle \leftrightarrow |33, n = 1\rangle$ transition. Due to residual broadening mechanisms (see section 2.4) the spin rotation using this sideband is limited to approximately the same efficiency as using the carrier transition in panel (a). The relative height of the carrier and the red sideband peak reflect the ratio

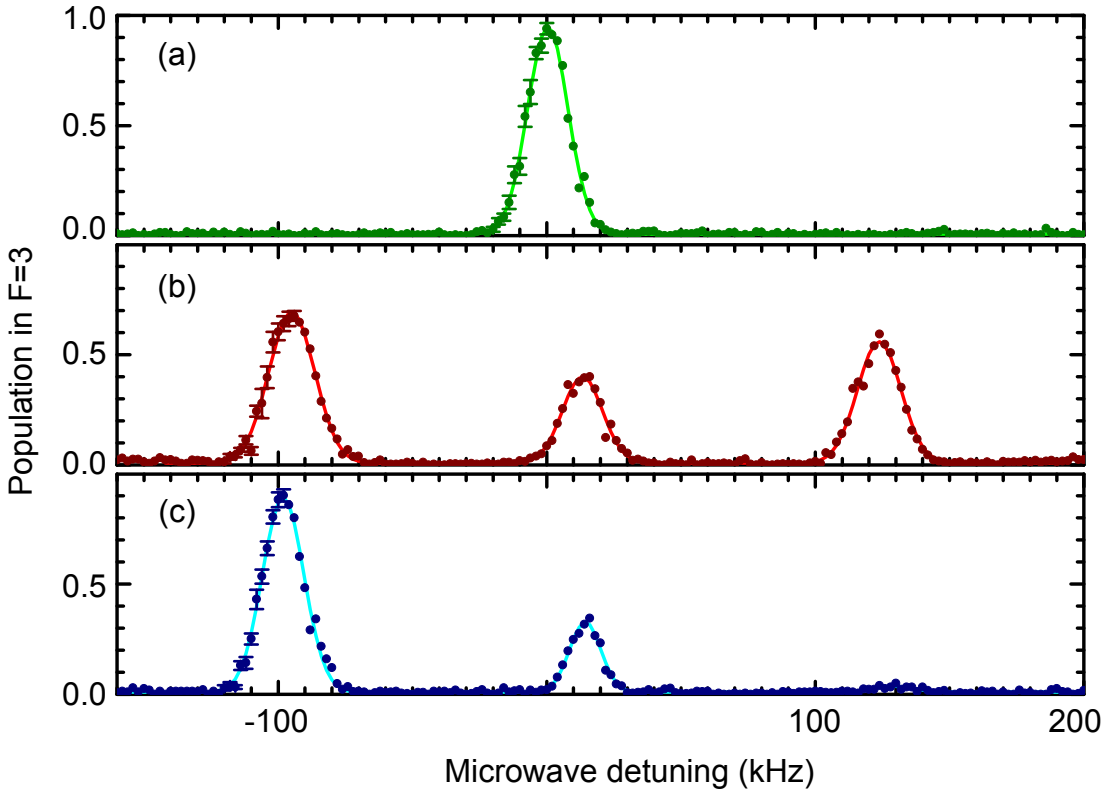

Fig. 2.3: Sideband spectrum: (a) In case of strictly overlapped potentials the sidebands are not detectable. (b) When a displacement of $\Delta x = 24\,\mathrm{nm}$ ($\vartheta = 11.6°$) is applied the first blue and red sideband appear. The red (blue) sideband corresponds to the increase (decrease) of the vibrational quantum number by $\Delta n = 1$. (c) When only the vibrational ground state is populated the vibrational quantum number cannot be further reduced. As a consequence the blue sideband almost disappears. From the relative strength of the red and the blue sideband we deduce a ground state population of 97 % (see section 3.1.

between the corresponding Franck-Condon factors. From the measured peaks it follows that the pulse area for the carrier amounts to $1.6\,\pi$. This is in good agreement with the theoretical expectation apart from a small deviation of the polarization angle ϑ. A possible explanation might be that due to the crosstalk between computer output channels the control voltage during the microwave pulse was transiently reduced by 5 mV (see page 7).

The resonance positions of the red sideband ($\Delta f_r = (112.5 \pm 0.5)\,\mathrm{kHz}$) and the blue sideband ($\Delta f_b = 115 \pm 2.5\,\mathrm{kHz}$) relative to the carrier transition in panel

(c) directly correspond to the spacing of the vibrational states. Here, Δf_r reflects the energy spacing of the U_{33}-potential while Δf_b that of the U_{44}-potential. The accuracy of the measured frequency spacings allows for a precise measurement of the axial trap depth (the trap contrast). As will be explained later on, for full quantitative understanding it is necessary to take into account the anharmonicity of the lattice potential (section 2.2.1), the thermal motion along the radial degree of freedom (section 2.4) and the peak shift due to dressing by microwave radiation (section 2.2.2).

The following experiments described in this chapter are performed with an atomic sample which is ground state cooled.

Axial oscillation frequency For a more complete picture we have performed an alternative measurement of the vibrational energy spacings. It is based on motional excitation when the lattice jitters with a small amplitude around a mean displacement Δx. When the jitter frequency coincides with the vibrational spacing the atoms in general get resonantly heated [85, 86]. In the harmonic approximation the relation between the axial trap contrast and the axial oscillation frequency is given by $\omega_{\mathrm{ax}} = 2\pi\sqrt{2U_{\mathrm{ax}}/(M\lambda_{\mathrm{lat}}^2)}$. The jittering method does not rely on an electromagnetic transition between hyperfine states and can thus be performed separately for each $|F, m_F\rangle$ state. Furthermore, the displacement at which the measurement is performed can be varied arbitrarily in contrast to the sideband method where the Franck-Condon factors constrain the useful measurement range. On the other hand it only provides information about the axial potential contrast. The radial confinement and thus the total trap depth can be quite different from the axial one, in particular for displaced potentials.

Experimentally, the jittering of the optical lattice was accomplished using the EOM-setup for the potential movement. For precise control of the jitter frequency the output of a function generator was added to the computer output using an analog adder. The jitter amplitude (2 nm) and the number of the jitter oscillations (100 cycles) where kept constant while the mean displacement and the jitter frequency where varied. As the atomic sample was initially in the ground state the strength of the blue sideband is a sensitive measure for the excitation. The jitter amplitude and its duration where chosen such that the blue sideband just starts to appear when the jitter becomes resonant. Its height is at most 0.4 (corresponding to 40 % of all atoms) so that only the first excited state is significantly populated.

Due to the pure initial vibrational state the motional excitation in this experiment can be considered very coherent. In fact, for a harmonic potential jittering excites the atoms to a coherent motional state [73]. This state describes an oscillating wave packed and thus is closely related to the classical picture. It has a poissonian distribution over the number states. Coherent excitation of motional

states is widely exploited in current experiments with trapped atoms [87, 74, 88, 89].

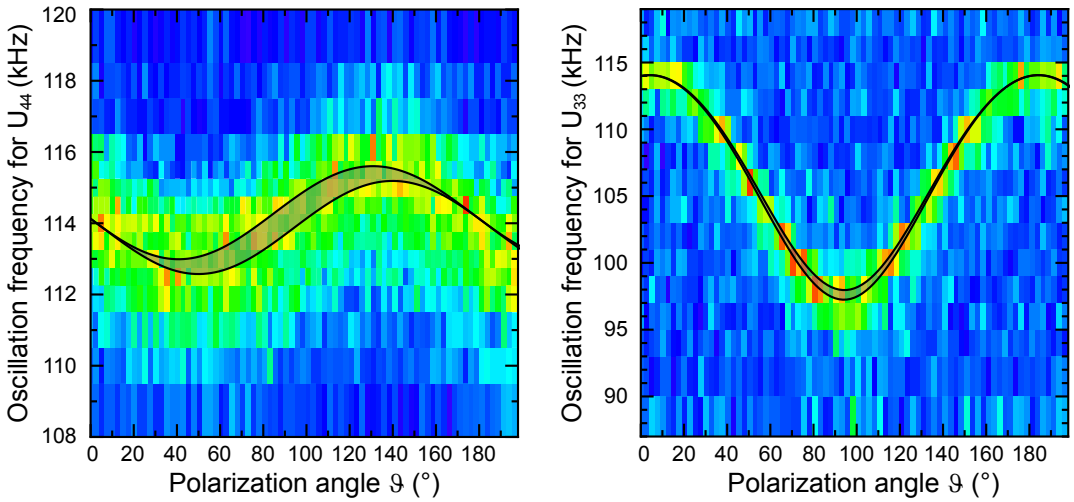

Fig. 2.4: Oscillation frequency of the trapping potentials U_{44} and U_{33}. The color coded data indicate the height of the blue sideband after exciting the atoms using resonant jittering of the lattice. As expected from the calculations in section 1.2, the oscillation frequency of the U_{33}-potential varies with the applied displacement whereas it remains constant for the U_{44}-potential. The theoretical curves result from our lattice potential model taking into account experimental misalignments (see text).

The measured oscillation frequencies for the U_{44} and the U_{33}-lattice shown in figure 2.4 are in good quantitative agreement with the theoretical expectation. Comparing the oscillation frequencies of (114 ± 0.5) kHz at small displacement with the positions of the first sidebands in the case of a ground state cooled sample also shows a good agreement between both measurements. The small but statistically significant discrepancy between the results of the two techniques can very well be explained by the fact that due to dressing microwave resonances are systematically shifted in figure 2.3 (see section 2.2.2). Unfortunately, the uncertainty of the daily alignment can in general lead to greater discrepancies between different data sets so that this conclusion cannot be completely proven.

In figure 2.4 the small but systematic deviations from the ideal theory reveal a slight distortion of the lattice potential. The most characteristic one is that instead of an ideally constant oscillation frequency of the U_{44} potential it sinusoidally varies with the polarization angle ϑ. In order to figure out potential reasons we exploit the model of the lattice potential outlined on page 21. Assuming a non-ideal retardation of the wave plates $\mathrm{wp4_r}$ and $\mathrm{wp2_r}$ (see figure 1.1) reproduces the observed distortion. An additional small rotational misalignment of the half wave plate $\mathrm{wp2_r}$

(0.1°) and/or assuming that the calculated value for the magic wavelength might be slightly wrong (-0.1 nm), makes the fit to the data perfect. The theoretical lines in figure 2.4 indicate variations on the order of ±0.1° and ±0.1 nm, respectively. The uncertainty of the magic wavelength is hereby within the confidence intervals of experimental oscillator strengths entering the calculation of the magic wavelength.

As well as for the microwave spectrum in figure 2.3 the trap anharmonicity and the radial motion must be considered for an accurate interpretation of the observed oscillation frequencies (see sections 2.2.1 and 2.4). Taking this effects into account, the potential contrast along the trap axis in case of unshifted potentials amounts to (80.8±0.7) μK in this measurement. This is in good agreement with the expected trap depth calculated from the knowledge of the beam waist and of the laser power used.

Due to the anharmonicity of the trap it might even be possible to extend this technique by jittering the lattice at higher harmonics of the oscillation frequency (for an ideal harmonic potential only one resonance exists). Another option might be to initially prepare the atomic sample in an excited vibrational sate using sideband transitions. This way, the jittering technique may be exploited as an independent spectroscopic tool for the investigation of the vibrational level scheme. A further application might be a state-selective heating of atoms, as for a polarization angle of ϑ=90° the oscillation frequencies are quite different. This would provide an alternative technique for the currently used state-selective push out. In particular, this method potentially allows to discriminate between different magnetic sub-levels.

Movement of the entire spectrum Coming back to the spectra in figure 2.3, we notice that the position of the carrier in the two sideband spectra has shifted to the blue with respect to the carrier transition at zero displacement. According to the ideal model, the depth of the U_{44} potential remains constant and that of the U_{33} potential is expected to become shallower. Due to the differential light shift [57] the energy gap between the upper and the lower hyperfine states in this case becomes shorter and a spectrum shift solely to the red side is expected .

A scan presented in figure 2.5 gives a more complete picture. It shows the position of the sideband spectrum depending on the polarization angle ϑ. In order to allow a quick measurement the sample was not ground state cooled at the beginning. This procedure benefits from the fact that each resonance peak consists of several pure transitions starting in different vibrational states. When the displacement becomes substantial compared to the lattice constant the transitions starting in higher vibrational states have still a considerable strength due to their larger spatial extension. Otherwise the e.g. carrier transition $|44,0\rangle \leftrightarrow |33,0\rangle$ would vanish for $\vartheta \gtrsim 35°$.

The observed sinusoidal shift of the spectrum depending on the displacement

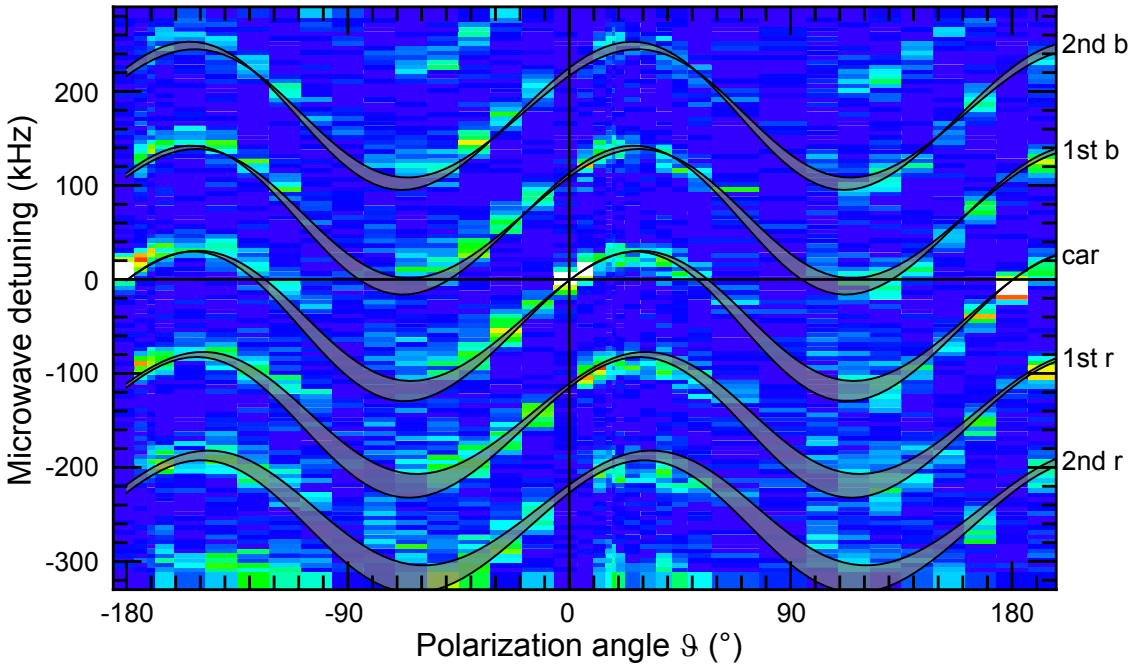

Fig. 2.5: The entire sideband spectrum shifts during the variation of the displacement. This provides a sensitive measure for the variation of the differential light shift $U_{44} - U_{33}$ and thus provides information about the total trap depth and not only about the axial trap contrast. The solid lines indicate the position of each transition predicted by a simulation including experimental imperfections. For each transition two lines are drawn, one for the atoms in the ground state and one for the second excited vibrational state.

qualitatively agrees with the expectation of an ideal setup. But, it also reveals pronounced and very systematic deviations: a perfectly aligned setup would result in a twice as large shift amplitude and the carrier would never shift to the blue side. The full model of the lattice potential (page 21) again nicely reproduces the characteristic features. Here, the non-ideal wave plates turn out to be responsible for the shift to the blue side. In order to explain the smaller shift amplitude the rotation angle of the half wave plate $\mathrm{wp2_r}$ must be assumed to be -0.5°. Although this rotation angle is small and hardly noticeable during the optical alignment it has a great influence on the relative depth of the two lattice components. Note that a measurement of the oscillation frequencies for the same situation would as well reveal a strong deviation from the ideal setup: The oscillation frequencies for *both* trap components would vary as in figure 2.4(b) but with half the amplitude.

The theoretical curves shown indicate the spread caused by the thermal distribution among the vibrational states which is now a drawback. Note that at least the

third vibrational state is significantly populated in the beginning as the third blue sideband is clearly visible. The measurement precision can be improved by conducting the same scan for several pure vibrational states. Nevertheless, despite thermal broadening the presented measurement provides reliable quantitative information about the total trap depth and not only the axial trapping contrast and helps to understand systematic distortions.

2.2 Model for sideband transition in a periodic potential

Until now the frequency range of the spectrum was restricted to the first few sidebands. According to equation 2.1.11, though, by increasing the displacement Δx the Franck-Condon factor for any high order sideband transition can be adjusted to approximately the same value as that for the first order sideband transition. Motivated by this we have recorded a wide range spectrum which indeed exhibits sideband transitions of up to the 14^{th} order (see figure 2.10). For the quantitative analysis of this data we have to give up the harmonic approximation for the axial lattice confinement. First, the real potential is not infinitely high and thus supports only a finite number of bound states. Second, due to the periodicity of the potential the maximum possible displacement is restricted to half the lattice site separation $\Delta x = \lambda_{\text{lat}}/4$. A more accurate theoretical treatment is given by the band structure model borrowed from the condensed matter physics. Before I continue to discuss measured data I briefly introduce how this theoretical frame is used in our case.

The second extension concerns microwave transitions between hyperfine states taking into account the vibrational manifold. As the maximum Rabi frequency of $2\pi\,59\,\text{kHz}$ in our experiment is of the same order of magnitude as the frequency separation between the vibrational states off-resonant excitation of several sideband transitions is significant. In order to consider this effect the Schrödinger equation 1.1.2 for a spin-$\frac{1}{2}$-particle and the Schrödinger equation for the atomic motion 2.2.1 are combined to a joined spinor equation.

2.2.1 Band structure model

In condensed matter physics [90, 91] the band structure model is the basis for the theoretical description of electron motion in presence of the periodic potential generated by the atomic cores in a crystal. It results from a reformulation of the Schrödinger equation when it is adapted to a hamiltonian with a periodic potential.

I use it here for the calculation of the eigenenergies and the corresponding motional eigenstates of our 1D-lattice [92, 56]. More precisely, we are only interested in the vibrational states which are bound and thus have negative energy eigenvalues.

The main trick for the adaptation of the Schrödinger equation

$$H_{\mathrm{lat}}\,\psi(x,t) \equiv \left(\frac{\hat{p}}{2\,M} + V_{\mathrm{lat}}(\hat{x})\right)\psi(x,t) = i\hbar\frac{\partial}{\partial t}\,\psi(x,t) \tag{2.2.1}$$

to the periodic potential problem is naturally the use of the discrete Fourier transform. Due to its periodicity the 1D lattice potential can thus always be represented by the Fourier sum

$$V_{\mathrm{lat}}(x) = \sum_{m\,\epsilon\,\mathbb{Z}} V_{mg_0}\exp(i\,mg_0x). \tag{2.2.2}$$

Here, mg_0 ($m\,\epsilon\,\mathbb{Z}$) label the vectors of the reciprocal lattice whereby $g_0 = 2\pi/a_{\mathrm{lattice}}$ is the smallest nonzero reciprocal vector and a_{lattice} is the spatial periodicity of the lattice. Using this notation the first Brillouin zone is defined by $[-g_0/2, g_0/2]$. The relationship between the reciprocal vector g_0 and the wavelength of the trapping laser is $g_0 = 2\pi/(\lambda_{\mathrm{lat}}/2) = 2k_{\mathrm{lat}}$. For a strictly real sinusoidal potential like that present in the experiment only the coefficients with the indices $m = \{-1; 0; 1\}$ are nonzero. Furthermore $V_{mg_0} = V^*_{-mg_0}$ holds (* denotes the complex conjugate).

Formally, the stationary Schrödinger equation is solved by the Bloch functions which are the energy eigenstates of the hamiltonian

$$\psi_{n,\kappa}(x) = \exp(i\,\kappa x)\sum_{m\,\epsilon\,\mathbb{Z}} c_{n,\kappa+mg_0}\exp(i\,mg_0x). \tag{2.2.3}$$

Each state is characterized by the discrete quantum number n, which enumerates the bands and by the wave vector (also called Bloch vector) κ which is chosen to be in the first Brillouin zone.

When the above equations are inserted into the stationary Schrödinger equation it can be formulated in the matrix form. This representation corresponds to the choice of the discrete set of plane waves $\exp(i\,mg_0x)$ to be the basis of the Hilbert space. For the sinusoidal lattice potential in our experiment the explicit matrix

equation reads

$$\begin{pmatrix} V_0 + \frac{\hbar(\kappa - 2\,g_0)}{2\,M} & V_{-g_0} & 0 & 0 \\ V_{g_0} & V_0 + \frac{\hbar(\kappa - g_0)}{2\,M} & V_{-g_0} & 0 \\ 0 & V_{g_0} & V_0 + \frac{\hbar\,\kappa}{2\,M} & V_{-g_0} \\ 0 & 0 & V_{g_0} & V_0 + \frac{\hbar(\kappa + g_0)}{2\,M} \end{pmatrix} \begin{pmatrix} c_{n,\kappa-2\,g_0} \\ c_{n,\kappa-g_0} \\ c_{n,\kappa} \\ c_{n,\kappa+g_0} \end{pmatrix} = E_{n,\kappa} \begin{pmatrix} c_{n,\kappa-2\,g_0} \\ c_{n,\kappa-g_0} \\ c_{n,\kappa} \\ c_{n,\kappa+g_0} \end{pmatrix} \tag{2.2.4}$$

For illustration purposes only a restricted equation is shown. In principle, the matrix of the Hamilton operator and the coefficients vector extend to plus and minus infinity but for the practical calculation their size is restricted to $\pm m_{\max} = 40$. For our typical experimental parameters the lattice potential supports not more than twenty bound states whose expansion coefficients $c_{n,\kappa+mg_0}$ are negligible for larger index values $|m| > m_{\max}$. Equation 2.2.4 has the form of an eigenvalue problem and can be easily handled using numerical solvers.

Energy level scheme By solving the eigenvalue equation for the potentials U_{44} and U_{33} using experimental parameters we obtain an energy level scheme similar to that in figure 2.6 (a). We identify three regimes of eigenvalues whose wave functions describe qualitatively different motional dynamics. For deeply bound states with large and medium negative eigenvalues the eigenenergy of each state $\psi_{n,\kappa}(x)$ is essentially independent of the Bloch vector κ resulting in practically infinitely sharp energy bands. The probability density $|\psi_{n,\kappa}(x)|^2$ is as well almost independent of κ. In principle, Bloch states have an infinite extent and exhibit unity spatial probability for each lattice site. Although this is an improper description for an atom confined to one specific potential well in the deeply bound regime the wave function of the Bloch states is very well localized around the lattice sites. The local wave function is a very good approximation for the real motional state which in particular is more accurate with comparison to the harmonic oscillator approximation. Due to this facts the Bloch vector κ is disregarded for the rest of this work and the quantum number for vibrational states is simply identified with the band index n.

For states with eigenenergies around zero the energy dispersion relation of κ leads to energy bands with a finite width. We need to consider this regime, which is related to tunneling phenomena, when we investigate sideband transitions of the highest order (see figure 2.10). For an increasingly higher band index n the bands become broader and the gap between neighboring bands shrinks. Finally, the bands

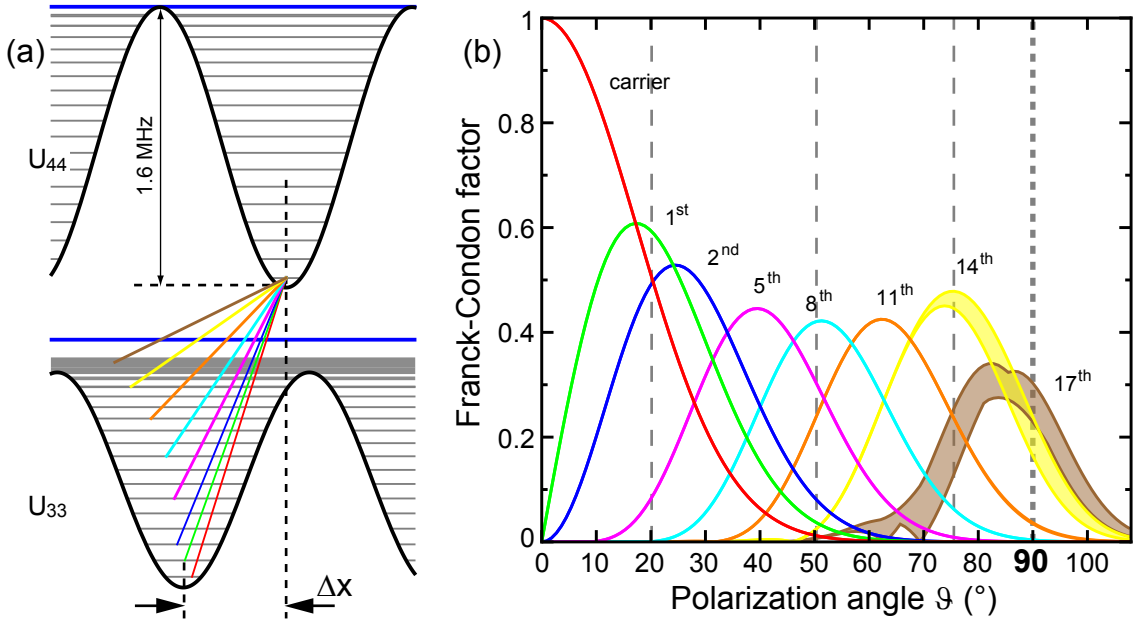

Fig. 2.6: (a) Energy level scheme for the Bloch states of the potentials U_{44} and U_{33}. (b) Dependence of the Franck-Condon factor on the polarization angle ϑ for a representative subset of transitions starting in the state $|44, 0\rangle$. For our experimental parameters the Franck-Condon factors for sidebands of all orders can be tuned to ≈0.5. Furthermore, for highest order transitions the Franck-Condon factors remain significantly large even for maximally displaced potentials (e.g. 11^{th} sideband). The thin dashed lines mark the three polarization angles at which the sideband spectra in figure 2.10 are measured.

effectively merge. In this regime the states describe freely moving atoms for which the influence of the lattice potential is negligible. Apart from atom loss this regime is irrelevant for atom manipulations investigated in this work.

For the U_{44}-potential our calculation predicts eighteen bands with negative energy (from $n = 0$ up to $n = 17$). Except for the uppermost three bands all of them exhibit a width smaller than 100 Hz, which is below the spectral resolution of the present experiment. For comparison, figure 2.6 shows as well eighteen bands of the U_{33} lattice. As its total depth and its standing wave contrast significantly decrease for a large displacement the bands $n = 16/17$ lie well above the axial potential barriers (for maximum displacement, we expect only the states $n = 0 - 15$ to be trapped).

For the correct interpretation of the first order sideband positions in figure 2.3 and of the measured oscillation frequencies in figure 2.4 it is worthwhile to take a closer look at the energy spacing between the motional ground state and the first

excited state. It turns out that for our experimental parameters it is smaller than the oscillation frequency based on the harmonic approximation by 2 kHz. This difference is easily resolved in our measurement which means that the Band model must be considered even for the first order sideband transition. This is also true for a precise determination of the axial trap contrast U_{ax} based on the sideband spectra.

The Franck-Condon factor Although the Bloch states in the deeply bound regime exhibit a well localized probability density around the lattice sites the interpretation of the Franck-Condon factor between two Bloch states requires some care. As long as the local wave function of the $|44\rangle$ potential overlaps with only one local wave function of the $|33\rangle$ potential, e.g. the left one (see figure 2.7 (a)), the overlap calculation based on the bare Bloch states yields a 'useful' Franck-Condon factor. In this case the two potential wells can be considered as an isolated pair and the atomic motion during the microwave operation is confined to such a double well [93].

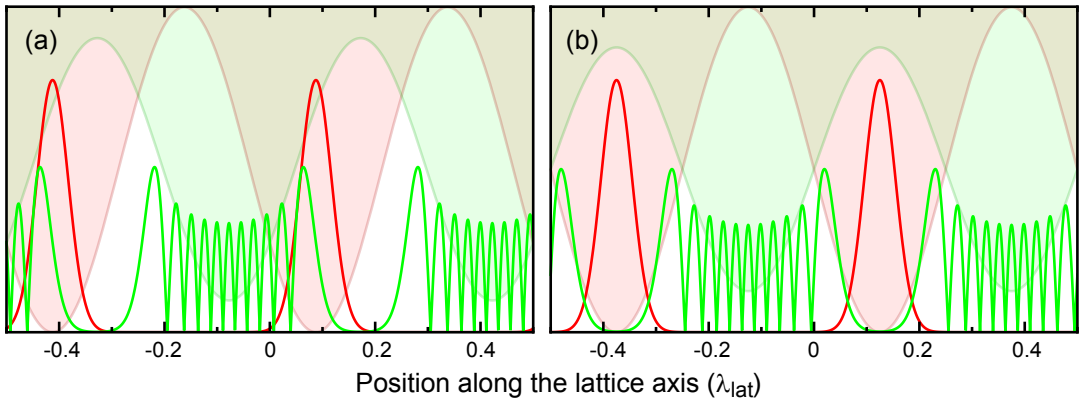

Fig. 2.7: Absolute value of the spatial wave function of the Bloch states $|44, 0\rangle$ and $|33, 10\rangle$. (a) Despite the large displacement the local ground state wave function overlaps only with the local wave function of the left neighboring lattice site. (b) When the displacement is maximum, however, the $|44, 0\rangle$ state has a significant overlap with both next neighbors. Note that the Bloch state $|33, 10\rangle$ has a negligible probability density between the wells and that the width of the corresponding Bloch band can be neglected.

The situation becomes more interesting when the local state of one potential has a significant overlap with the local states of both next neighbor lattice sites of the other potential. As illustrated in figure 2.7 (b) this already happens between states in the deeply bound regime including even the motional ground state. In this case, the Franck-Condon factor between two Bloch states does not provide the

correct scaling factor for the strength of a sideband. This is because of their infinite extent and because they possess a fixed phase relation between the lattice sites determined by the wave vector κ. Depending on κ the overlaps between the left and the right lattice sites interfere constructively or destructively yielding a single value. In contrast, for a real localized atom the coupling to each of the two sites is described by one individual Franck-Condon factor for the left direction and one for the right.

This problem can be solved using the Wannier states which provide a second complete set of wave functions for problems with periodic potentials [91, 90]. In contrast to Bloch states these wave functions are well localized: There is one Wannier function for each Bloch band and each lattice site. Their drawback is that they are not energy eigenstates. In the deeply bound regime, however, the Bloch bands are very sharply defined which is then also true for the energies of the corresponding Wannier states. In fact, in this case they very accurately approximate the local Bloch states around each lattice site. In this basis the Franck-Condon factors with respect to the left or with respect to the right next neighbor site can be calculated independently. In the deeply bound regime, though, very much the same result can be obtained by still using the Bloch states and by simply choosing the appropriate integration boundaries for the overlap calculation. This is the procedure which is used to calculate the Franck-Condon factors for the $|44, 0\rangle \leftrightarrow |33, n\rangle$ transitions shown in figure 2.6 (b). They have to be interpreted as one direction (left or right) factors. Note that a sharply defined Franck-Condon factor can even be obtained for the maximum displacement of $\Delta x = \lambda/4$ which corresponds to a polarization angle of $\vartheta = 90°$. This applies even more when a higher initial vibrational state is used instead of the ground state. Using microwave radiation the spatial wave function of the atom may thus be coherently split between the left and the right direction. As the target potential well again couples to its neighboring lattice sites the atom is coherently delocalized along the lattice and thus performs a quantum walk [22, 8].

Once the width of the Bloch bands cannot be neglected and the Bloch vector κ significantly determines the form of the probability distribution the overlap between wave functions naturally also becomes κ-dependent. This is indicated by the spread of the Franck-Codon factor lines for the highest order transitions in figure 2.6 (b). The calculation of the overlap between Wannier states instead of the procedure using Bloch states does not provide a better insight. As the Wannier states in this regime also have an extent much larger than one lattice site the overlap between two lattice sites again involves several Wannier states. Moreover, the Wannier states are not stationary and thus significantly evolve during the duration of the microwave pulse. In any case, independent of the basis used the picture of atoms transferred between discrete lattice sites is just not adequate in this limit. In conclusion, the calculation of the Franck-Condon factors relevant for this work can entirely be carried out in the

Bloch basis. This has the additional big advantage that the Schrödinger equation can be expressed in the eigenenergy basis.

In the deeply bound regime a further trick tremendously accelerates the computation using Bloch state. Instead of calculating the wave function overlap via a direct, properly truncated integration we exploit their coefficient vector representation (see 2.2.4). As mentioned above, this coefficients are defined with respect to the basis given by the set of plane waves $\exp(i\,m g_0 x)$. The coefficient vectors of both lattices are thus defined with respect to a common basis. For the calculation of the Franck-Condon factors it is thus sufficient to compute the scalar products between the corresponding coefficient vectors. Furthermore, as the microwave radiation leaves the atomic momentum unchanged transitions occur only between states with the same wave vector κ. The computation of Franck-Condon factors among Bloch states with different κ's can thus also be omitted. A small extension of the scalar product method allows for its usage even in the case when the atom couples to both next neighbors. In this case, the Bloch states with κ=0 and $\kappa = g_0/2$ do have a negligible difference between their spatial probability distribution. But, their phase factor differs by $\exp(i\,\pi) = -1$ every second lattice site. The sum of these two Bloch states thus yields a state which occupies only every second lattice site. The overlap between such superposition states thus corresponds to the Franck-Condon factor of two isolated lattice sites as long the applied lattice displacement is not larger than its periodicity.

2.2.2 Microwave transitions in a multi-level system

For the quantitative theoretical analysis of the experimentally observed microwave-induced dynamics, e.g. the high order sideband spectrum in fiure 2.10, the Schrödinger equation of a two level system (1.1.2) is a good starting point. In this approximation each pair of states $|44, n\rangle$ and $|33, n'\rangle$ is regarded as an isolated two level subsystem. Using Bloch states defined in the foregoing section, both the strength and the resonance frequency of the corresponding transition can be calculated thus providing the required information for the time evolution of the spin. Nevertheless, this simplified model becomes inaccurate when a strong microwave field is used. The experimental parameter range allows for a maximum bare Rabi frequency of $\Omega_{\text{bare}} = 2\pi\,59$ kHz. This needs to be related to the frequency spacing between two neighboring sidebands which amounts to 115 kHz in our case. As both values are of the same order of magnitude off-resonant excitation is significant and must be considered for the quantitative microwave dynamics as it influences the observed resonance positions as well as the observed Rabi frequencies.

Schrödinger equation for the spinor For the more appropriate description of the experimental situation the theoretical frame of a two level atom can be extended by inserting the spatial Hamiltonian of each lattice (equation 2.2.1) into the spin evolution equation 1.1.2. The resulting Schrödinger equation thus fully accounts for the one-dimensional motion of the atom along the lattice axis while its spin is coupled to the microwave field

$$\begin{pmatrix} \frac{\hat{p}}{2m} + U_{44}(\hat{x}) & \hbar\Omega_{\text{bare}}/2 \\ \hbar\Omega_{\text{bare}}/2 & \frac{\hat{p}}{2m} + U_{33}(\hat{x}) + \omega_{\text{mw}} \end{pmatrix} \begin{pmatrix} \psi_{44}(x,t) \\ \psi_{33}(x,t) \end{pmatrix} = i\hbar \frac{d}{dt} \begin{pmatrix} \psi_{44}(x,t) \\ \psi_{33}(x,t) \end{pmatrix}. \tag{2.2.5}$$

Here, $\hat{x}$ and $\hat{p}$ denote the position and the momentum operators of the atom, $U_{44}(\hat{x})$ and $U_{33}(\hat{x})$ are the two different lattice potentials and $\psi_{44}(x,t)$ and $\psi_{33}(x,t)$ are the wave functions of each spin component, respectively. The frequency of the microwave radiation is labeled by ω_{mw}. At this point the radial degree of freedom is ignored as due to its relatively weak confinement the classical radial motion can be treated independently (see section 2.4).

It is very instructive to write the Hamilton operator in this form as it shows that the total equation of motion is mathematically a system of two coupled partial differential equations. Solving this problem by using numerical methods yields the full information about the spatial and the spin degree of freedom. In principle, this can be done for any initial spatial distribution of the two spin components which can be experimentally prepared regardless of whether it can be nicely expanded in terms of the energy eigenbasis or not. Especially if the microwave radiation starts to couple both next neighbor lattice sites or if the microwave brings the atom in resonance with one of the broad energy bands where tunneling plays a role the direct approach provides the full information about the microwave-induced spread of the spatial probability distribution over the lattice. The drawback of the direct numerical solution of the Schrödinger equation is its computational demand. Moreover, it does not provide an intuitive picture for the appearance of sidebands.

Especially because of the second point it is equally attractive to express equation 2.2.5 with respect to the energy eigenbasis which is given by the product states between the spin degree of freedom and the motional eigenstates

$$\begin{pmatrix} E_{44,n\kappa} & \frac{1}{2}\hbar\,\Omega_{44,\text{n}\kappa\leftrightarrow 33,\text{n}'\kappa'} \\ \frac{1}{2}\hbar\,\Omega_{33,\text{n}'\kappa'\leftrightarrow 44,\text{n}\kappa} & E_{33,n'\kappa'} + \hbar\,\omega_{\text{mw}} \end{pmatrix} \begin{pmatrix} c_{44,n\kappa} \\ c_{33,n'\kappa'} \end{pmatrix} = i\hbar \frac{d}{dt} \begin{pmatrix} c_{44,n\kappa} \\ c_{33,n'\kappa'} \end{pmatrix}. \tag{2.2.6}$$

Here $E_{44,n\kappa}$ and $E_{33,n'\kappa'}$ label diagonal matrices whose entries are the bare eigenenergies of the vibrational states resulting from the band structure model introduced in the forgoing section. Similarly, the coefficient vectors $(c_{44,n\kappa}, c_{33,n'\kappa'})$ result from the

projection of the full spinor onto the Bloch states basis of each lattice. Note that the parameter ω_{mw} shifts the energy of the entire subspace of the $|33\rangle$-hyperfine state. It thus controls which sideband is tuned in resonance with the microwave field. The coupling between the hyperfine states is now also described by a square matrix labeled by $\Omega_{44,\mathrm{n}\kappa\leftrightarrow 33,\mathrm{n}'\kappa\prime} = (\Omega_{33,\mathrm{n}'\kappa\prime\leftrightarrow 44,\mathrm{n}\kappa})^{\dagger}$ which in general exhibits nonzero entries at any position. Each entry is given by the wave function overlap between the corresponding motional states multiplied by the bare Rabi frequency Ω_{bare}. The absolute value of each entry thus corresponds to the Rabi frequency of the respective transition. In general, the entries are not real numbers. The phase relation between the entries start to play a role when a strong microwave field leads to strong off-resonant excitation where interference between several sideband transition must be taken into account.

For this work, the Bloch states are used for the calculation of the Franck-Condon factors. As the microwave radiation is not capable of changing the momentum of the atom only the entries coupling Bloch states with the same κ are nonzero. Note that the Bloch states can be calculated for any lattice shift, or in general, for any other variation of the trapping potential. Thus, the Hamilton operator in equation 2.2.6 is easily constructed for any experimental situation.

According to the discussions in the foregoing section the above equation can be significantly simplified when the motional dynamics are limited to a pair of wells so that the Bloch vector κ can be discarded by setting it equal to zero. For most of the microwave transitions experimentally investigated in this work the reduced set of vibrational states is entirely sufficient. The size of the four square matrices forming the Hamilton operator is then given by the number of the considered bands n_{max}. This number is chosen suitably for the problem under investigation as it strongly affects the required calculation time.

Mathematically, the reduced Schrödinger equation 2.2.6 is a system of $2 \times n_{\mathrm{max}}$ coupled differential equations which again can be solved numerically. This approach is particularly interesting when the amplitude of the microwave pulse and thus the bare Rabi frequency Ω_{bare} is time dependent as is the case for a Gaussian pulse. But, especially when many bound states must be taken into account, the computational effort of this approach is very high.

Dressed states basis The computational time can be significantly reduced in case the bare Rabi frequency is constant during the pulse duration. In this case the Hamilton operator in equation 2.2.6 does not explicitly depend on time so that the Schrödinger equation can be solved by reformulating it in terms of an eigenvalue equation and by diagonalizing the Hamilton operator. The new eigenstates form the so-called dressed state basis very familiar from the two level atom [54]. The solution of the initial state problem is now trivial: Once it has been expressed in

the dressed state basis a simple multiplication with the phase factors $\exp(i\,E_{\mathrm{dr},i}/\hbar\,t)$ yields the entire time evolution where $E_{\mathrm{dr},i}$ labels the energy of the i^{th} dressed state. In contrast to the approach with a direct solution of the differential equation system the calculation can be easily performed for arbitrary long evolution times.

The dressing picture can even be used for approximating the time evolution induced by a Gaussian microwave pulse (or by pulses with other time dependent shapes). For this, the pulse is divided into discrete time steps which are short enough for the field amplitude to be considered as constant. The form of the pulse is thus approximated by a step function. The time evolution of each time step can be calculated within the dressed state model where the final state of the previous step is used as the input state in the following step. In practice, this approach is very convenient as it turns out to be fast compared to the direct solution of the system of differential equations.

Three level example It is instructive to investigate a simple example in order to illustrate the effects introduced by the multilevel system. The simplest one is that of a three level system (see figure 2.8 (a)). Let the microwave be able to couple the states $|2\rangle$ and $|3\rangle$ with the common state $|1\rangle$. The time evolution of the system then depends on the coupling strengths of the two transitions with respect to the energy separation Δ_{23} between the states $|2\rangle$ and $|3\rangle$. When one or both coupling strengths become comparable to this energy gap, the two transitions start to influence each other. For illustration figure 2.8 (b) shows the dependence of the dressed eigenenergies on the microwave frequency. In case of a negligible coupling ($\{\Omega_{12},\ \Omega_{13}\} \ll \Delta_{23}$) the bare energies E_2 and E_3 of the states $|2\rangle$ and $|3\rangle$ are constant while the sum $E_1 + \hbar\,\omega_{\mathrm{mw}}$ linearly increases with ω_{mw}. In this limit the resonance positions are located at microwave frequencies fulfilling the condition $\hbar\,\omega_{\mathrm{mw}} = E_{2/3} - E_1$ which corresponds to the crossing points in figure 2.8 (b).

When the coupling is switched on the crossings turn into anti crossings. For the presented example the Rabi frequency Ω_{12} is held constant at $0.1 \times \Delta_{23}$ while four different values are used for $\Omega_{13} = \{0, 0.3, 0.5, 1\} \times \Delta_{23}$. In the dressed state picture the resonance of a transition is located at the frequency which shows the smallest gap between the eigenenergies. Obviously, the resonance frequency of the $|1\rangle \leftrightarrow |2\rangle$ transition is shifted according to the strength of the $|1\rangle \leftrightarrow |3\rangle$ transition. This is exactly the phenomenon called AC Stark shift [54]. From this point of view, when the microwave radiation is resonant with the $|1\rangle \leftrightarrow |2\rangle$ transition it is far red detuned with respect to the $|1\rangle \leftrightarrow |3\rangle$ transition. Due to the coupling Ω_{13} the energies of the states $|1\rangle$ and $|3\rangle$ are pushed apart. The shift of the state $|1\rangle$ can eventually be probed by the $|1\rangle \leftrightarrow |2\rangle$ transition.

A closer look onto the gap between the eigenenergies E_2 and E_1 is shown in figure 2.8 (c). In the dressed state picture the gap corresponds to $\hbar$ times the Rabi

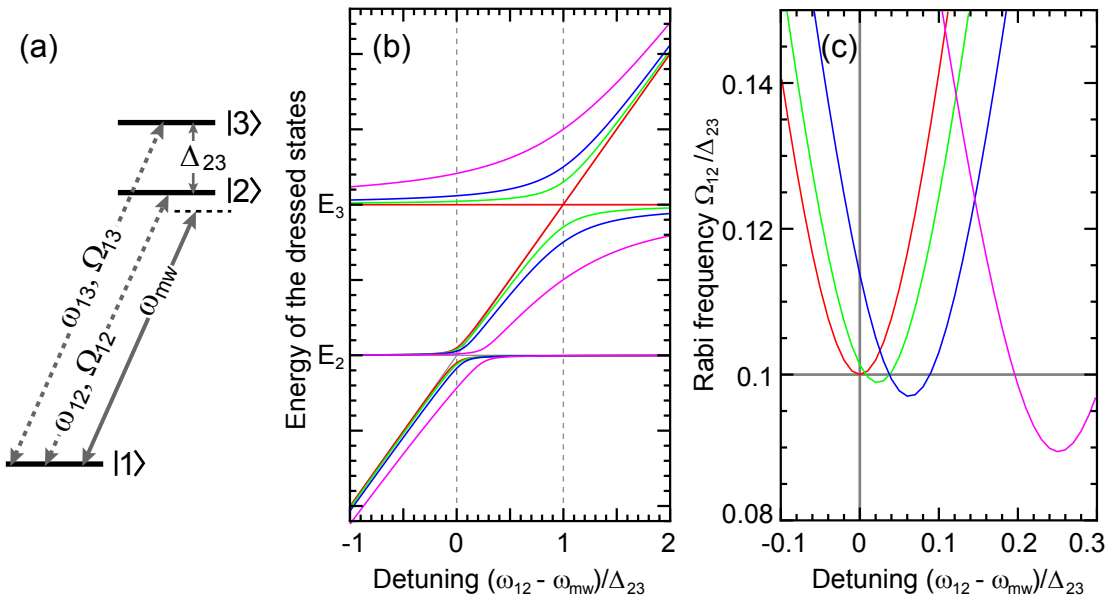

Fig. 2.8: Three level system. (a) The transition $|1\rangle \leftrightarrow |2\rangle$ ($|1\rangle \leftrightarrow |3\rangle$) has the resonance frequency ω_{12} (ω_{13}) and the coupling strength Ω_{12} (Ω_{13}). The frequency of the microwave is labeled by ω_{mw}. (b) The eigenenergies of the three dressed states for four different values of Ω_{13} while Ω_{12} remains constant. (c) The Rabi frequency of the $|1\rangle \leftrightarrow |2\rangle$-transition depending on the detuning $(\omega_{12} - \omega_{\mathrm{mw}})$. Its resonance position is shifted when the coupling strength Ω_{13} of the other transition increases. Additionally, a larger value of Ω_{13} slightly reduces the minimum value of Ω_{12}.

frequency of the transition. Again, the shift of the gap minimum clearly indicates the shift of the resonance position. In addition, the figure shows that the gap minimum becomes smaller when the strength of the neighboring transition is increased. This corresponds to a smaller Rabi frequency even in case the microwave is tuned to the new, shifted resonance position. The change of the Rabi frequency due to microwave dressing must in particular be considered for the measurement of the Franck-Condon factors (see section 2.5).

The full multilevel structure By considering the full quantum mechanical multilevel structure we are able to simulate experimentally relevant deviations from the simple two level approximation. A good experimental example for the microwave-induced AC stark shift is the movement of the first order sideband transition according to the variation of the microwave power. When the lattice displacement is very small the Franck-Condon factors for all of the carrier transitions are still close to unity and at the same time the factors for the sidebands are very small. When the

microwave is tuned in resonance with the first red sideband as in figure 2.9 (a) the radiation is at the same time red detuned with respect to the strong carrier transitions. Due to the AC stark shift caused by the carriers the hyperfine states $|44\rangle$ and $|33\rangle$ together with all of their motional states are pushed apart. When the dressed energy level scheme is probed by the weak sideband transition its resonance peak appears blue shifted with respect to the unperturbed situation. The measurement in figure 2.9 (b) shows the peak positions of the first red sideband for three different microwave powers. All three peaks have been generated using a Gaussian pulse with a $e^{-1/2}$-width of 15 μs. This explains the different heights of the peaks as the pulse area is not kept constant. The calculation using the full multilevel structure very well reproduces both, shift and height of the peaks. In the same manner the first order sideband spectrum from figure 2.3 (c) can be simulated which then reveals that the observed sidebands are also shifted from the ideal position. This explains the discrepancy to the measurement of the oscillation frequencies in figure 2.4.

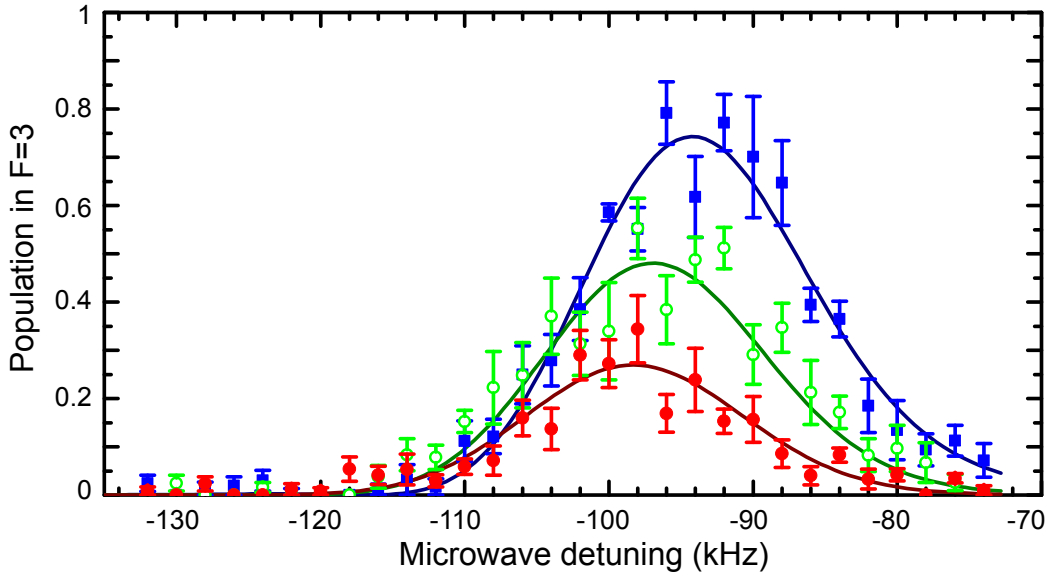

Fig. 2.9: Microwave-induced AC Stark shift. For a very small shift (ϑ=3.9°) the first red sideband is "attracted" towards the carrier transition when the microwave power is increased. The theoretical curves result from the dressed state calculation accounting for off-resonant coupling between the vibrational states.

One further interesting question is: Which set of experimental parameters leads to a well resolved sideband spectrum? In other words, how large is the off-resonant transfer of population to neighboring motional states? This, e.g., depends on the choice of the pulse shape as the simple rectangular pulse leads to a much stronger off-resonant population mixing than a Gaussian pulse. The scheme for the state-

selective detection explained on page 8 dose not discriminate between vibrational states. A direct measurement of the population of a vibrational state thus requires more elaborated techniques (see section 4). In contrast, during the simulation all of the populations are directly available. The simulation thus helps in advance to predict the amount of population redistribution after the application of a microwave pulse. For the case shown in figure 2.9, where a Gaussian pulse has been used, the calculation predicts a negligible transfer to states other than $|33, 1\rangle$. This becomes different for a rectangular pulse with the same pulse areas for which a few percent of the atoms are transferred to the $|33, 0\rangle$ state (see also figure 2.23).

The theoretical background summarized in this section provides a basis for the quantitative analysis of the measurements presented next.

2.3 High order sideband transitions

According to the calculated Franck-Condon factors in figure 2.6 (b) it should be possible to reach all available vibrational states of the trapping potential starting from the ground state with a single microwave pulse. The measured wide range spectrum shown in figure 2.10 indeed exhibits up to fourteen peaks each corresponding to a $|44, 0\rangle \leftrightarrow |33, n\rangle$ transition. The entire scan is divided into four parts. The first part shows only the carrier transition without displacement and is used to mark the position of zero detuning. The other three sub-spectra, each with a different polarization angle ϑ, favor a different set of sideband transitions namely those for which the Franck-Condon factors become substantial.

In addition to the mostly well separated resonance peaks a cutoff at the detuning of -1.4 MHz marks the position of the highest bound states. From the vibrational eigenenergies resulting from the band structure model (section 2.2.1) the peak positions of the sideband transitions can be immediately calculated. The expected positions of the $|44, 0\rangle \leftrightarrow |33, n\rangle$ transitions are indicated by pale vertical lines in the background of figure 2.10. Generally, experimental and theoretical peak positions quantitatively agree although there are small but significant discrepancies. A closer look on the extracted peak separations is given in figure 2.11. Here the decreasing spacing between adjacent peaks in the experimental data follows the theoretical expectation (apart from an offset).

The model for the lattice potential taking into account experimental imperfections (see page 21) is used again. Note that a better agreement between experiment and theory can be achieved for each individual sub-spectrum. The only free parameter is the rotation angle of the half wave plate $\mathrm{wp2_r}$: -0.5° for the low order spectrum (○), which coincides with the angle necessary to explain the spectrum shift in figure 2.5. For the two higher order spectra, though, an almost perfect alignment

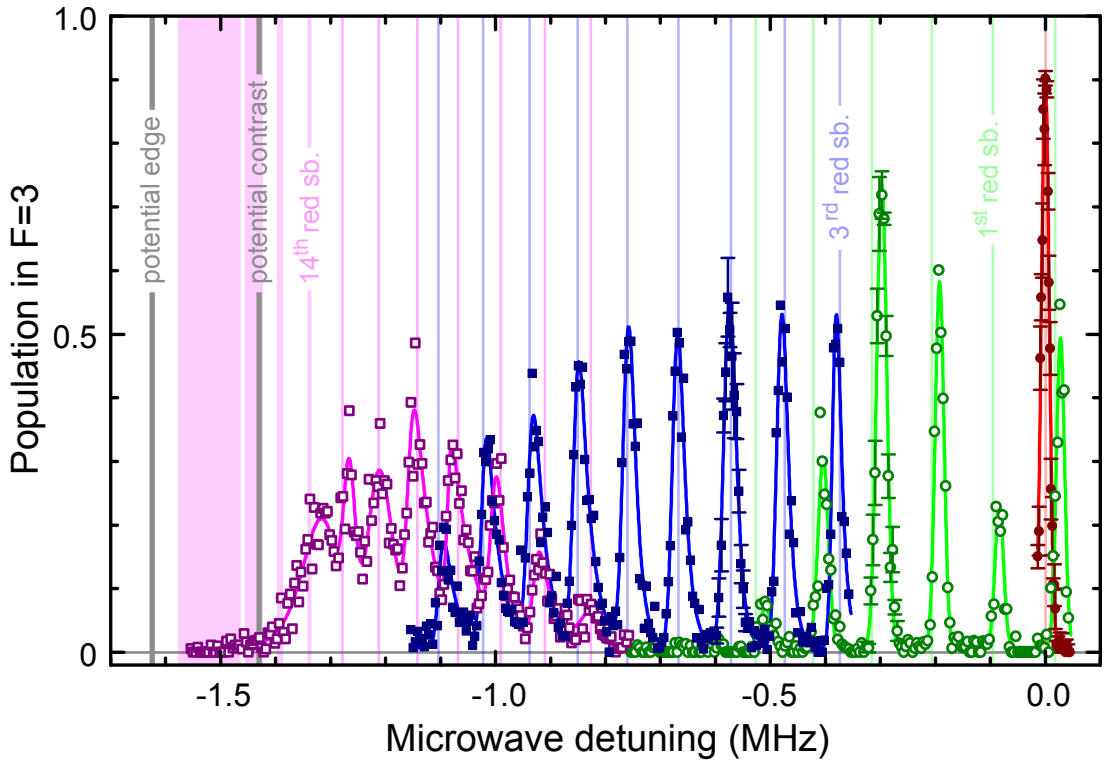

Fig. 2.10: Starting with an axially ground state cooled sample a wide frequency scan exhibits several resonances each corresponding to a n^{th}-order sideband. The set of visible sidebands depends on the polarization angle of ϑ={0° (●), 20.1° (○), 50.3° (■), 75.5° (□)} (Δx={0, 43, 111, 176} nm). The experimental resonances are fitted with an asymmetric peak function (equation 2.3.1). The pale vertical lines indicate the positions of the sideband transitions resulting from the band structure model. The two gray vertical lines indicate the expected positions of the free space edge and of the edge of axial confinement of the $|33\rangle$-potential, respectively. They are calculated for the polarization angle of $\vartheta = 75.5°$.

of the half wave plate provides better agreement; similar to the measurement of the oscillation frequencies (see figure 2.4). A more accurate experimental investigation of the observed discrepancies is thus required for a more complete picture.

Note that the large detuning used in this scan is of the same order of magnitude as the Zeeman splitting between the magnetic sub-levels. At approximately -1 MHz the microwave field becomes resonant with the π-transition $|33\rangle \leftrightarrow |43\rangle$ so that three different hyperfine states are coupled via the same microwave field (see figure 1.4). By recording a microwave spectrum without displacement we experimentally verified

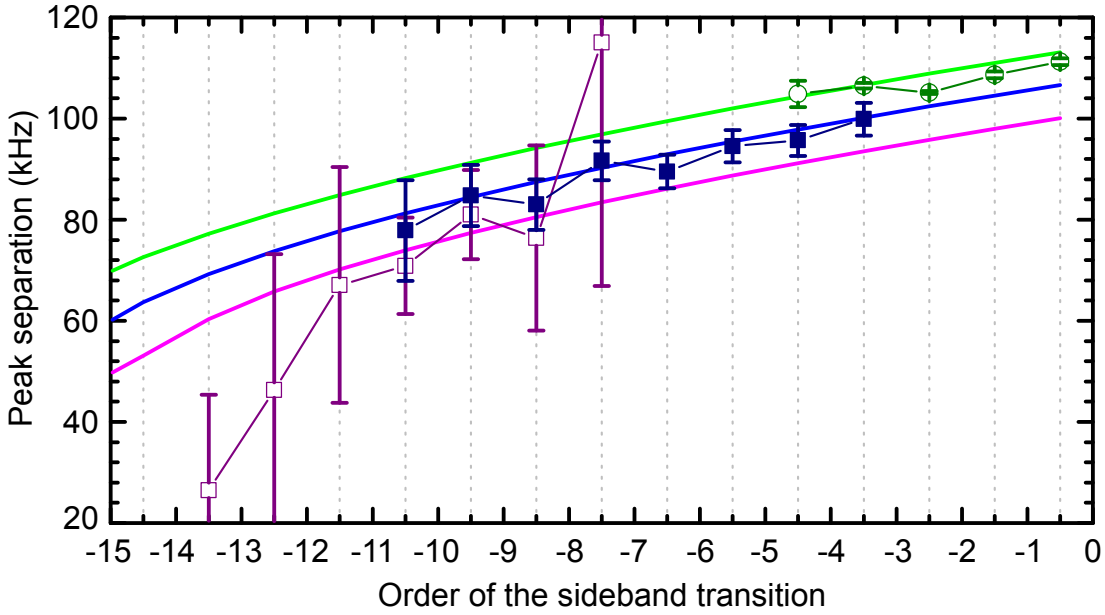

Fig. 2.11: Separation of adjacent sideband peaks depending on the order of the sideband (same symbols as in figure 2.10). The data points are placed in between the two relevant sidebands. In case of highest sidebands the theoretical curves result from an average over the Bloch vector κ so that the width of the bands dose not play a role for the peak separation.

that the π-transition is not detectable using the same parameters as for the spectra in figure 2.10. This is, first, because of the smaller magnetic dipole matrix element and second, because the microwave field seems to be very well circularly polarized at the position of the atoms. The π-transition thus does not interfere with the presented high order sideband spectrum.

A closer look to the peak form of the sideband transitions uncovers their asymmetry. This is a signature of broadening as will be discussed in section 2.4. Broadening effects, e.g., alter the heights of the measured sideband transitions so that they cannot be directly compared to the calculated Frank-Condon factors in figure 2.6. For further analysis the spectra are fitted using a peak function which results from a convolution of an asymmetric detuning distribution and a Gaussian peak

$$\begin{aligned} \mathrm{p}(\nu) \;=\; & \frac{A_0}{2|\gamma_\mathrm{b}|}\,\exp\left(\frac{\sigma_\nu^2}{2\,\gamma_\mathrm{b}^2}-\frac{\nu-\nu_\mathrm{cm}+\gamma_\mathrm{b}}{\gamma_\mathrm{b}}\right)\times \\ & \mathrm{erf}\left(\frac{\sigma_\nu}{\sqrt{2}\,\gamma_\mathrm{b}}-\mathrm{sign}(\gamma_\mathrm{b})\,\frac{\nu-\nu_\mathrm{cm}+\gamma_\mathrm{b}}{\sqrt{2}\,\sigma_\nu}-\right). \end{aligned} \tag{2.3.1}$$

Here ν denotes the microwave frequency, A_0 is the amplitude of the Gaussian, σ_ν is its $e^{-1/2}$-width and $\mathrm{erf}(x)$ denotes the error function. ν_{cm} denotes the the center-of-mass position of the peak. For reasons explained in section 2.4 the asymmetric detuning distribution used is given by a truncated exponential function with the characteristic asymmetric width γ_b (see equation 2.4.1). The ideal resonance position in the limit of a vanishing peak asymmetry is defined by $\nu_{\mathrm{ideal}} = \nu_{\mathrm{cm}} - \gamma_\mathrm{b}$. Note that for the correct comparison to the theory which does not consider broadening the peak separations presented in figure 2.11 are calculated using ν_{ideal}.

Function 2.3.1 is only fitted to peaks for which the asymmetry is clearly visible. Thus, only the middle (■) and high (□) order spectra are fitted using the asymmetric peak function whereas a simple Gaussian is used for the carrier (●) and the low order spectrum (○). The reason for this restriction is, that the exp-factor and the erf-factor diverge towards very large and very small values when the asymmetry parameter γ_b becomes small. Although their product analytically is always well defined the numerical treatment during the fit stops or returns extremely large error bars when γ_b is smaller than ∼5 kHz. All deduced peak widths are plotted in figure 2.12.

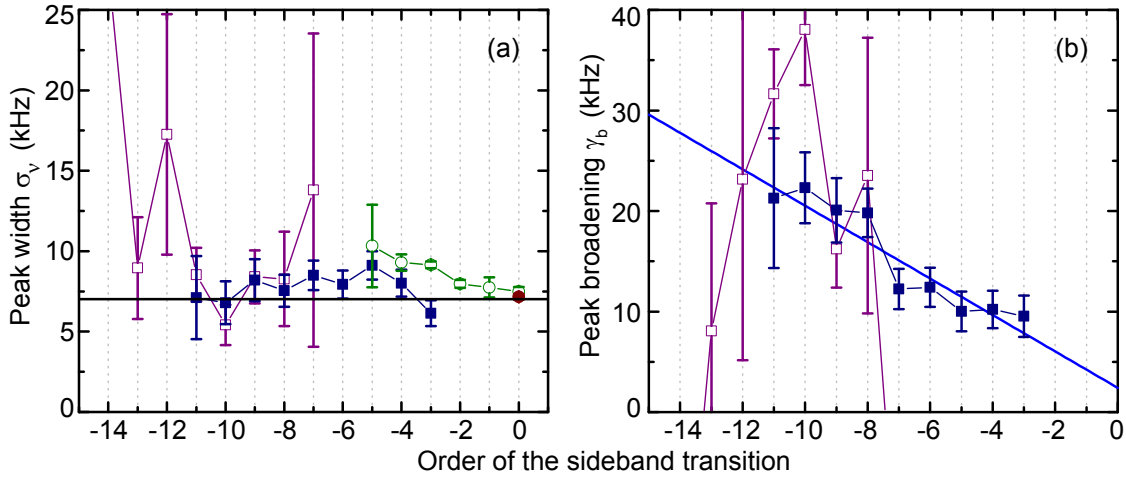

Fig. 2.12: The fitted peak widths of the resonances in figure 2.10 have two contributions (same assignment of the symbols): (a) the Gaussian width σ_ν and (b) the asymmetric width γ_b (see equation 2.3.1). The horizontal line in (a) indicates the Fourier-limited width of a π-pulse. In (b) a linear fit outlines the increase of peak asymmetry γ_b with the order of the sideband.

Because of their well separated peaks reliable conclusions are only drawn from the carrier, the low and the middle order sideband spectra. The fitted Gaussian widths σ_ν turn out to be slightly broader than the Fourier limit of a Gaussian π-pulse and basically independent of the order of the sideband transition (note that the width of a Gaussian pulse also depends on its pulse area). Although the widths in the low

order spectrum exhibit an unambiguous increase, most probably this broadening still stems from thermal contributions even though the peaks could not be reliably fitted with the asymmetric function (compare to figure 3.6). This is supported by the fact that even the widths of the middle order transitions are almost Fourier-limited. Their broadening seems to be completely governed by the asymmetric contribution which approximately linearly increases with the order of the sideband (see figure 2.12(b)). In section 2.4 this broadening and its linear increase will mostly be attributed to the thermal radial motion of the atoms.

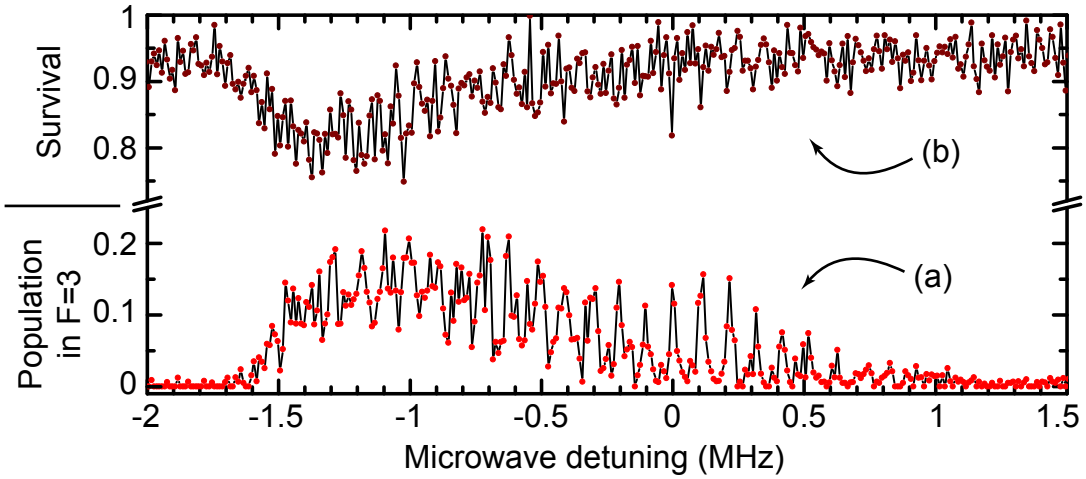

Fig. 2.13: (a) A high order spectrum similar to that in figure 2.10 (no ground state cooling). (b) The survival probability for the same experimental sequence as in (a) (no state-selective push-out applied). When microwave detuning approaches the edge of the potential atoms get lost.

Apart from broadening, atoms can even get lost when the microwave pulse excites them close to the edge of the potential as is demonstrated in figure 2.13. This phenomenon is expected when thinking about the broad Bloch bands (figure 2.6 (a)) just below the energetic trapping boarder where tunneling between the potential wells plays a considerable role. Due to the axially not ground state cooled sample the frequency region where losses occur in figure 2.13 is very broad.

In the following I give an overview of the most important broadening and decoherence mechanisms in our setup. The focus is placed on their characteristic shape and their dependence on the order of the sideband.

2.4 Broadening and decoherence sources

At the beginning, it is instructive to collect possible effects which might be responsible for the observed distortions of the spectra and the Rabi oscillations which will be discussed later on. It turns out, that the main distortion stems from the fact that the atomic ensemble under investigation exhibits a thermal distribution of its motional degrees of freedom. The axial and the radial degree of freedom are qualitatively different in the sense, that the first must be treated quantum mechanically while the second one can be considered classically. Second, as the trapping potential is designed to be spin dependent the microwave resonances are sensitive to fluctuations of the potential (see figure 1.9) [57]. Thus, other broadening mechanisms are caused by technical imperfections, namely, by the jittering of the lattice beam power and of the lattice displacement, by the beam pointing stability and by the polarization inhomogeneity across the lattice beam. Note that not only the resonance frequency of a given sideband transition is subject to fluctuations but also the corresponding Franck-Condon factor. As usually, for transitions between magnetically sensitive atomic states a noisy quantization field also plays a role.

In order to present a suitable overview of the different noise contributions their strengths are graphically tabulated in figures 2.18 and 2.19. The controlled shift of the lattices relative to each other is a key feature of our experiment. We thus investigate each disturbance at various polarization angles ϑ and take standard values for all other experimental parameters.

Concerning the form of the detuning distribution the noise sources can be classified into two categories. The first one comprises effects which symmetrically smear out the resonance lines. In this case, a small deviation of an experimental parameter from its nominal set-value leads to a linear change of the detuning with respect to the center frequency. When the parameter fluctuation does have a Gaussian distribution so does the corresponding detuning distribution. Effects from this category can thus be characterized by the Gaussian width σ_b. The convolution of this distribution with the Fourier-limited peak (with the width σ_f) yields again a Gaussian peak whose width is defined by the quadratic sum $\sigma_\nu^2 = \sigma_\mathrm{f}^2 + \sigma_\mathrm{b}^2$.

Members of the second category lead to an asymmetric detuning distribution which has the form of a truncated exponential function

$$\eta(\delta) = \Theta(\mathrm{sign}(\gamma_\mathrm{b})\,\delta)\frac{1}{|\gamma_\mathrm{b}|}\exp(-\frac{\delta}{\gamma_\mathrm{b}}). \tag{2.4.1}$$

Here, δ denotes the microwave detuning from the ideal resonance position, $\Theta(x)$ denotes the heaviside function and $\mathrm{sign}(x)$ returns the sign of x. The parameter γ_b is a measure for the asymmetric broadening (see page 61). Note that its sign

determines whether the "tail" of the distribution points towards positive or negative detunings. The convolution of this distribution with a gaussian pulse yields the peak function defined in equation 2.3.1.

It is impossible and unnecessary to discuss each of the individual sideband transitions $|44, n\rangle \leftrightarrow |33, n'\rangle$. For a representative overview, the influence onto few selected transitions is shown: the carrier transitions $|44, n\rangle \leftrightarrow |33, n\rangle$ with n={0, 3, 6, 9, 12}, and the sideband transitions starting from the ground state $|44, 0\rangle \leftrightarrow |33, n\rangle$ with n={0 ,3 ,6 ,9 ,12}. These are the most extreme transitions in the sense that fluctuations for all other transitions have a magnitude which is in between the presented ones. The restriction to states below n=12 is chosen due to the experimentally negligible width of their Bloch bands. For most of the presented settings the calculations based on the Bloch states thus yields sharply defined results. In case the microwave couples the wave function of each lattice site to both next neighbor sites the Franck-Condon factor reflects the overlap with only one individual neighboring site as discussed on page 41.

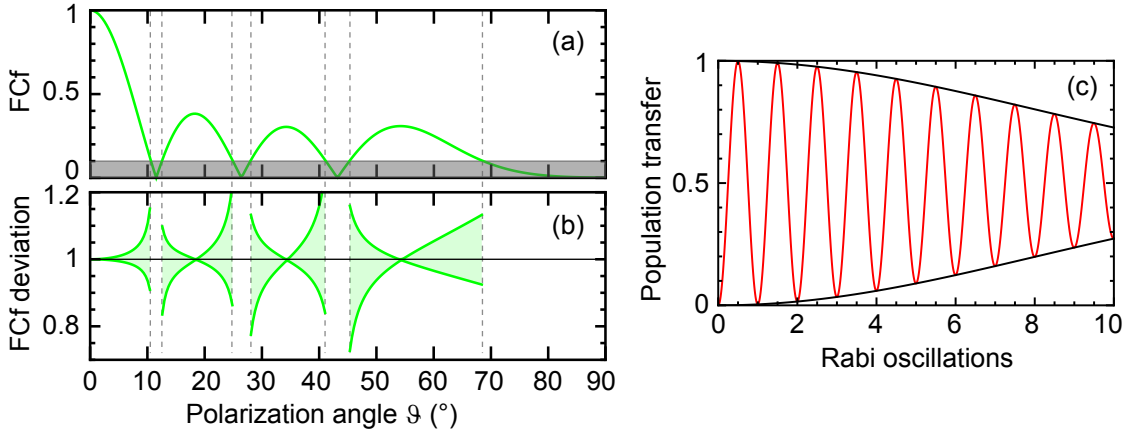

Fig. 2.14: (a) The Franck-Condon factor of the transition $|44, 3\rangle \leftrightarrow |33, 3\rangle$ and (b) the corresponding confidence interval due to thermal radial motion showing its typical dependence on the polarization angle. The fluctuation of the Franck-Condon factor is provided in terms of a ratio. The original Franck-Condon factor at the given polarization angle corresponding to a value of 1 in this representation. (c) Illustration of the perfectly resonant Rabi oscillation which suffers from a Gaussian distribution of the Rabi frequency ($\sigma_{\Omega_R} = 0.02\,\Omega_{mean}$, see equation 2.4.2).

As the relation between the displacement and the Franck-Condon factors is complicated and in general shows up several sharp kinks (see figure 2.14 (a)) at certain experimental parameters even small fluctuations may strongly affect the wave function overlap. For simplicity, we restrict the analysis to regions where the Franck-

Condon factor is larger than 0.1. Although the choice of this threshold is arbitrary it is motivated by the fact that the Franck-Condon factor of 0.1 corresponds to a Rabi oscillation with a frequency of ∼6 kHz. At the present stage of the experiment, due to decoherence, transitions with smaller coupling strengths experimentally hardly show more than one full oscillation before the signal is completely damped. They are thus not useful for further applications. Within the 'good' regions the local dependence of the Franck-Condon factor on the displacement is always smooth. The fluctuation of the Franck-Condon factor due to a small variation of some experimental parameter is, however, not necessarily linear. There is thus no simple transformation available between the noise distribution of the parameter under investigation and the resulting noise distribution of the Franck-Condon factor. For simplicity, the confidence interval for the distribution of the Franck-Condon factor is defined by determining the minimum and the maximum Franck-Condon factor within the confidence interval of the noise source. These boundaries are then displayed as a ratio with respect to the ideal Franck-Condon factor (see figure 2.14 (b)). For comparison, presuming a Gaussian distribution of the Franck-Condon factor the expected distortion of the resonant Rabi oscillation can be calculated analytically

$$\begin{aligned} & \int_{-\infty}^{\infty} \frac{1}{\sqrt{2\pi}} \sigma_{\Omega_\mathrm{R}} \exp\left(-\frac{(\Omega_\mathrm{R}-\Omega_\mathrm{mean})^2}{2\,\sigma_{\Omega_\mathrm{R}}}\right) \frac{1}{2}(1-\cos(\Omega_\mathrm{R}\,t))\,d\Omega_\mathrm{R} \\ = \; & \frac{1}{2}(1-\exp(-\frac{1}{2}\sigma_{\Omega_\mathrm{R}}^2 t^2)\cos(\Omega_\mathrm{mean}\,t)). \end{aligned} \tag{2.4.2}$$

Here, Ω_mean labels the mean Rabi frequency and $\sigma_{\Omega_\mathrm{R}}$ denotes the width of the Rabi frequency distribution. It follows that the contrast of the Rabi oscillation has a Gaussian form. The reduction of the contrast is exemplarily illustrated in figure 2.14 (c).

In the following the contribution of each broadening mechanism is discussed separately. For these investigations a perfect experimental setup with ideal optical elements is assumed. For small deviations from the ideal case, as e.g. observed in the experiment, the drawn conclusions are quantitatively similar.

Axial motion

Before the investigation of broadening mechanism for pure microwave transitions $|44,n\rangle \leftrightarrow |33,n'\rangle$ we briefly address the case of a statistical mixture over the axial vibrational states. As, in general, all pure sideband transitions possess a different resonance frequency and a different Rabi frequency the observed spin evolution suffers from broadening and decoherence (see e.g. the spectrum in figure 2.3). On the other hand, due to the discretized motional spectrum the spin evolution can be

exploited for the measurement of the vibrational state populations (see section 4.1).

Here, we concentrate on the special case of unshifted potentials where, presuming $U_{44} = U_{33}$ perfectly holds, all carrier transitions are identical. After each everyday alignment (see page 17) a simple spectrum is recorded in this configuration in order to make a final check of the alignment quality using atoms as a probe. Moreover, the case of microwave pulses with unshifted potentials is important for our realization of the quantum walk [8]. Due to different light shifts for the states $|44\rangle$ and $|33\rangle$ they experience slightly different trap depths even in the case of perfectly linearly polarized trapping lasers. This difference may easily be overwhelmed by a small polarization ellipticity. Figure 2.15 illustrates the differences between the carrier transitions if the depths of the sinusoidal potentials are not the same.

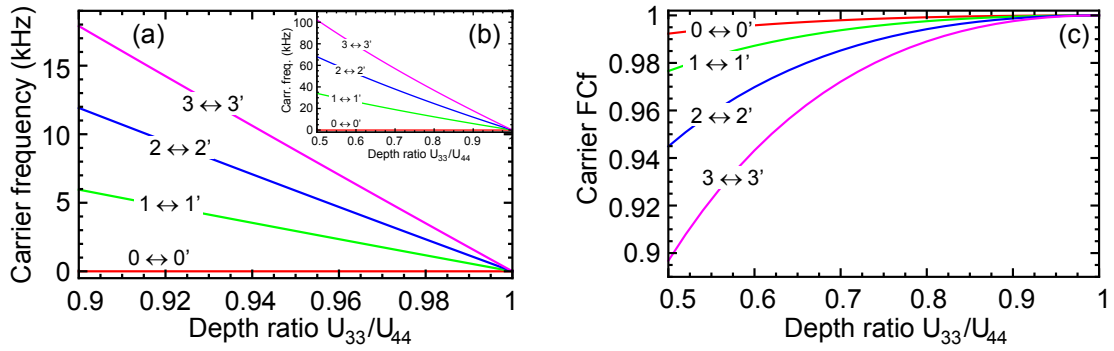

Fig. 2.15: Differences between carrier transitions in case of unshifted potentials: Panels (a) and (b) show the resonance frequencies with respect to the $0 \leftrightarrow 0'$ transition and (c) the Franck-Condon factors depending on the ratio between the depths of the potentials U_{33}/U_{44}. For perfectly linearly polarized lattice beams this ratio amounts to 0.9975 but it can be strongly affected by a residual polarization ellipticity (compare to figure 1.9). While the variation of the Franck-Condon factors is negligible for usual experimental settings the resonance frequencies are strongly affected.

During the experimental sequence the population of the vibrational states is not static but rather can be changed by heating mechanisms or by deliberate lattice shifts and depth ramps. Fortunately, the intrinsic heating caused by technical noise is on the order of one vibrational quantum per 100 ms and can be neglected for single pulses or even long pulse trains and long Rabi oscillations. In contrast, the atomic ensemble suffers from significant decoherence of its quantum mechanical state if diabatic lattice manipulations induce a change of the atomic motional state [23].

Lattice depth

Although the jitter of the depth of the lattice potential is not the dominating distortion in our setup this noise source is discussed first. This is done with regard to other noise sources as many of them are traced back to a variation of the lattice depth.

Due to active stabilization the standard deviation for the laser power fluctuation in our setup amounts to ±1%. In principle, the frequency distribution of the noise must be considered for a complete discussion. In our case, the significant frequency range is ≈0.1 Hz-150 kHz. Here, noise contributions at frequencies much larger than the energetic spacing between motional states can be ignored because they average out to an effective mean trapping potential. The lower bound of the relevant frequency range is defined by the time which is required for several sequence repetitions with the same initial conditions.

The influence of a fluctuating trap depth is investigated by recalculating the eigenenergy spectrum and the corresponding eigenstates for different depths (see equation 2.2.4). The spread of the eigenenergies directly transforms into a detuning distribution of a microwave transition $|44, n\rangle \leftrightarrow |33, n'\rangle$. Because of the linear dependence a Gaussian noise distribution of the laser power thereby leads to a Gaussian detuning distribution characterized by the width σ_b. Panels (b) and (f) in Figure 2.18 show its expected value. As long as the depths of the two potentials are identical the eigenenergies fluctuate perfectly in common so that at least the carrier transitions are not affected. This, in general, does not hold for sideband transitions. The broadening becomes more serious when the lattice displacement is nonzero where due to wobbling of U_{33} the difference between U_{44} and U_{33} is very large. The transition $|44, 0\rangle \leftrightarrow |33, 0\rangle$ is the most sensitive of all carrier transitions as it fluctuates with the full amplitude whereas the fluctuation of the higher states is increasingly weaker. Accordingly, the relative fluctuation between the ground state and the higher vibrational states increases with the order of the sideband.

The influence of the depth fluctuation on the Franck-Condon factor is shown in panels (b) and (f) of figure 2.19. The variation of the Franck-Condon factor is based on the fact that the motional eigenstates vary depending on the potential depths. This is even true when the two potentials are perfectly identical and are changing in common (no detuning for the carriers).

Radial motion

After cooling the axial degree of freedom to the vibrational ground state the radial motion is expected to remain almost unaltered. As the radial oscillation frequency $\omega_\mathrm{rad} = 2\pi\, 1$ kHz is very different from the axial one $\omega_\mathrm{ax} = 2\pi\, 115$ kHz the exchange of energy between the two degrees of freedom is negligible [43]. After molasses cooling the radial temperature amounts to $T_\mathrm{rad} \approx 10\ \mu$K corresponding to

a mean vibrational number of $\bar{n}_{\mathrm{rad}} \sim 200$. In this limit the quantization of the radial motion can be neglected and the radial atomic position can be treated classically.

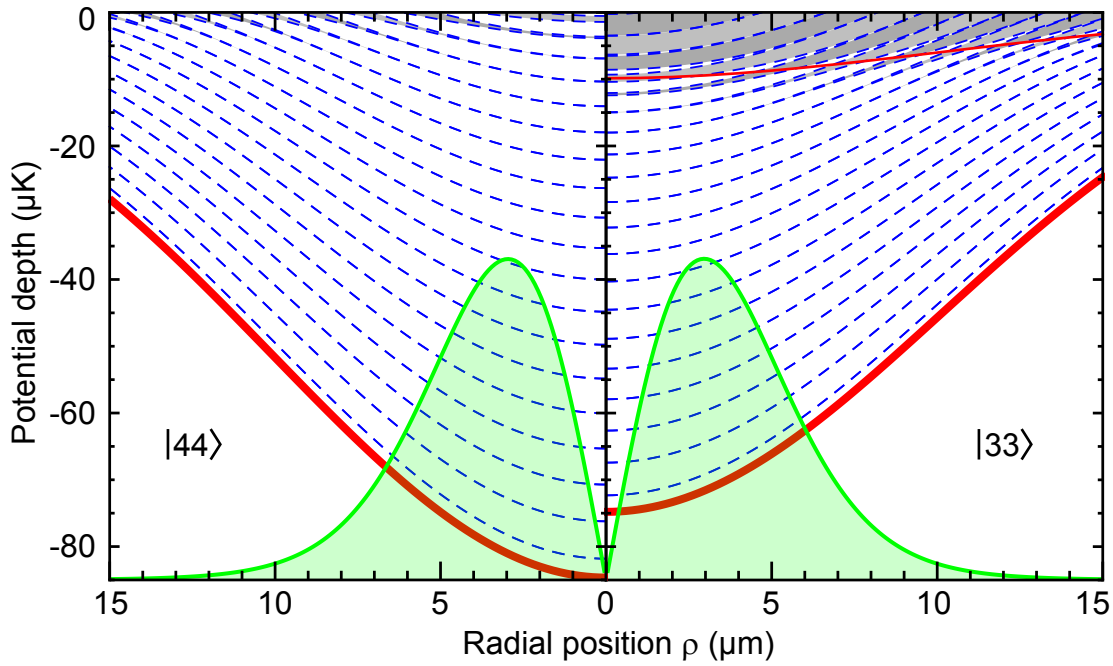

Fig. 2.16: The thick red line indicates the Gaussian shape of the U_{44} and U_{33} potentials along the radial direction. The classical probability density to find an atom at the distance ρ is denoted by the shaded green line (assuming a radial temperature of 10 μK (see chapter 4). The vibrational states along the axial direction, indicated by the dashed lines, change their total eigenenergy and their spacing when the distance ρ from the trap axis increases. The width of the energy bands is indicated by gray shading. Here, the polarization angle amounts to $\vartheta = 75.5°$ so that the potential U_{33} is shallower than U_{44} and also has a smaller axial contrast where the upper red line indicates its axial trap depth.

Due to the radial position distribution of the atomic ensemble microwave operations are sensitive to position-dependent differences between the potentials U_{44} and U_{33}. Even for perfectly identical potentials the sideband transitions are still affected. In order to understand how the distortion depends on the order of the sideband (see figure 2.12 (b)) we must drop the harmonic approximation for both the axial and the radial confinement. Unlike for a three-dimensional harmonic oscillator the hamiltonian for the lattice potential resulting from a multiplication of a Gaussian with a sine-function is not separable. Hence, the previous calculation of the Bloch states which implied that the axial eigenstates can be calculated independently from the

radial motion is not completely correct. The modeling of this problem can be tackled by comparing the timescales of the axial and the radial motion: At each radial position ρ the local axial eigenenergy states can be considered as properly defined. In this picture, the atoms adiabatically follow the change of the axial eigenstate during a slow radial movement.

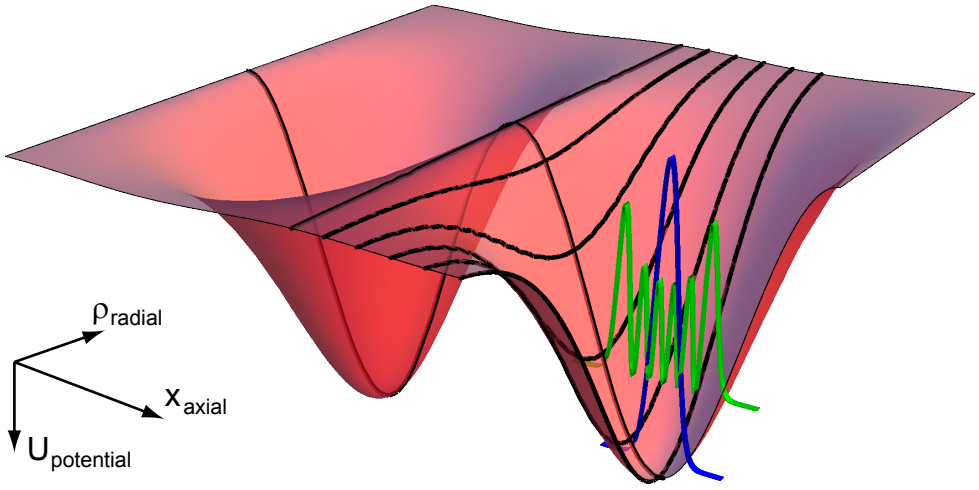

Fig. 2.17: The radial confinement depends on the axial motional state $|n\rangle$. Due to the anharmonicity of the 3D-trapping potential an axially excited atom (e.g. $n = 5$) effectively experiences less light shift and is thus more loosely bound along the radial direction. This is the counterpart to the case of figure 2.16 where the axial state varies with the radial position.

The dashed lines in figure 2.16 indicate the variation of the eigenenergies of the axial bands with the radial position ρ although it is slightly anomalous to draw curved eigenenergy levels. These lines have to be interpreted as energy levels corresponding to the sum of the local radial potential energy and the local axial eigenenergy. They suggest that the radial confinement depends on the axial vibrational state (e.g. an atom in the axial state $n = 5$ experiences a shallower radial potential compared to an atom in the axial ground state). This is indeed the case as is illustrated in figure 2.17.

Note that the spacing between the eigenenergies also varies with the radial position. The same is true for inter-potential spacings. As microwave transitions connect a dashed line of the $|44\rangle$-potential with a dashed line of the $|33\rangle$-potential the resonance frequency of a sideband depends on the radial position of the atom. In addition, according to the shallower axial potential at the distance ρ from the lattice axis the highest axial bands switch one-by-one to positive energies. The situation is

similar in the case of the $|33\rangle$-potential. Here, due to the reduced potential contrast the bands of the upper most bound states become very broad and finally merge to a quasi-continuum although they are still negative. This effect needs to be considered for the highest order sidebands: Atoms with an energy above the axial confinement most probably also contribute to the losses shown in figure 2.13.

For comparison, figure 2.16 shows the classical probability density to find an atom at the distance ρ from the lattice axis

$$\eta_{\mathrm{rad}}(\rho) = \frac{\rho}{\sigma_\rho^2}\,\exp(-\frac{\rho^2}{2\,\sigma_\rho^2}) \qquad \text{with} \qquad \sigma_\rho = \sqrt{\frac{k_\mathrm{B}\,T_{\mathrm{rad}}}{M\,\omega_{\mathrm{rad}}^2}}\,. \tag{2.4.3}$$

It is derived by assuming a 2D-Boltzmann distribution with temperature T_{rad} for the radial motion and by approximating the radial confinement by a harmonic potential with oscillation frequency ω_{rad}.

An analytical expression for the thermal frequency distribution can be derived by assuming that the atomic radial position and thus its detuning is fixed during the duration of the microwave pulse. This assumptions is justified by comparing the radial oscillation period of ∼1 ms with the length of a typically used Gaussian microwave pulse ($e^{-1/2}$-width of 15 μs). Furthermore, each dashed line in figure 2.16 is approximated by a parabola with a different oscillation frequency $\omega_{\mathrm{rad},n}$ for each axial state $|n\rangle$. In this approximation, the spacing between two axial states depends quadratically on the radial position

$$E_{44,n}(\rho) - E_{33,n'}(\rho) = K_{nn'}\,\rho^2. \tag{2.4.4}$$

The position distribution 2.4.3 can be directly cast into a detuning distribution defined by equation 2.4.1 with

$$\gamma_\mathrm{b} = \frac{K_{nn'}}{\pi\,\hbar}\,\sigma_\rho^2. \tag{2.4.5}$$

In particular, the asymmetric width γ_b depends on the order of the sideband and, less strongly, on the involved vibrational states. For our parameters figures 2.18 (a/e) indicate the magnitude of thermal broadening. Qualitatively, the conclusions are similar to those drawn for the broadening due to laser power fluctuations but the thermal broadening is an order of magnitude stronger.

A closer look to the theoretical curves for a fixed lattice displacement reveals the linear increase of γ_b of 5 kHz per order of sideband. This can be compared to figure 2.12 where the measured increase of γ_b amounts to 1.8±0.4 kHz per order of sideband. Obviously, the measured peak asymmetries are by a factor of two

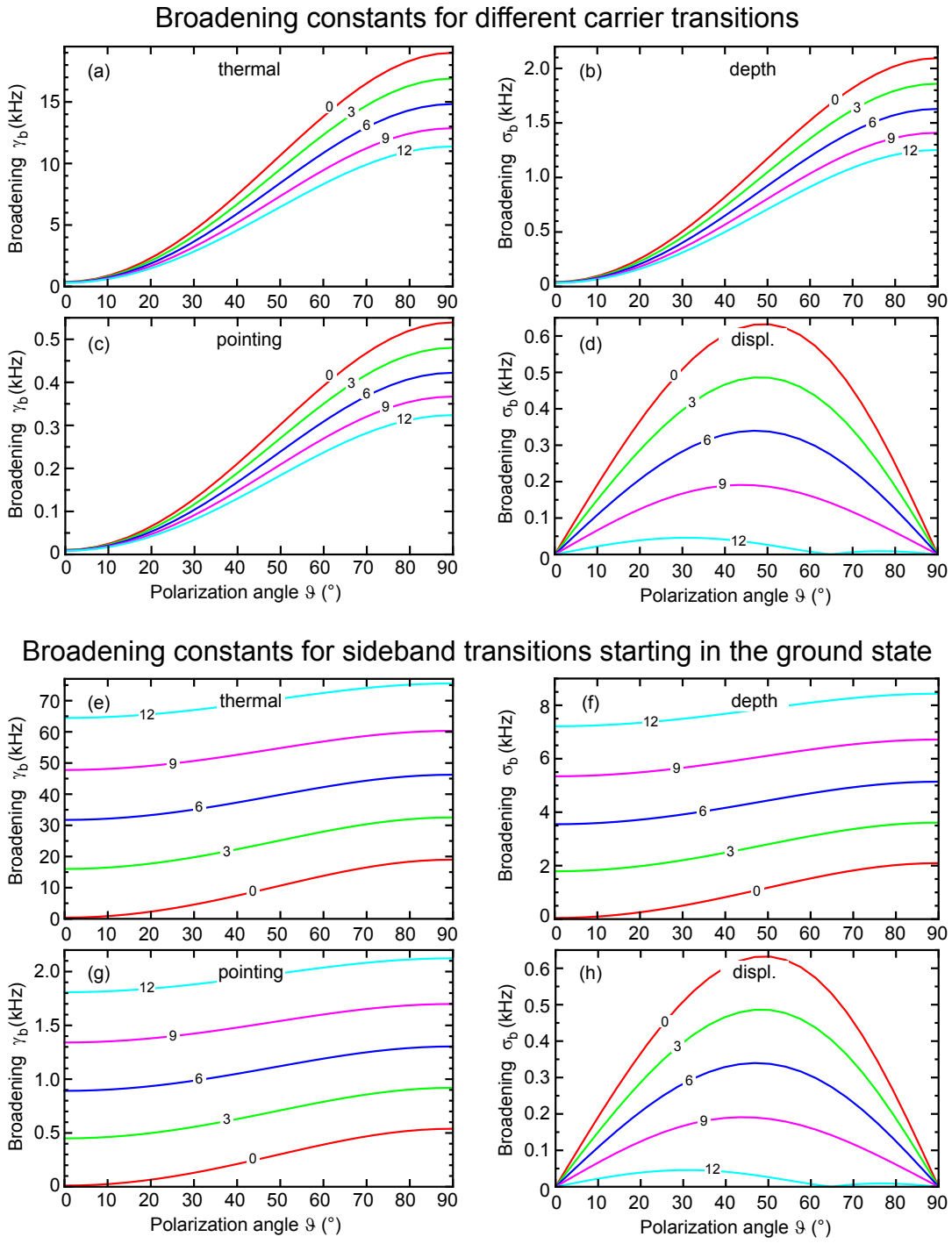

Fig. 2.18: Broadening of the carrier transitions $|44, n\rangle \leftrightarrow |33, n\rangle$ and sideband transitions $|44, 0\rangle \leftrightarrow |33, n\rangle$ with n={0, 3, 6, 9, 12} due to four different noise sources.

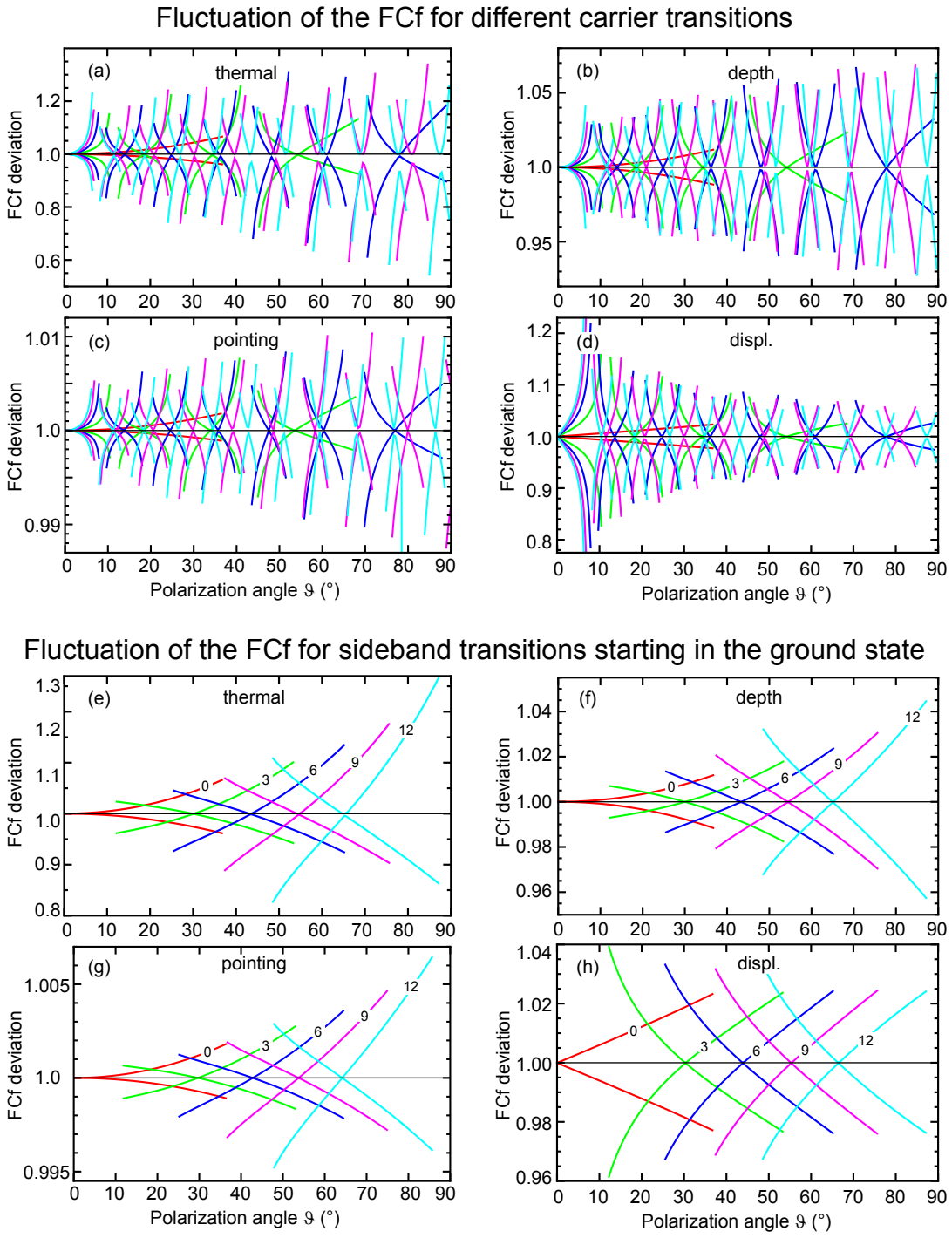

Fig. 2.19: The fluctuation of the Franck-Condon factor of the carrier transitions $|44,n\rangle \leftrightarrow |33,n\rangle$ and sideband transitions $|44,0\rangle \leftrightarrow |33,n\rangle$ with n={0, 3, 6, 9, 12} due to four different noise sources (the same color code for all sub-figures). The definition of the confidence interval for the fluctuation is given in figure 2.14.

smaller than the calculated expectation. Because the radial confinement cannot deviate much from the expectation the curvature of the lines in figure 2.16 and thus the coefficients $K_{n,n'}$ are fairly reliable. A second explanation could be a radial temperature which is significantly smaller than $T_{\mathrm{rad}} = 10\ \mu\mathrm{K}$ (see section 4.1.1). This is questionable as this would mean an exceptionally low temperature for a molasses cooled sample. On the other hand, the sideband cooling process itself influences the radial motion and possibly leads to a non thermal energy distribution (see figure 3.6). Also possible that the assumption of a fixed detuning during the duration of the microwave pulse does not hold and that a quantum mechanical treatment of the radial motion is required. This is an extraordinary computational effort so that the discrepancy between theory and experiment must be left open here.

As the local axial vibrational state depends on the radial position so do the corresponding Franck-Condon factors. A subtle detail for the analysis is the fact that the distribution of the radial position is not Gaussian (see figure 2.16). For simplicity the "confidence interval" for the position distribution is defined by choosing symmetrical bounds around the mean radial position at $\rho_{\mathrm{mean}} \approx 3\,\mu\mathrm{m}$. Then, the maximum and the minimum value of the Franck-Condon factor within this position range determine the width of the Franck-Condon factor distribution.

Polarization inhomogeneity

For the preceding discussion a homogeneous polarization across the beam profile is assumed. If this is not the case (see figure 1.10) the size of the atomic sample (dominated by the radial motion) plays an even more important role. The current simulation of the lattice potential does not take into account this important effect. Although this is in principle possible (see figure 1.10) there is no simple conclusion which can be drawn from this. Additionally, the gradient is not very well quantified at this moment as this requires a sub-degree resolution of the rotation angle of the wave plates used. Experimentally, this problem is on the way to be solved both by cooling along the radial degree of freedom and by compensating the polarization inhomogeneity using glass plates with controlled mechanical stress applied to them.

Displacement

Naturally, a fluctuating lattice displacement directly alters the Franck-Condon factors. The standard deviation for the displacement fluctuation used here amounts to $\pm 0.001\,\lambda_{\mathrm{lat}}/2 = 0.433\,\mathrm{nm}$ ($\vartheta \sim 0.2°$) and is limited by the purity of the computer control voltage and by the stability of the EOM-driver voltage. Although the stability of the displacement is already quite high the Franck-Condon factor still can show a fluctuation on the order of 10 % especially for the carrier transitions at small polarization angles. This underlines the importance of an equal beam path for both

polarization components of the trapping beam and that the lattice shift is solely caused by the EOM (see section 1.2.2).

When the displacement is varied with a a small amplitude the depth of the $|44\rangle$-lattice ideally remains constant while that of the $|33\rangle$-lattice changes. This is similar to a direct change of the trap depth and thus leads to a symmetric broadening contribution σ_b. The approximation of a linear variation of the depth with a small change of the displacement is valid to a very good degree for most settings. For displacements for which the depth changes quadratically, e.g. for $\Delta x = 0$, the contributions are negligible compared to other fluctuations. The qualitatively different dependencies in figure 2.18 (d) and (h) compared to other broadening mechanisms reflect the small potential wobbling at zero and at maximum displacement and a stronger depth change when the lattice sites are separated by $\lambda_\mathrm{lat}/8$.

Pointing stability

The instability of the beam alignment at the position of the atoms alters the resonance width by affecting the lattice contrast and thus the potential depth. This only becomes important if the two counter propagating beams are misaligned relative to each other. The standard deviation for the misalignment deduced from the radial position of the imaged atoms amounts to ± 1 μm [23]. In contrast to the intrinsic fluctuation of the depth (page 58) a relative beam displacement always leads to a *reduction* of the potential. It thus gives rise to an asymmetric broadening. Luckily, this contribution has the same broadening distribution as that caused by the radial motion and can thus also be quantified by the constant γ_b. Since the relative position of the counter propagating beams has a two-dimensional Gaussian distribution (similar to the radial position of the atoms) it can be reduced to a distribution which only gives information about the separation between the beam axes and which is therefore described by an equation equivalent to 2.4.3 (ρ means then the distance between the axes). To first order the detuning varies quadratically with the axes separation which again has the form of equation 2.4.4. For our experiment the distribution only minimally depends on the radial position of the atom. Combining this two facts yields a detuning distribution which is modeled by equation 2.4.1. Unfortunately, the constant γ_b of the radial motion and of the pointing fluctuation are not additive because the convolution of the distribution 2.4.1 with itself is a more complicated function. Due to the high passive pointing stability, however, its fluctuation can be neglected. It is important to maintain the stability level as the influence of this source grows quadratically.

Quantization field

The fluctuation of the Zeeman splitting between the states $|44\rangle$ and $|33\rangle$ due to the instability of the applied magnetic field is very linear and thus also contributes to

the symmetric broadening constant. From the measured coherence times we deduce its value to be $\sigma_b \approx \pm 1\,\mathrm{kHz}$.

The Franck-Condon factor is not subject to quantization field fluctuations because a homogeneous magnetic field does not change the wave functions by any means. In principle, a strong field gradient introduces a relative displacement between wave functions of different $|F, m_F\rangle$-states [77]. Nevertheless, because of the strong axial confinement the displacement along the axial direction is negligible even for the highest gradients experimentally available in our setup. The displacement is also negligible along the radial degree of freedom as here the quantization field dominates the direction of the local magnetic field.

Long term drifts

The experimental practice shows that once adjusted the setup degrades on the time scale of few hours until it must be realigned to preserve good coherence properties. The elements with the strongest effect are the wave plates and the transport EOM (see figure 1.1). It turns out that the wavelength of the lattice laser also has a strong influence. Here, two questions have to be answered: The influence of a drifting wavelength and the precision of the calculated magic value.

Wave plates In the present investigation all wave plates are assumed to be zero order plates according to their specification. The intrinsic effect of a small rotational drift of the two wave plates $\mathrm{wp2_i}$ and $\mathrm{wp4_i}$ used to prepare the polarization of the incoming beam is ideally negligible. This is due to the used retro-reflecting configuration of the lattice beam setup. Here, the left-handed circular polarization component of the incoming beam is reflected as a right-handed circularly polarized one and vice versa. The flipping element is the quarter wave plate $\mathrm{wp4_r}$ which acts as an effective half wave plate after double-pass. Thus, any imbalance between the circular components of the incoming beam is inverted so that the standing wave intensity of both components is equal. The auto-compensating effect is degraded, when the relative laser intensity of the incoming and the reflected beams are different due to attenuation or unequal waists. The influence of $\mathrm{wp2_i}$ and $\mathrm{wp4_i}$ during the lattice shift depends on their relative order in the beam path. For our setup, where the intensity ratio amounts to $\sim$0.85 due to beam attenuation, the rotational drift causes a shift of any transition by $4\,\mathrm{kHz}/1^\circ$ for the quarter wave plate and by $8\,\mathrm{kHz}/1^\circ$ for the half wave plate. For the half wave plate this is independent of the lattice displacement while for the quarter wave plate the shift varies between $+4\,\mathrm{kHz}/1^\circ$ and $-4\,\mathrm{kHz}/1^\circ$.

The distortion of the Franck-Condon factor is more pronounced which explains, why the alignment of the wave plates is so critical (especially for carrier transitions). The rotation of $\mathrm{wp4_i}$ by 0.1° introduces almost the same lattice shift as a polarization

rotation of $\vartheta = 0.2°$ so that in this case the drift of the Franck-Condon factor is qualitatively and quantitatively similar to the Franck-Condon factor variation presented in figure 2.19 (d) and (h) (here the data has to be interpreted as a slow drift instead of a fluctuation and the lines mark the situation for a rotation of $\pm 0.1°$). In contrast the rotation of $\mathrm{wp2_i}$ leads to a negligible distortion of the Franck-Condon factor.

A rotational drift of the two wave plates $\mathrm{wp4_r}$ and $\mathrm{wp2_r}$ in the retro-reflected part has a striking impact onto the positions of the resonance peaks. This was already mentioned during the explanation of the measurements in figure 2.4 and 2.5. Figure 2.20 now illustrates the expected shift and stretching of a sideband spectrum caused by a rotation of the half wave plate as small as 0.1°. The effect of the quarter wave plate is approximately half of that of the half wave plate. Note that ideally there is no distortion if the displacement is zero. The distortion of the Franck-Condon factor caused by the plate $\mathrm{wp4_r}$ is comparable to the distortion shown in figure 2.19 (d) and (h) when its rotation amounts to 0.1°. $\mathrm{wp2_r}$ however has a rather small influence on the Franck-Condon factor which nevertheless becomes significant at large lattice displacements.

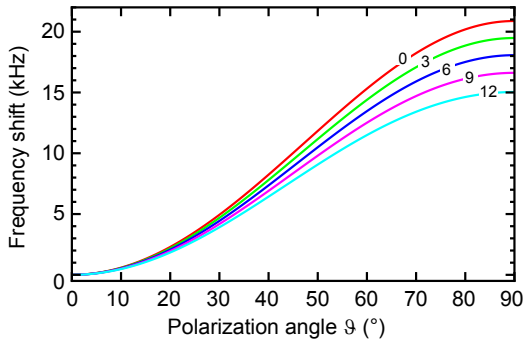

Fig. 2.20: Frequency shift of the sideband transitions $|44, 0\rangle \leftrightarrow |33, n\rangle$ with n={0, 3, 6, 9, 12} due to the rotation of the half wave plate $\mathrm{wp2_r}$ by 0.1 ° depending on the polarization angle ϑ. The effect onto the carrier transitions $|44, n\rangle \leftrightarrow |33, n\rangle$ is quantitatively almost the same except that the spread between the transition is twice as large while the $n = 0$ transition is in both cases the same.

Wavelength drift The wavelength drift primarily has an influence on the coefficients in equation 1.2.1 (see figure 1.6). Additionally, the retardation of the zero order wave plates used is changing which leads to an almost comparable contribution. For a wavelength change of 0.1 nm the distortion is quantitatively comparable

to the depth fluctuation presented in figures 2.18 / 2.19 (b) and (f). The qualitative behavior is also very similar, which is reasonable as the change of the coupling coefficients mainly causes a change of the trap depth.

Experimentally, a wavelength change by 0.1 nm can indeed happen when the Ti:Sapphire laser undergoes a mode jump but this is immediately displayed by the wavemeter which monitors the wavelength. It also indicates slow drifts of the wavelength of up to ±0.01 nm when the laser is not locked to our stabilized reference Fabry-Perot cavity. According to the simulation this small drift should be negligible. Nevertheless, experimentally a sensitivity of the microwave spectrum is observed as it shows a periodic shift when the frequency of the Ti:Sapphire laser is scanned on the GHz scale. This suggests that the atoms are affected by a spurious interference of the trapping laser which most probably originates in the transport EOM. This assumption is based on the fact that the observed phenomenon disappears when the EOM is removed from the optical path. In order to reduce this contribution a thermal stabilization of the EOM and its holder is planned in the future.

Wrong wavelength For the experiments discussed in this work the wavelength of the trapping laser is set to 865.900 nm which results from our calculation employing several approximations (see section 1.2.1). Additionally, some measured transition strengths which enter the calculation are only known with finite accuracy. There is thus an uncertainty in the calculated intensity-to-depth coefficients so that an estimation of possible deviations of the microwave transition properties (resonance frequencies and Franck-Condon factors) is necessary. For simplicity, the once obtained intensity-to-depth coefficients are not recalculated. Instead, the emulation of a wrong magic wavelength is accomplished by artificially using a different value than 865.900 nm assuming that the shape in figure 1.6 (b) remains approximately the same. Thus, the procedure is very similar to the simulation of a drifting wavelength. The measurements presented in figure 2.4 and 2.24 suggest that the used wavelength seems to be slightly blue shifted with respect to the correct magic wavelength of Cesium.

In conclusion, the most important broadening and decoherence source in the current experimental setup is the thermal distribution of the atomic ensemble along the radial degree of freedom. This in particular limits the coherence of the sideband transitions which cannot be improved by making the two trapping potentials as equal as possible. Nevertheless, the technical noise sources still play a significant role. For example, the above analysis revealed which level of stability is required for the EOM-voltage and for the wave plate alignment in order to assure a stable Franck-Condon factor and a stable resonance frequency. Note that in the displaced lattice a simple increase of the microwave power leads to higher off-resonant excitation and thus is not an option to improve the situation.

2.5 Tuning the Franck-Condon-factor

2.5.1 Rabi oscillations on sideband transitions

The coherence of sideband transitions can most directly be tested by driving Rabi-Oscillations. Figure 2.21 shows Rabi-Oscillations for the 1st and the 7th sideband starting from the ground state. The measured Rabi frequencies (32.0 kHz and 21.7 kHz) well agree with the expectation based on the lattice model (31.5 kHz and 23.6 kHz) (dressing must be taken into account, see section 2.2.2). The timescale for the decay of the coherent evolution is quite different for this two traces. We empirically found that the fitting function

$$P_{33}(t) = bg + A_0 \left(1 + \exp(-\sqrt{t/\tau_{\text{decay}}}) \sin(\Omega_{\text{Rabi}} t + \phi_{\text{offset}})\right) \tag{2.5.1}$$

leads to a significantly better fitting result compared to the usually used *exponentially* decaying sine function (see figure 2.21(b)). The fitted decay constant τ_{decay} for the first sideband amounts to (1.53±0.05) ms that for the seventh sideband to (90±10) μs. This is reasonable recalling that the radial motion causes broadening which depends on the order of the sideband as discussed on page 58. The ratio between the two decay times amounts to approximately ten and is comparable to the corresponding ratio between the fitted widths of the high order sideband spectrum shown in figure 2.12.

Similar to the shape of the spectral peaks in fiure 2.10 the shape of the Rabi oscillation envelope also contains information about present decoherence mechanisms (see section 2.4). Figure 2.14(c), e.g., shows that a fluctuating Franck-Condon factor leads to a Gaussian envelope. In case of a detuning distribution the envelope unfortunately cannot be calculated analytically. Figures 2.22(a+b) thus compare the results of a numerical convolution of three different detuning distributions with the Rabi formula given in equation 1.1.4. In case of a Lorentzian distribution the free induction decay familiar from NMR experiments leads to an exponential envelope. For a driven system on the contrary, none of the presented distributions leads to an exponential envelope. This is the reason why different envelopes have been tried for the data fit. Note that moreover the measured Rabi oscillation traces are of the same length as the period of the radial movement. When the average over a static thermal detuning distribution is replaced by the average over individual atomic trajectories with a thermal weighting factor the Rabi envelope is again significantly altered (see figure 2.22(c)). A full theoretical description thus requires a lot of computational power as it is at least not straight forward to extract general conclusions [5].

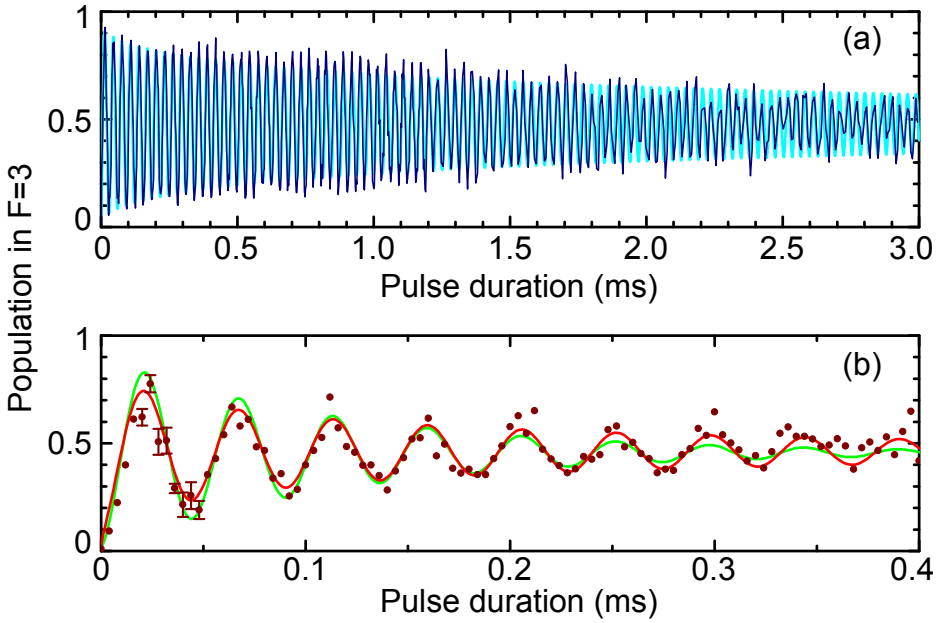

Fig. 2.21: Coherent Rabi oscillations for the sideband transitions (a) $|44,0\rangle \leftrightarrow |33,1\rangle$ with a fitted Rabi frequency of $2\pi(32.0\pm0.1)$ kHz ($\vartheta = 11.6°$) and (b) $|44,0\rangle \leftrightarrow |33,7\rangle$ with a Rabi frequency of $2\pi(21.7\pm0.2)$ kHz ($\vartheta = 50.3°$) . The sinusoidal fitting functions include the empirically found damping term $\exp(\sqrt{t/\tau_{\mathrm{decay}}})$. For comparison the fit with the usual exponentially damped sine function is shown in (b) as a green line exhibiting a faster decay.

An experimentally interesting point concerns the rich motional level structure of the trapping potential. Using the model described in section 2.2.2 the simulation of the state population for the data, e.g. presented in figure 2.21(a), reveals that the motional state is not pure. Due to the strong driving field ($\Omega_{\mathrm{bare}} \lesssim \omega_{\mathrm{ax}}$) off-resonant excitation coherently redistributes the population among several motional states. As figure 2.23 though illustrates the population does not simply spread without bounds. For our parameters it oscillates back and forth between few nearest neighbor states. The initial situation however is also never found again meaning that the population of the initial state is hardly higher than 99%. In the experiment the information about the motional state is traced out. The motional dynamics though remains visible and manifests itself in a kind of beating signal superimposed on top of the main spin oscillation. This also has a significant influence on the observed envelope of the Rabi signal.

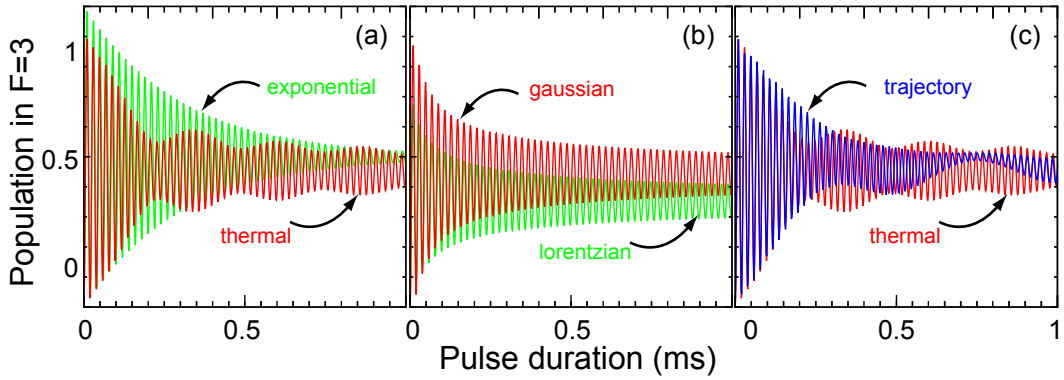

Fig. 2.22: Characteristic envelopes of Rabi oscillations of a two level system with a frequency of $\Omega_R = 2\pi 50$ kHz. (a+b) Three different detuning distributions are all leading to different envelopes (the static thermal distribution is defined by equation 2.4.1). The respective broadening constants (γ_b for the thermal, $e^{-1/2}$ radius for the Gaussian, half maximum radius for the Lorentzian distribution) are all set to 20 kHz. For comparison (a) shows the standard exponential envelope. (c) Comparison of a static thermal distribution and an average over (classical) radial trajectories with otherwise the same experimental parameters.

2.5.2 Rabi frequency depending on the lattice displacement

Comparing the measured Rabi frequency of a sideband transition to the Rabi frequency of a free atom Ω_{bare} directly yields the absolute value of the Franck-Condon factor between the involved motional states (see equation 2.1.2). One remarkable property of the spin dependent potential is that any of the Franck-Condon factors can easily be varied by adjusting the lattice displacement Δx. For comparison, for recoil-induced sideband transitions this is only possible by changing the angle between the propagation axes of the two Raman laser beams. As the Franck-Condon factor in our case is nothing else than the spatial wave function overlap a measurement of the Rabi frequency depending on the displacement provides information about the spatial shape of the motional states. Figure 2.24 shows the measurement of three different wave function overlaps. Very similar results have been independently obtained in a shallow 3D lattice [78, 29]. Related measurements have also been performed with trapped ions but without the tunability option [37].

Our measurement procedure is based on the experimentalists point of view: The resonance position of a desired transition is first determined by measuring a spectrum with a close to π-pulse condition. The resulting resonance frequency thus already includes all possible shifts as there are: the shift due to the wobbling of the $|33\rangle$

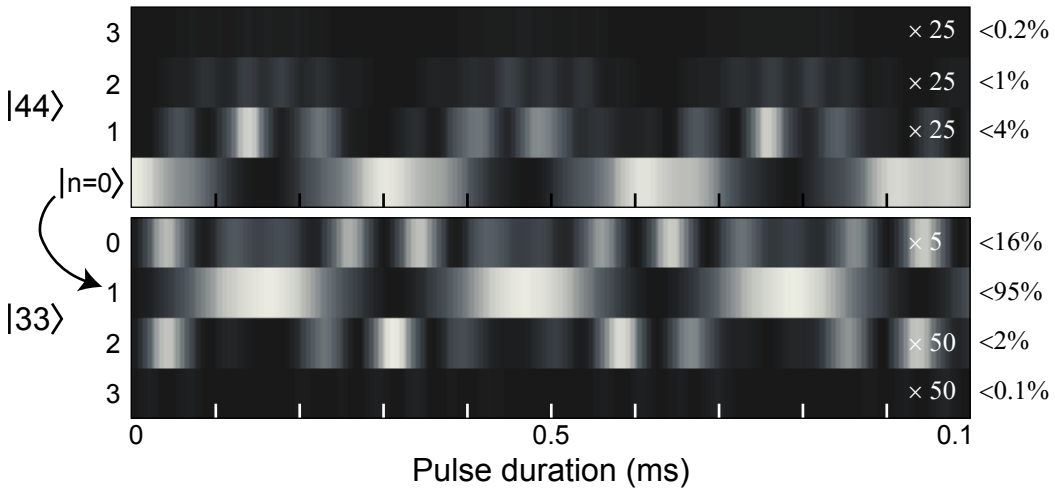

Fig. 2.23: Population of individual vibrational states while the sideband transition $|44,0\rangle \leftrightarrow |33,1\rangle$ is driven with a coupling strength of $\Omega_{\text{bare}} = 2\pi\,59$ kHz (same conditions as for figure 2.21(a)). While the total transfer to the hyperfine state $|33\rangle$ is 99% the population of the target motional state is at most 95%.

potential, deviations from this shift caused by technical imperfections (e.g. shown in figure 2.5) and shifts due to the AC Stark shift (figure 2.9). As the AC Stark shift depends on the field amplitude the spectrum must be recorded with the same microwave power which is used for the measurement of the Rabi oscillations. For the data in figure 2.24 the full microwave power with the maximum Rabi frequency of $\Omega_{\text{bare}} = 2\pi\,59\,\text{kHz}$ is used in order to decrease the influence of decoherence. On the other hand, the determination of the resonance frequency becomes less precise as the length of the π-pulse is relatively short. If not limited by decoherence $\approx$5 Rabi oscillations are recorded. Finally the data are fitted by a single decaying sine function given in equation 2.5.1. The precision of the fitting result for the Rabi frequency is below $\pm$0.2 kHz. Alternatively the Rabi frequency is extracted from the Fourier transform of the traces. Here the maximum of the resonance peak is taken as the resonance position. Both approaches coincide within the confidence interval. A more realistic confidence interval of $\pm$0.5 kHz is however defined by averaging over several repetitions with the same experimental conditions.

The data in figure 2.24 agree quite well with the theoretical prediction of the Franck-Condon factors derived using the band structure model. In particular this results account for the depth change of the potential U_{33} as well as the nonlinear dependence of the displacement Δx on the polarization angle ϑ (see figure 1.8). Note that only the absolute value of the Franck-Condon factor is measurable. This becomes evident by considering that the mathematical definition of the motional

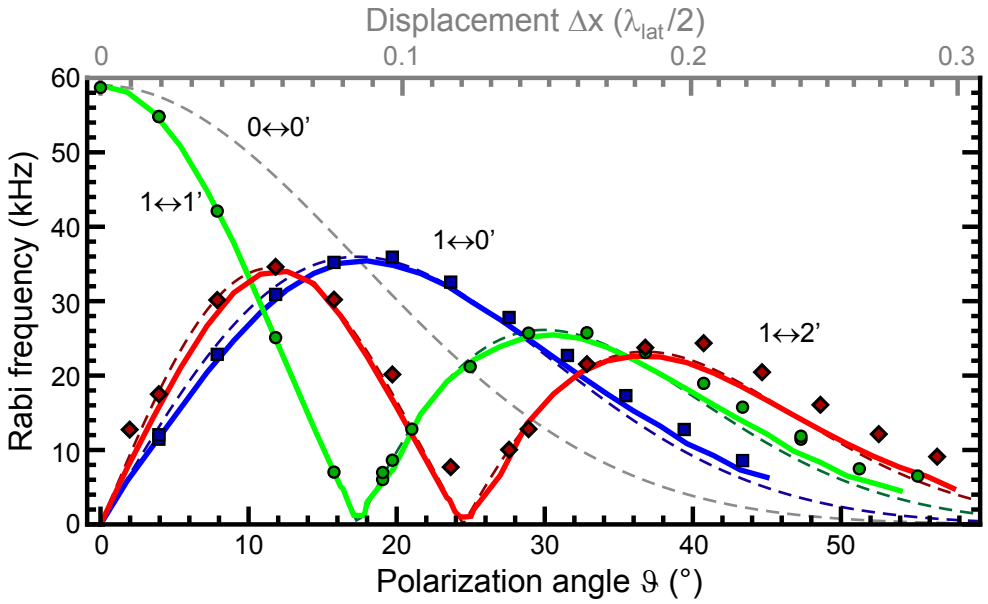

Fig. 2.24: Measurement of the Rabi frequency for the carrier (circles), the first red (diamonds) and the first blue sidebands (rectangles) starting from state $|33, 1\rangle$ for different polarization angles ϑ. Dashed lines indicate the Franck-Condon factors calculated using the band structure model from section 2.2.1. Solid lines result from a model including the microwave dressing (see section 2.2.2) and thermal average over radial trajectories.

states is fixed only up to an individual phase factor. When the atom in contrast is initially prepared in a well known superposition between motional states the relative phase between the state amplitudes indeed has a strong influence on the observed Rabi signal.

For large displacements the simple calculation of the Franck-Condon factor systematically deviates from the measured Rabi frequencies. We thus extended the theory by firstly taking into account the off-resonant microwave coupling between the motional states. As the investigation of the simple three level system on page 46 shows dressing changes the observed Rabi frequency.

The theory secondly includes the thermal radial motion at 10 μK as this contribution is expected to be the largest among all broadening sources. In brief, this is accomplished by computing the Rabi oscillations for individual radial trajectories and by combining them to a thermally averaged theoretical trace. This trace is finally analyzed with the same procedure as the experimental data. As figure 2.24 reveals all this considerations do not significantly change the initial result of the simple model. As the measured data reproducibly deviate from the theory the discrepancy must stem from systematic potential distortion probably the same which

would explain the discrepancy in the high order sideband spectrum in figure 2.10.

In principle, the measurement of the Franck-Condon factor can be very precise as it is based on a frequency measurement. It thus also allows for a precise measurement of e.g. the lattice displacement: Shifts on sub-nanometer scale already introduce a significant change of the Franck-Condon factor. For comparison, the size of the ground state wave packet in our setup amounts to $x_{\mathrm{ax}} = \sqrt{\hbar/\omega_{\mathrm{ax}} M} \approx 25$ nm. The tunability of the wave-function overlap can have many applications in the coherent manipulation of the atomic motional state as e.g. proposed and demonstrated in [94, 32, 95, 84, 96, 33] for a harmonic oscillator potential and in [97, 34] for periodic potentials.

Chapter 3

Ground state cooling in a state dependent potential

It is natural that for high precision experiments the sample under investigation must be initialized in an as pure as possible quantum mechanical state. For our system this applies to the internal as well as to the motional states of the trapped atoms. During the last decades various schemes aiming for cooling an atomic sample to the vibrational ground state have been considered and experimentally realized [40, 24, 98]. Here, we concentrate on the so-called resolved sideband cooling technique which was first demonstrated on trapped ions [99] but is also routinely applied to neutral atoms trapped in optical lattices [9, 25, 26] or even to micro-mechanical objects [100]. In experiments with trapped ions a ground state occupation probability as high as 99.9% was demonstrated [101].

In all these experiments the cooling mechanism is based on the recoil of an optical photon. Cooling schemes based on long wave length radiation have rarely been suggested [102, 103, 104] or experimentally tested [105]. Moreover, they often are based on the Sisyphus cooling scheme which mostly applies to classically moving atoms. In the previous chapter I demonstrated that in combination with a state-dependent trapping potential microwave radiation is capable to induce resolved sideband transitions between quantized motional states. In this chapter I will show that by adding a spontaneous process it is straight forward to realize a ground state cooling scheme (1D in our case) fully competitive with the laser-based technique.

3.1 Cooling the axial degree of freedom

3.1.1 Cooling scheme

The resolved sideband cooling scheme is a typical example of dark-state cooling [67, 106]. It exploits the fact that atoms which reach the vibrational ground state are ideally isolated from all perturbations and can thus accumulate in this state. The cooling cycle which performs pumping towards the axial ground state in our experiment is sketched in figure 3.1. It starts by a microwave transition tuned to the

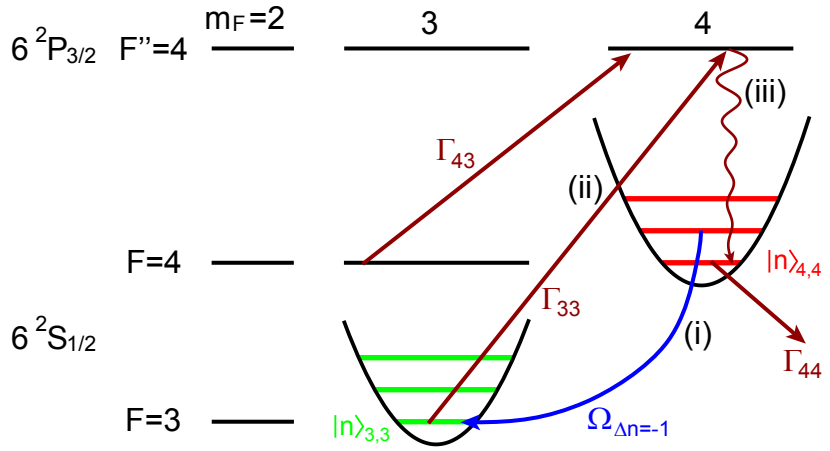

Fig. 3.1: Scheme for the microwave-induced resolved sideband cooling technique. (i) The microwave field tuned to the first blue sideband induces a $|44, n\rangle \leftrightarrow |33, n-1\rangle$ transition and thus decreases the motional quantum number by one. (ii+iii) The cooling cycle is closed by an optical repumping photon resonant with the $F = 3 \rightarrow F'' = 4$ transition ('repumping' in figure 1.4 with the pumping rate Γ_{33}). An additional laser resonant with the $F \rightarrow F'' = 4$ transition preserves spin polarization ('optical pumping' laser in figure 1.4 with the pumping rate Γ_{43}). Atoms pumped to the dark state $|44, 0\rangle$ stop to participate in the cooling cycle unless they are off-resonantly excited (leakage rate Γ_{44}).

first blue sideband and thus decreases the motional quantum number by one. This process is coherent and the population thus oscillates between the states $|44, n\rangle$ and $|33, n-1\rangle$ with the Rabi frequency $\Omega_{\Delta n=-1}$. It is equivalent to the Raman transition usually used for sideband cooling [81] but in our case the transition requires a nonzero displacement of the lattice potentials. It is slightly unfamiliar to see the blue sideband providing cooling. This is only due to the fact that the dark state is the energetically higher hyperfine state. As the lifetime of the dark state $|44\rangle$ is

equal to that of the 'auxiliary' state $|33\rangle$ this is irrelevant for the cooling procedure.

The cooling cycle is completed by a laser transition which pumps the atoms back to the $|44\rangle$ hyperfine state. The spontaneous decay involved in the scattering event thereby interrupts the coherent microwave evolution which is important as only irreversible processes ar able to provide net cooling. Assuming that the scattered photon does not significantly heat the atom their energy is diminished by one vibrational quantum per cycle. When the atom reaches the dark state $|44, 0\rangle$ it is neither affected by the microwave field nor by the repumping lasers. Independent of the initial motional state all atoms eventually accumulate in this state which shows that the entropy of the system is reduced.

The cooling operation can alternatively be interpreted as an extension of the usual optical pumping procedure sketched in figure 1.4. The microwave radiation thereby depopulates the usually dark hyperfine state $|44\rangle$ except for its motional ground state. After the cooling sequence the atomic ensemble is thus both spin polarized and ground state cooled which are ideal starting conditions. The purity of the prepared state is basically limited by the depletion of the dark state due to residual off-resonant excitation processes characterized by the leakage rate Γ_{44}.

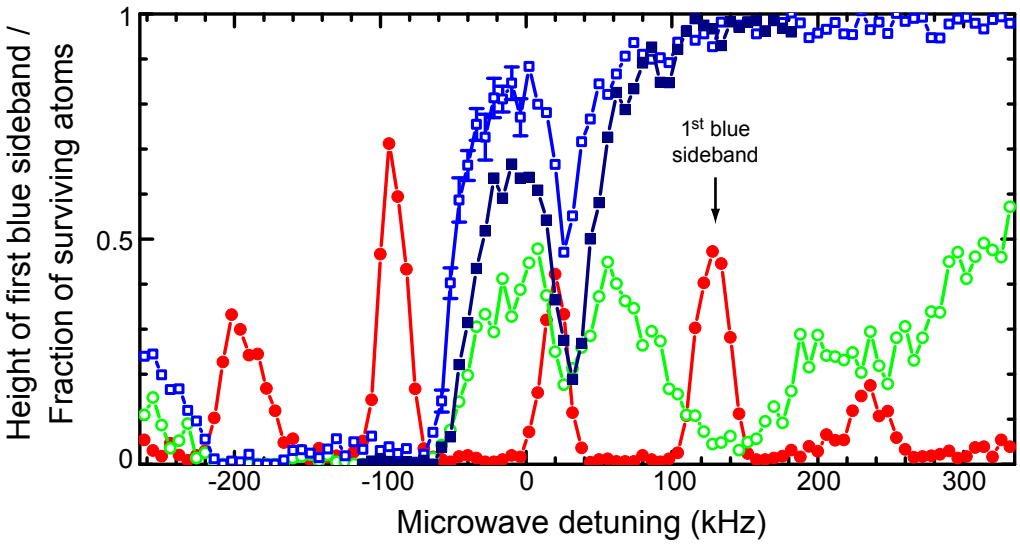

Fig. 3.2: Scan of the microwave frequency (Ω_{bare}=16 kHz) during the cooling process. A usual spectrum of an uncooled sample (•) marks the position of the sidebands. The height of the blue sideband (○) and the fraction of surviving atoms (□) after the 'cooling' period characterize its performance. (■) is the same as (□) but with a stronger microwave coupling Ω_{bare}=27 kHz).

The height of the first blue sideband provides a good measure for the cooling efficiency. As it is not possible to reduce the vibrational quantum number starting from

the ground state it is suppressed compared to the red sideband. In order to determine the optimum cooling parameters each parameter is scanned and a subsequent measurement of the height of the first blue sideband reveals the cooling performance. A typical trace showing a result of a scan of the microwave frequency during the cooling process is presented in figure 3.2. The optimum frequency for cooling should of course be in the vicinity of the first blue sideband which is confirmed by its suppression in this measurement. A less pronounced suppression is also present at the position of the second blue sideband. The scan moreover reveals the absence of the blue sideband in a very broad red detuned frequency range and also a dip at the position of the carrier. Similar features are present when the fraction of remaining atoms is measured instead of the height of the blue sideband (no push-out). This countercheck reveals that at wrong frequencies the atoms are strongly heated and eventually escape from the trap. Optimum cooling parameters thus must satisfy two criteria: the blue sideband must be suppressed as far as possible but at the same time atom losses must be negligible.

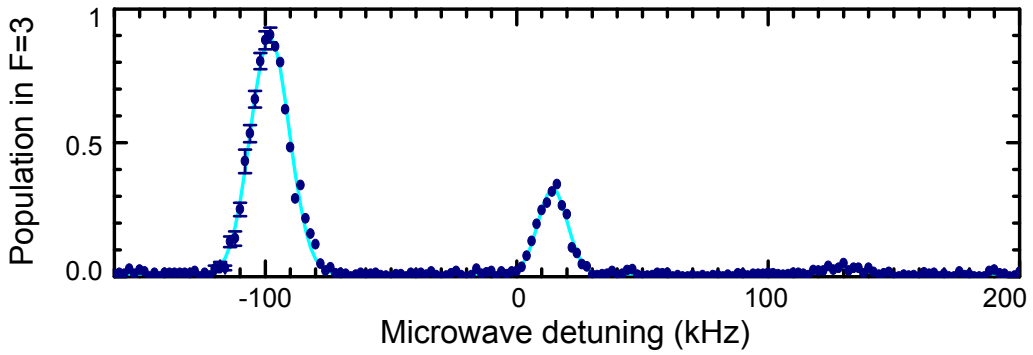

Fig. 3.3: Microwave spectrum after ground state cooling including the first order sidebands. The ratio between the heights of the red and blue sidebands is used for the calculation of the 1D atomic temperature along the lattice axis.

After optimization a spectrum showing both first order sidebands similar to that in figure 3.3 is used for the determination of the resulting atomic temperature [107]. For best visibility a gaussian microwave pulse satisfying the π-pulse condition for the first red sideband $|44,0\rangle \leftrightarrow |33,1\rangle$ is used. In principle, due to the wobbling of the potential U_{33}, the Franck-Condon factor for the blue sideband $|44,1\rangle \leftrightarrow |33,0\rangle$ differs by 0.3% but this is neglected here. In the limit of a low temperature the heights of the red and blue sidebands are proportional to the population of the ground state $P_{44,0}$ and the first excited state $P_{44,1}$, respectively. By assuming a thermal distribution and the harmonic oscillator approximation for the potential the ratio between the sideband heights is thus proportional to the Boltzmann factor

which is related to the average motional quantum number

$$\frac{P_{44,1}}{P_{44,0}} = \exp(-\frac{\hbar\omega_{\mathrm{ax}}}{k_{\mathrm{B}}T_{\mathrm{ax}}}) = \frac{\langle n\rangle}{\langle n\rangle + 1} \qquad \text{with} \qquad \langle n\rangle = (\exp(\frac{\hbar\omega_{\mathrm{ax}}}{k_{\mathrm{B}}T_{\mathrm{ax}}}) - 1)^{-1}. \quad (3.1.1)$$

The fitted heights of the sideband peaks in figure 3.3 amount to 0.885 ± 0.007 and 0.027 ± 0.007, respectively. The measured mean vibrational quantum number thus amounts to $\langle n\rangle = 0.03 \pm 0.01$ corresponding to a ground state population of $n_{\mathrm{grndst}} \approx 97\%$ along the axial degree of freedom. Due to broadening effects the more appropriate measure for the transition strength is the peak area. For the sufficiently short pulse length used here the Fourier width however dominates and the discrepancy between the two methods is much smaller than the confidence intervals of the measurement. We thus typically use the height of the blue sideband in order to quantify the cooling performance. Table 3.1 summarizes the experimental parameters for optimal cooling in our setup.

Ω_{bare}	ϑ	Γ_{33}	Γ_{43}	Γ_{44}
2π 16 kHz	4.5°	35 10^3/s	10 10^3/s	15 1/s

Tab. 3.1: Experimental parameters for optimal cooling in our setup. Ω_{bare} labels the Rabi frequency at zero displacement and ϑ denotes the polarization angle of the lattice. The low value of the pumping rate Γ_{43} results from the low power of the optical pumping beam which otherwise significantly increases the leakage rate Γ_{44}. The rates are defined as the inverse of the e^{-1}-lifetime of the corresponding hyperfine state.

Our cooling result is comparable to previously reported values from experiments employing the sideband cooling technique in optical lattices [9, 25, 26]. Note that, however, our microwave based approach is not limited by the purity of the driving field. A comparably small linewidth using laser transitions requires significantly more experimental effort. The limit in our setup is entirely determined by technical contributions to the leakage rate Γ_{44} which quantifies the 'darkness' of the dark state. Here, first of all, the polarization purity of the optical pumping beams plays a crucial role. The main distortion thereby stems from the small angle between the axis of the optical pumping beam and the quantization axis pointing along the lattice potential (see page 8). A second fundamental contribution originates from off-resonant photon scattering of the trapping laser. The power of both optical pumping beams was minimized until both leakage contributions where approximately equal.

Microwave-induced sideband cooling is attractive due to the absence of heating caused by photon scattering of Raman lasers. Moreover, very well controllable

generators guarantee reliable performance and a simple experimental setup. The microwave field is also more homogeneous which is advantages for large atomic samples. On the other hand its disadvantage is the additional projection heating caused by the optical repumping process in a displaced potential as is theoretically elucidated in the following subsection.

3.1.2 Theory for the cooling process

Sideband cooling has been thoroughly studied in the past (e.g. [67, 108, 106, 81]). Here, the question of interest is the cooling efficiency in displaced state-dependent potentials which has not been explicitly considered yet. Moreover, the lattice displacement is a tunable parameter in our case and the determination of its optimum value requires some investigation.

In the experiment, the microwave and the two repumping lasers operate continuously for a specified cooling period which is typically 20 ms in our case. Theoretically, the cooling process is described by master equations [54], a coherent form of rate equations. The continuous operation simplifies the experimental sequence and does not require fast electro or acousto-optic modulators for fast switching of the repumping lasers. In general the master equation determining the time evolution of a density matrix ρ of a system is given by

$$\frac{d}{dt}\rho = -\frac{i}{\hbar}(\hat{H}\,\rho - \rho\,\hat{H}) + \mathcal{L}(\rho). \tag{3.1.2}$$

Here, the hamiltonian $\hat{H}$ considers the coherent evolution and the Liouvillian $\mathcal{L}$ takes into account the dissipative decay processes.

An accurate consideration of the photon scattering processes is important as the usually valid assumption of a preserved motional quantum number can be strongly violated in our case. This is because of the displaced state-dependent potentials for the generation of the sideband transitions. When a scattered photon involves a change of the hyperfine state the motional state before the scattering process is projected onto the spatially shifted set of eigenstates (additionally to the small recoil-induced shift in the momentum space).

The hamiltonian relevant for our cooling scheme is similar to that in equation 2.2.6 but it now includes the states $|F = 4, m_\mathrm{F} = 3, n\rangle = |43, n\rangle$ (note that

as previously all entries are block matrices).

$$\hat{H}_{\text{cooling}} = \begin{pmatrix} E_{44,n} & \frac{1}{2}\hbar\,\Omega_{44,\text{n}\leftrightarrow 33,\text{n}} & 0 \\ \frac{1}{2}\hbar\,\Omega_{33,\text{n}\leftrightarrow 44,\text{n}} & E_{33,n} + \hbar\,\omega_{\text{mw}} & 0 \\ 0 & 0 & E_{43,n} \end{pmatrix} \tag{3.1.3}$$

The hyperfine state $|43\rangle$ is not coupled to the microwave field (see page 51) but its consideration is important because after optical excitation to the state $|F'' = 4, m_{\text{F}}'' = 4\rangle$ there is a large probability for the atoms to decay to $|43\rangle$ (see figure 3.1). Other hyperfine states are ignored because of their low population. The description of the pumping process by the Liouvillian is modeled by an effective decay rate. For any state $|F, m_{\text{F}}, n\rangle \equiv |a\rangle$ involved in the cooling process which can decay to state $|F', m_{\text{F}}', n'\rangle \equiv |b\rangle$ the Liouvillian is defined by

$$\mathcal{L}_{a,b}(\rho) = \begin{pmatrix} -\gamma_{a\to b}\,\rho_a & -\frac{1}{2}\gamma_{a\to b}\,\rho_{a,b} & -\frac{1}{2}\gamma_{a\to b}\,\rho_{a,c} \\ -\frac{1}{2}\gamma_{a\to b}\,\rho_{b,a} & \gamma_{a\to b}\,\rho_a & 0 \\ -\frac{1}{2}\gamma_{a\to b}\,\rho_{c,a} & 0 & 0 \end{pmatrix} \tag{3.1.4}$$

Here, ρ_a labels the population of the state $|a\rangle$ and $\gamma_{a\to b}$ denotes the effective incoherent decay rate for the process $|a\rangle \xrightarrow{\text{decay}} |b\rangle$. The diagonal matrix elements reflect the population transfer between these states and the off-diagonal matrix elements the decay of the corresponding coherences. Note that off-diagonal elements with any other state $|c\rangle$ are also affected.

The decay rates $\gamma_{F,m_{\text{F}},n\to F',m_{\text{F}}',n'}$ do have three contributions. In the simulation I make the simplifying assumption that there is only one optically excited state namely $|F'' = 4, m_{\text{F}}'' = 4\rangle$. The first contribution characterizes the power of the pumping laser for the transition $|F, m_{\text{F}}\rangle \to |F'' = 4, m_{\text{F}}'' = 4\rangle$ which is modeled by the excitation rate $\Gamma_{F,m_{\text{F}}}$ (see figure 3.1). The second contribution takes into account the branching ratio of $|F'' = 4, m_{\text{F}}'' = 4\rangle$. The explicit consideration of the optically excited state is omitted because due to its short lifetime (30 ns) compared to the motional time scale (10 μs) it can be adiabatically eliminated. Thus only effective branching ratios $r_{F,m_{\text{F}}\to F',m_{\text{F}}'}$ between ground states are used. For the leakage process modeled by the rate Γ_{44} only the two target states $|33\rangle$ and $|43\rangle$ are considered assuming the same probability for both processes. The third contribution, which is peculiar to our scheme, is the wave function overlap between motional states which not only takes into account the momentum kick of the scattered photon but also the spatial shift of the potentials (for simplicity the emission of the scattered photon is assumed to be spherically symmetric). For the Bloch states (see equation 2.2.3) the recoil-induced momentum shift simply adds to the Bloch vector κ. The wave

function overlap between two Bloch states with a relative shift in momentum space and in spatial space can thus be again efficiently computed via the scalar product between the corresponding coefficient vectors (see page 43)

$$\gamma_{F,m_F,n\to F',m'_F,n'} = r_{F,m_F\to F',m'_F}\,\Gamma_{F,m_F} \times |\langle n'_{F',m'_F}|n_{F,m_F}\rangle|^2. \tag{3.1.5}$$

The last factor in this expression is responsible for the redistribution of the population among the vibrational states during the repumping process. It reveals that for state dependent potentials both, the momentum kicks and the spatial displacement are relevant. For efficient cooling in a harmonic trap, thus, the generalized Lamb-Dicke factor defined in equaiton 2.1.11 has to satisfy the condition $\eta \ll 1$. Figure 3.4(a) shows the theoretically expected heating amount per cooling cycle in our setup assuming that only one photon is required in order to transfer the atom from state $|33\rangle$ to state $|44\rangle$. Heating at zero displacement with $\vartheta = 0$ comes solely from the photon recoil.

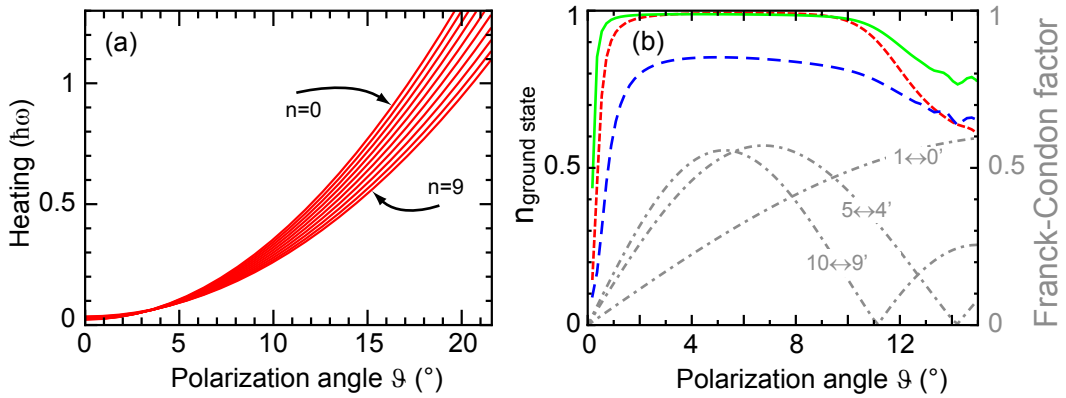

Fig. 3.4: (a) Heating per cooling cycle caused by one repumping photon depending on the spatial displacement. For $\vartheta = 0$ only recoil heating is present. Different lines correspond to different initial motional states. (b) Calculated steady state ground state population n_{grndst} depending on the polarization angle ϑ for three different microwave powers ({dotted, solid, dashed} lines correspond to Ω_{bare}={5, 15, 60} kHz). The dash-dotted lines indicate the Franck-Condon factors for three exemplary sideband transitions.

The bounds for the lattice displacement range leading to optimal cooling in our setup are set by the vanishing strength of the sideband transitions at small polarization angles and by heating due to repumping photons at large polarization angles (see figure 3.4(b)). As the comparison between panel (a) and (b) of figure 3.4 reveals the ground state population for larger displacements drops off at a polarization an-

gle at which the projection heating rises above 0.5 vibrational quanta per cooling cycle. At the same time this drop is located at a position where the Franck-Condon factors of some first order sidebands already possess a minimum (see panel (b)). The reduction of the cooling efficiency thus seems to be a combination of both effects: with larger displacements each repumping process projects the motional state onto higher vibrational states which at the same time are less quickly cooled (or even not at all). Our calculation, however, is less precise in this regime as first the maximum considered vibrational quantum number is set to n=15 due to computational effort. Moreover, the theoretical model does not take into account atom losses when they are excited to the highest trapped Bloch bands or even above. Note, however, that the excitation to non trapped Bloch bands with positive energy is quite small as the main heating originates from unfavorable projections of the motional state within a conservative potential.

The theoretical results reveal that the ground state population n_{grndst} robustly reaches 99% over a quite broad range of polarization angles and is optimum at $\vartheta = 5°$. At this polarization angle the projection heating only slightly exceeds the unavoidable recoil-induced heating. The displacement range within which efficient cooling is possible corresponds to a Lamb-Dicke parameter range of η=0.15-0.7 (see equation 2.1.11). This includes quite large values compared to other experiments exploiting sideband cooling [24, 9]. The theoretical expectation is confirmed by our experimental investigations.

Figure 3.5(a) shows the achievable steady state ground state population n_{grndst} depending on the microwave frequency during the cooling process at $\vartheta = 4.5°$. Figures 3.4(b) and 3.5(a) at the same time compare n_{grndst} achievable at three different microwave powers within the experimentally accessible range. On the one hand the Rabi frequency for the first sideband should be large in order to compete with heating mechanisms. At the same time the Rabi frequency of the $|44, 0\rangle \leftrightarrow |33, 0\rangle$ carrier transition should be small with respect to the vibrational energy spacing ω_{ax} because off-resonant microwave excitation depopulates the dark state otherwise. For a fixed polarization angle there exists a well-defined optimal value for the microwave power.

For our setup (and its heating processes) the highest ground state population is reached using a free atom Rabi frequency around $\Omega_{\mathrm{bare}} = 2\pi 5$ kHz. Experimentally, though, we found $\Omega_{\mathrm{bare}} = 2\pi 16$ kHz to be a more comfortable value. Figure 3.5 indicates two reasons for the choice of a slightly higher microwave power. Panel (a) points out that cooling at higher microwave powers is less sensitive to drifts of the sideband spectrum caused by slow misalignments of the experimental setup. At the same time the steady state results are almost the same. Panel (b) shows the time scale of the cooling process. It reveals that if Ω_{bare} is too small the low steady state limit is not yet reached within a fixed cooling duration. In principle, an optimized

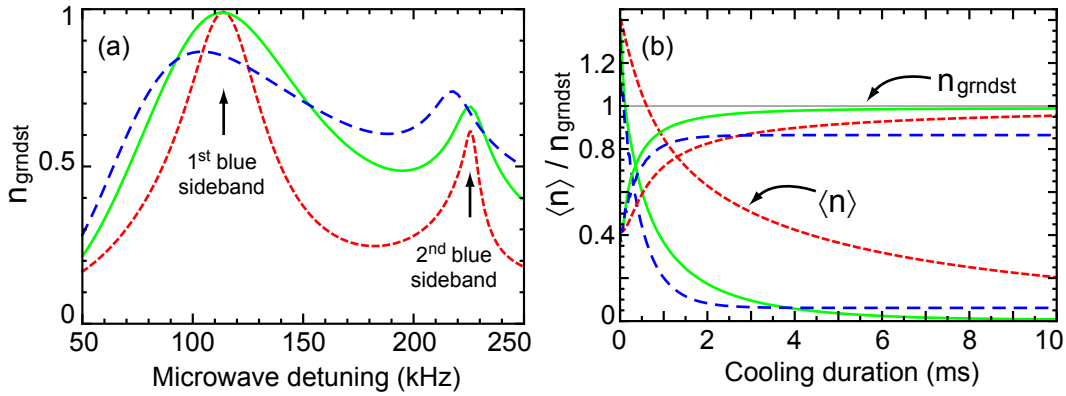

Fig. 3.5: (a) Calculated steady state ground state population n_{grndst} depending on the frequency of the cooling microwave pulse for three different microwave powers ({dotted, solid, dashed} lines correspond to Ω_{bare}={5, 15, 60} kHz). (b) The time evolution of the average quantum number $\langle n\rangle$ and of the ground state population n_{grndst} during the cooling process. The mean vibrational population for the initial thermal state is set to $\langle n\rangle = 1.2$ which corresponds to an axial temperature of $T_{\mathrm{ax}} = 10\ \mu$K.

experimental sequence with a ramped microwave power can enhance the cooling performance.

The selectivity between the carrier and the sideband transition is also influenced by the power of the repumping lasers. As the pumping rate determines the lifetime of the states $|33, n\rangle$ it effectively broadens the linewidth of the microwave transition [26]. At pumping rates exceeding the angular oscillation frequency of the trap $\Gamma_{33} \gtrsim \omega_{\mathrm{ax}}$ off-resonant dark state depopulation induced by microwaves is significantly increased thus degrading the cooling performance. Theoretically, the dependence of the ground state population on the powers of the $|F = 3\rangle \rightarrow |F'' = 4\rangle$-laser is qualitatively similar to the plateau like shape in figure 3.4(b). The optimum repumping rate in our case is $\Gamma_{33} \approx 60\ 10^3$/s so that the effective linewidth of the microwave transition amounts to ≈10 kHz. The favorable pumping rate of the laser $|F = 4\rangle \rightarrow |F'' = 4\rangle$ theoretically is infinite. Experimentally, the optimization of the power of the two repumping lasers is limited by their polarization purity (see table 3.1).

The determination of the proper cooling parameters is not only important for the optimal cooling performance for axial motion but also minimizes heating of the radial degree of freedom: the less cooling cycles are required the less scattered repumping photons affect the radial motion. Experimentally, radial heating can be estimated by measuring the linewidth of a microwave peak. As the fit of the spectral peaks before and after sideband cooling in figure 3.6 reveals broadening caused by radial

motion (see page 58) indeed increases after cooling, but not very much. Detailed analysis is required to deduce the heating amount in particular it is important to independently measure the distribution among the axial states in the uncooled case (see section 4). Note, however, that the initially present peak asymmetry has almost disappeared in the cooled case. This could be a hint that the radial motion does not obey the Boltzmann distribution after sideband cooling. This could also provide an explanation for the unexpectedly small line widths in the high order spectra in figure 2.10 (see page 61).

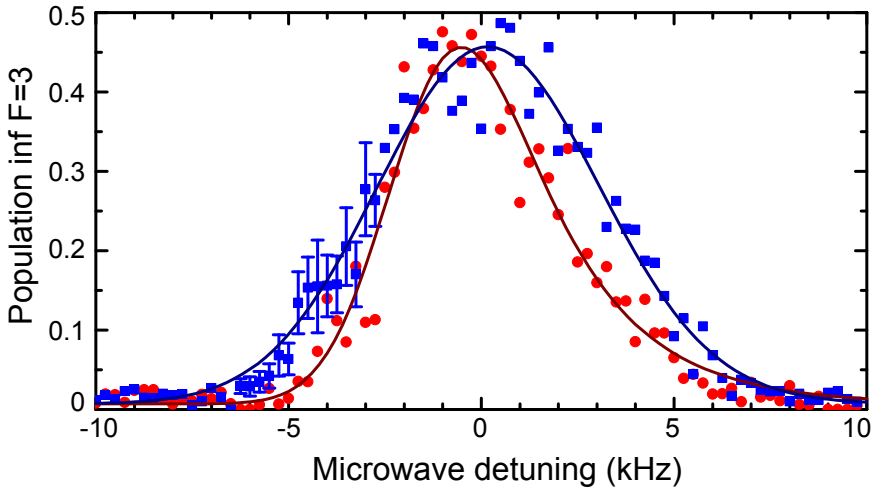

Fig. 3.6: The shape of the carrier transition peak before (•) and after (▪) sideband cooling. The Fourier-limited (full) $e^{-1/2}$ half-width of the used microwave pulse is 0.8 kHz. The lines indicate the fit using the peak function from equation 2.3.1. Before cooling the gaussian and the asymmetric width amount to $\sigma_\nu = 1.5 \pm 0.1$ kHz and $\gamma_\mathrm{b} = 2.2 \pm 0.2$ kHz, and after cooling they read $\sigma_\nu = 2.8 \pm 0.2$ kHz and $\gamma_\mathrm{b} = 0.9 \pm 0.7$ kH.

Possible extensions of the cooling scheme

Cooling with a bichromatic microwave field As figure 3.5(a) and figure 3.2 indicate an appreciable cooling takes also place when the microwave frequency is tuned to the second sideband transition. A variation of the model parameters including the lattice displacement unfortunately yield that the cooling performance in terms of ground state population is always inferior compared to cooling using the first sideband [108]. Second-sideband cooling nevertheless can be appealing for the generation of a nonclassical state where only the ground and the first excited vibrational states are populated [109].

A possible extension might be the simultaneous application of two frequencies

tuned to the first and e.g. to the second sideband, respectively [110] (see figure 3.7(a)). Experimentally this is rather simple to implement for microwave fields. The approach is motivated by expecting a higher cooling speed and by a reduced number of required photon scattering events and thus less heating of the lateral degrees of freedom. This becomes particularly important when the atomic sample needs to be cooled in all three dimensions, either via direct sideband cooling [107, 26] or via collisional coupling between orthogonal degrees of freedom [111]. Reabsorption of scattered photons by atoms already cooled to the dark ground state also imposes a limit on the minimum temperature achievable in a dense atomic cloud [26]. Possible improvements are thus conceivable when less photons are required.

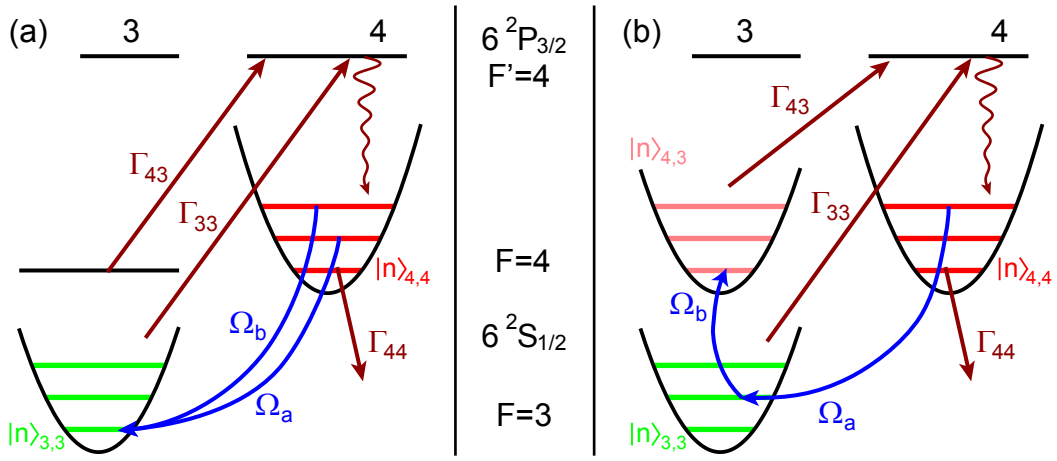

Fig. 3.7: The basic cooling scheme presented in figure 3.1 can in principle be extended by irradiating the atoms with a bichromatic microwave field characterized by the Rabi frequencies Ω_a and Ω_b.

A second extended cooling scheme shown in figure 3.7(b) has the same motivation but provides an additional advantage of a reduced projection heating. This originates from the fact that the light shift coefficients for the hyperfine state $|43\rangle$ in equation 1.2.1 have the same 1/7-relation as those for the state $|33\rangle$ but that the assignment of the circularity is opposite. The trapping potential U_{43} is thus not displaced with respect to U_{44}, they only differ in their depths as U_{43} wobbles equally to U_{33}. It thus might be possible to use even larger displacements which is favorable considering that the sideband transitions become stronger and at the same time the carrier transitions causing off-resonant excitations are attenuated.

The Hamiltonian 3.1.3 describing the atom-microwave coupling needs to be modified in order to take into account two driving fields. For this, it is instructive to follow the derivation of the time independent hamiltonian of a driven two level

system [53] (the rotating wave approximation is used in the second step)

$$\frac{1}{\hbar}H_{\text{atom+field}} = \begin{pmatrix} \omega_{44} & \Omega\cos(\omega_\text{f}\, t) \\ \Omega\cos(\omega_\text{f}\, t) & \omega_{33} \end{pmatrix} \Leftrightarrow \begin{pmatrix} 0 & \frac{\Omega}{2}\exp(-i\,\Delta\, t) \\ \frac{\Omega}{2}\exp(i\,\Delta\, t) & 0 \end{pmatrix} \Leftrightarrow \begin{pmatrix} \omega_{44} & \frac{\Omega}{2} \\ \frac{\Omega}{2} & \omega_{33}+\omega_\text{f} \end{pmatrix}. \tag{3.1.6}$$

Here, $\hbar\omega_{44/33} = E_{44/33}$ denotes the energies of the hyperfine states, Ω quantifies the coupling strength of the field oscillating at frequency ω_f and the detuning is defined by $\Delta = \omega_f - (\omega_{44} - \omega_{33})$. In the case of two fields the steps are the same until the intermediate result where the Hamiltonians for the two schemes in figure 3.7 read

scheme (a)	scheme (b)
$\begin{pmatrix} 0 & \mathcal{F}_a+\mathcal{F}_b & 0 \\ \mathcal{F}_a^\dagger+\mathcal{F}_b^\dagger & 0 & 0 \\ 0 & 0 & 0 \end{pmatrix}$	$\begin{pmatrix} 0 & \mathcal{F}_a & 0 \\ \mathcal{F}_a^\dagger & 0 & \mathcal{F}_b \\ 0 & \mathcal{F}_b^\dagger & 0 \end{pmatrix}$

and where the definition $\mathcal{F}_{a/b} = \frac{1}{2}\Omega_{a/b}\exp(-i\,\Delta_{a/b}\, t)$ is used. The Hamiltonian for scheme (b) can in principle be casted into a time independent form [53], which is also often used to describe the two photon Raman transition

$$H_{\text{scheme(b)}} = \hbar\frac{1}{2}\begin{pmatrix} 0 & \Omega_a & 0 \\ \Omega_b & 2\Delta & \Omega_b \\ 0 & \Omega_b & 2\delta \end{pmatrix}. \tag{3.1.7}$$

Such a reformulation is not possible for scheme (a) (see also [112]). The Hamiltonian thus remains explicitly time dependent and our investigation here is restricted to the direct numerical solution of the master equation.

The comparison between the usual cooling scheme and the two possible extensions is shown in figure 3.8. The parameters (Rabi frequencies, repumping rates, ...) used for the simulation are all compatible with the experimental setup and are near around optimum values for each scheme. The interesting figures of merit are the achievable cooling speed, the cooling limit and the average number of required photons which have to be scattered during the cooling process. This number is computed by

$$\text{scattered photons} = \int_{t=0}^{t_\text{max}} dt\ \left(\Gamma_{33}\sum_{n=1}^{n_\text{max}}\rho_{33,n}(t) + \Gamma_{44}\sum_{n=1}^{n_\text{max}}\rho_{43,n}(t)\right). \tag{3.1.8}$$

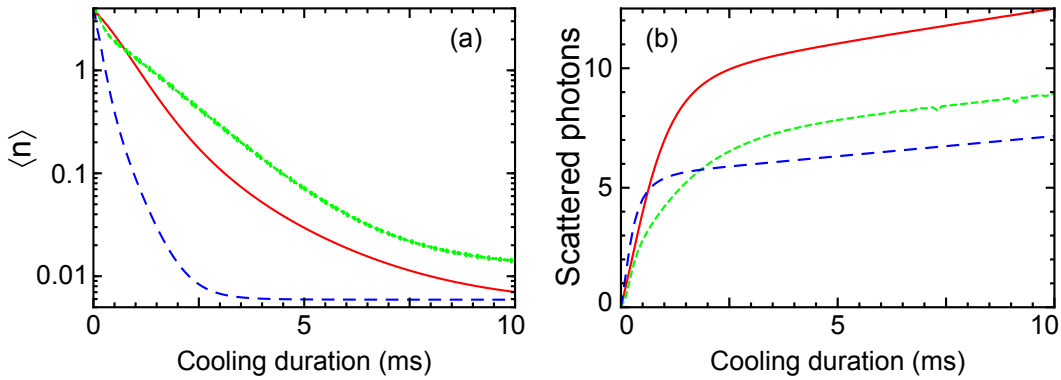

Fig. 3.8: Cooling performance for the schemes from figure figure 3.1 (solid) and figure 3.8(a/b) (small/big dashing) assuming the pure initial state $|44, 4\rangle$. Panel (a) compares the cooling speed, panel (b) shows the average number of scattered photons required during the cooling process.

It turns out, that scheme (a) is difficult to handle but that scheme (b) provides an easily achievable improvement with respect to the simple cooling scheme. The difficulty of scheme (a) arises from interference effects between the two driving fields when they become resonant with a two photon transition. Note that two of the three coupled states are not affected by repumping lasers. The population of the motional states can thus 'climb' upwards in the same way as it can 'climb' downwards (several two photon transitions, see figure 3.7(a)). In order to avoid the interferences either the repumping power must be increased or the microwave power has to be reduced or the microwave frequencies must be detuned away from the two photon resonance. All these actions, however, lead to a higher final temperature. With a good parameter choice it is though possible to decrease the required number of required repumping photons.

In contrast, the cyclic cooling scheme is preserved in scheme (b) and the concatenation of several two photon transitions is not possible. The simulation shows both, an increased cooling speed and a significantly reduced number of scattering events. Unfortunately, the scheme does not benefit from an increase of the lattice displacement. The reason for this is, that during the final cooling stage basically only the first excited motional state plays a role. This also explains the basically unchanged cooling limit.

Pulsed cooling An option to improve the cooling performance consists in pulsed operation with an interleaving succession of discreet microwave pulses and discreet repumping pulses. Experimentally, this requires the possibility to switch the repumping laser on a sub milliseconds time scale. The performance of a preliminary

experimental attempt of pulsed cooling is shown in figure 3.9. It reveals that after approximately 10 repetitions the cooling result is comparable to the continuous cooling method.

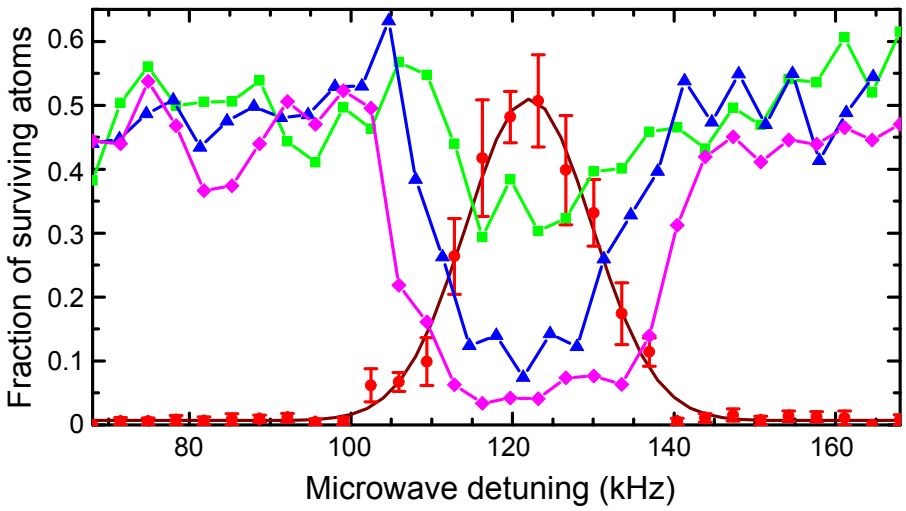

Fig. 3.9: Performance of pulsed cooling depending on the microwave frequency during the cooling process ((•) indicates the position of the blue sideband). The blue sideband is attenuated step by step with the number of cooling pulses {(■, 1 pulse), (▲, 5 pulses), (♦, 10 pulses)}. For simplicity all pulses are equal and fulfill the π-pulse condition for the $|44,1\rangle \leftrightarrow |33,0\rangle$ transition.

The benefit of the pulsed operation is that the lattice displacement can be individually adjusted for each microwave pulse and each repumping pulse. First of all, this procedure eliminates the projection heating because the repumping can take place in an unshifted lattice. Furthermore, the displacement can be optimized for a desired sideband transition. This at the same time reduces off-resonant excitation out of the dark state because the Franck-Condon factors of the carrier transitions become small for larger displacements (see figure 2.24). The method easily allows for a sequence of pulses starting from the highest ones and ending with the first sideband. Ideally, only one repumping photon will be required in order to bring the atom to the motional ground state independent of its initial state. The required lattice shifts between the cooling pulses of course imply a precise and preferably fast control of the shift. Comparison of different shift speeds during the measurement presented in figure 3.9 revealed however that even a shift within 10 μs does not introduce detectable heating (the speed is limited by our EOM driver). The reason for this is that the shift length is only a fraction of the wave function size and not several multiples of it [7].

Future applications

As discussed in section 2.4 the main limitation for precise manipulations in our experiment stems from the thermal radial motion. Our preliminary attempt to perform microwave-induced sisyphus cooling as proposed/demonstrated in [102, 103, 105] did not decrease the present atomic temperature although clear heating was observed at wrong microwave frequencies. A more fruitful approach, probably based on the proposals in [113, 114], can be tried out by implementing a state selective potential shift along the radial direction.

In general, the microwave based cooling scheme can be implemented in many existing experiments. In particular, the magic wavelength for the generation of the optical lattice is not at all a stringent prerequisite. As the required potential displacement is rather small the less pronounced vector light shift at other wavelengths is still enough to introduce spin dependency [76]. The possibility to reduce the amount of scattered photons during the cooling procedure might be exploited for cooling of large dense clouds where multiple scattering imposes a limit onto the finite temperature [26]. This in particular becomes interesting after the cloud has been distorted during fluorescence imaging where modern setups provide single site resolution [19]. The reduced number of required lasers is also appealing for experiments where optical access might be restricted [30, 31]. An interesting question is finally whether our method, exploiting a transition between state dependent potentials, can be successfully transferred to the field of micro-mechanical oscillators [100].

Chapter 4

Preparation and detection of vibrational states

Experimental control over the quantized motional state of a trapped particle allows to utilize the system for more complex applications [32, 94, 84]. The previous section was dedicated to the initialization of the atomic sample into the ground state. In this chapter I present two detection methods for the motional state which are finally employed for the verification of deliberately prepared states.

4.1 Beating of Rabi-oscillations

Let us assume that the motional state to be measured is stored in the lower hyperfine state so that its density matrix representation reads

$$\rho = \sum_{n=0}^{n_{\max}} P_{33,n} |33, n\rangle\langle 33, n| + \text{coherence terms.} \tag{4.1.1}$$

In the more general case for which the motional state and the spin state of an atomic ensemble have both to be determined the population of one of the spin states can be shelved in a third auxiliary state (e.g. $|33\rangle \rightarrow |43\rangle$) prior to the detection. In experiments with small numbers of atoms, which are mostly trapped ion experiments, a standard technique to measure the population of the quantized motional states of the ion is based on recording Rabi flopping traces between internal states (in our case the hyperfine states $|44\rangle$ and $|33\rangle$) [37, 95, 89]. It exploits the fact that all first order sideband transitions (in our case $|33, n\rangle \leftrightarrow |44, n+1\rangle$) possess a different Rabi frequency $\Omega_{n,n+1}$. For a harmonic trapping potential in the Lamb-

Dicke regime $\eta \ll 1$ e.g., the Rabi frequencies scale as $\Omega_{n,n+1} = \sqrt{n}\,\Omega_{0,1}$ (see page 30). When off-resonant excitation can be neglected the subspaces $\{|33,n\rangle,\ |44,n+1\rangle$ are decoupled during the spin-flip operation. The recorded Rabi flopping trace is thus a simple superposition of several sinusoidal signals. The population of the state $|33,n\rangle$ leads to a contribution at frequency $\Omega_{n,n+1}$ and has an amplitude which is equal to its occupation probability $P_{33,n}$. The time dependent population of the auxiliary hyperfine state $|44\rangle$ is thus given by

$$P_{44}(t) = \frac{1}{2}\left(1 - \sum_{n=0}^{n_{\max}} P_{33,n}\,\cos(\Omega_{n,n+1}\,t)\exp(-t/\tau_{n,n+1})\right). \tag{4.1.2}$$

Here, we consider an individual decay constant $\tau_{n,n+1}$ for each transition [37, 68, 115].

The method of beating Rabi oscillations is directly applicable using our microwave sideband technique. In our case, at a fixed displacement the sideband transitions of any order possess well defined relative strengths and thus Rabi frequencies. The measurement of Rabi frequencies for initially pure motional states (Fock state) is exemplarily shown in figures 2.21 and 2.24. For a thermal distribution over the vibrational states which results from simple molasses cooling the Rabi flopping measurement in displaced potentials shown in figure 4.1(a) shows a clear signature of beating. The occurrence of few discrete frequencies is confirmed by the discrete Fourier transform of the trace shown in panel (b). A so-called Kaiser window was applied to the Rabi trace before the Fourier Transform in order to avoid that the side lobs of large peaks obscure the smaller neighboring peaks.

For this measurement the full microwave power ($\Omega_{\text{bare}} = 2\pi\,59\,\text{kHz}$) was used in order to record many oscillation cycles within the decoherence time. On the other hand, the polarization angle of $\vartheta = 6°$ already corresponds to an η-parameter of 0.33 and dressing of the observed carrier transitions due to the relatively strong first order sidebands must be considered. This firstly causes a shift of the expected Fourier peaks by approximately 1.5 kHz with respect to their positions expected from the bare Franck-Condon factors. A simulation of the experiment using the model described in section 2.2.2 confirms this shift (see dashed line in figure 4.1(b)). What is more important here, is that according to the simulation, off-resonant excitations also reduce the heights of the relevant peaks by approximately 10%. This implies that the expected sum of all peak heights is only 0.9. The sum of the three experimentally visible peak heights yields 0.48. The large discrepancy is mainly due to the decay of the observed oscillations which is not considered in the theory.

The decay can be considered by fitting the Rabi trace using the function equivalent to that in equation 4.1.2. Only the lowest three motional states are taken into account ($n_{\max}$=3) as according to the Fourier transform all other contributions are

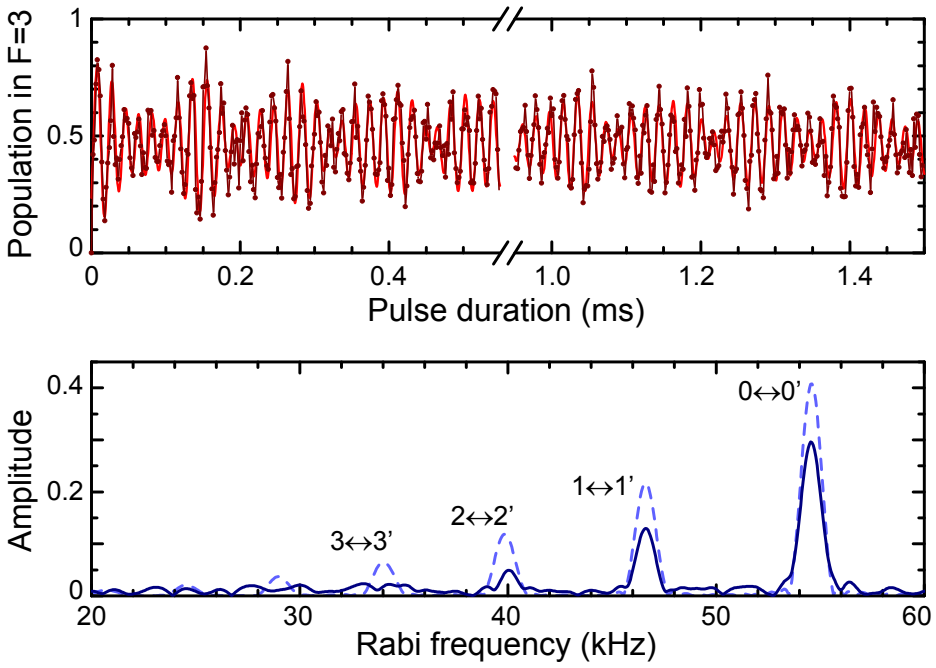

Fig. 4.1: (a) Rabi flopping measurement on the carrier transition of a thermal ensemble when the polarization angle amounts to $\vartheta = 6.0°$ (η=0.33) and (b) the corresponding discrete fourier transform (solid line). A Fourier amplitude of 1 corresponds to an ideal Rabi oscillation with full population transfer and without decay. The line underneath the data in (a) is a fit of the Rabi flopping trace and the dashed line in (b) indicates the Fourier peaks of a theoretically calculated Rabi trace assuming a temperature of 10 μK.

buried in the background. Alternatively, the damping term in the fitting function is replaced by $\exp(-\sqrt{t/\tau_{\mathrm{decay}}})$. It was found to give better fitting results for the Rabi oscillations measured in our experiment as outlined in figure 2.21. Table 4.1 summarizes the determined parameters of the Rabi trace. According to the analysis of decoherence sources in section 2.4 carrier transitions between higher motional states are less susceptible to broadening. They are instead strongly affected by the fluctuation of the Franck-Condon factor either caused by the radial motion or by the fluctuation of the lattice displacement. This, most likely, causes the observed increase of the damping with the quantum number n.

When the decay of the Rabi signal is taken into account the sum of the amplitudes of the three visible peaks amounts to 0.6 and 0.68 for the two alternative damping terms, respectively. These values reasonably agree with the sum of the three largest theoretically expected amplitudes which amounts to 0.75.

Assuming a thermal distribution a temperature T_{ax} for the axial degree of free-

	Fourier	$\exp(-t/\tau_{n,n})$		$\exp(-\sqrt{t/\tau_{n,n}})$	
$n \leftrightarrow n'$	$H_{44,n}$	$P_{44,n}$	$\tau_{n,n}$	$P_{44,n}$	$\tau_{n,n}$
$0 \leftrightarrow 0'$	0.30	0.34±0.02	4.5±0.6	0.37±0.02	10±3
$1 \leftrightarrow 1'$	0.13	0.17±0.03	3.0±1	0.18±0.03	5±3
$2 \leftrightarrow 2'$	0.05	0.09±0.03	1.8±1	0.13±0.03	1.0±0.7
T_{ax}	$7\,\mu$K	$(8\pm1)\,\mu$K		$(9pm1)\,\mu$K	

Tab. 4.1: Comparison between the heights of the Fourier peaks in figure 4.1 and the fitting parameters of the Rabi trace using two different damping terms. The damping constant for the transition $|44,0\rangle \leftrightarrow |33,0\rangle$ was determined independently using a ground state cooled sample. The temperature of the atomic ensemble is deduced from the relative amplitudes.

dom can be determined by comparing the ratios between the measured amplitudes with the theoretical expectation (see table 4.1). As the Fourier transform method does not consider the damping it underestimates the actual temperature. The temperature estimated by the fitting method provides a more reliable value and the results of the two fitting functions agree with each other within the error-bars. They also are consistent with the value of $10\,\mu$K obtained by atom loss detecting at variable trap depths [51].

The presented measurement is a proof of principle, which reveals the feasibility of the Rabi-beating technique. High accuracy in particular requires an independent measurement of damping envelopes of each individual transition. In principle, the tunability of the Franck-Condon factors inspires to extend the method. High order sidebands can, e.g., be used to 'hide' the population of several highly populated ground states in order to be able to detect small signals originating from weakly populated states. Or, a clever choice of the displacement which maximizes the Franck-Condon factor for a desired transition makes this transition less sensitive to decoherence sources (see figure 2.19). Combining several such partly optimized measurements could provide a more accurate picture of the motional state population.

4.1.1 Height of sideband peaks

Instead of measuring Rabi flopping traces at a fixed sideband transition the population of the vibrational states can be mapped by recording a spectrum with many sidebands using a fixed pulse duration. An exemplary spectrum for a thermal ensemble is shown in figure 4.2.

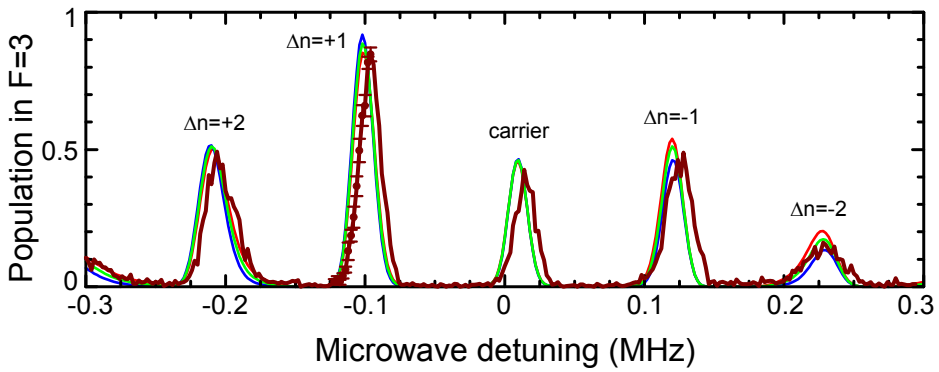

Fig. 4.2: A measurement of many sideband peaks provides information about the population of the vibrational states ($\vartheta = 10.5°$ and $\eta = 0.58$). The data are consistent with an axial temperature of $T_{\mathrm{ax}} = 10 \pm 2$ μK as is confirmed by three calculated spectra with $T_{\mathrm{ax}} = \{8, 10, 12\}$ μK, respectively (the radial motion is not considered here).

For comparison, the same figure shows calculated spectra which result from an average over a thermal population distribution. Note that the peak asymmetry stems from the anharmonicity of the sinusoidal trap and not from the radial motion. A measurement of the same spectrum but with a ground state cooled sample confirmed that broadening due to radial motion is small (see page 61), so it is ignored here.

The measured spectrum is again consistent with an axial temperature of $T_{\mathrm{ax}} = 10$ μK. The theoretical results, however, show a relatively small sensitivity of the spectrum with respect to a temperature change. This can be slightly improved by choosing an optimal displacement and optimal parameters for the microwave pulse. Despite that, in general, the spectrum method is inferior to the Rabi flopping method as it contains a lot of redundant information. Basically, one point on top of each peak would be enough to provide the same discrimination between different temperatures. The better strategy is thus to record the peak heights of several peaks at different pulse times, which is equivalent to the Rabi method.

4.2 Push-out technique for the vibronic state

A detection procedure which requires less demanding coherence properties compared to the previous ones can be implemented by extending our state selective push-out detection for the hyperfine state (see page 8). The scheme is based on the alternating application of microwave pulses and push-out pulses as illustrated in figure 4.3.

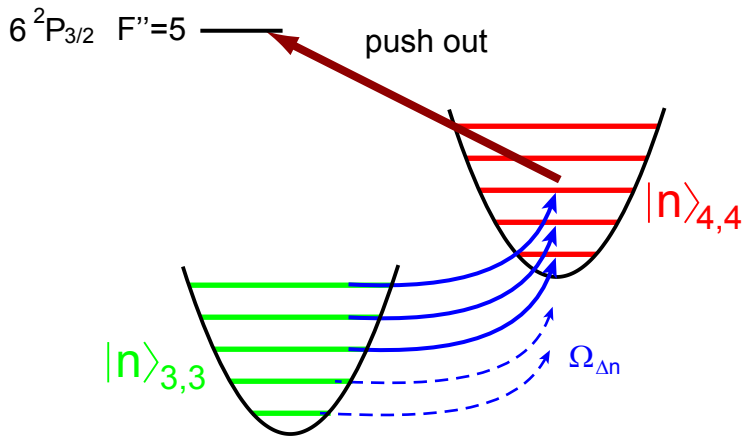

Fig. 4.3: The push-out technique selective to the vibrational state. Microwave pulses transfer the population of selected motional states to the upper hyperfine state $|44\rangle$. A subsequent laser pulse resonant with the $F = 4 \rightarrow F'' = 5$ transition removes all atoms in this state. After several repetitions all states $|33, n\rangle$ resonant with the microwave pulses are depleted.

The starting condition is again the motional state defined by equeation 4.1.1. The procedure begins with a microwave pulse tuned to the red sideband transition $|33, n\rangle \leftrightarrow |44, n - \Delta n\rangle$ transferring a fraction of atoms to the upper hyperfine state. But, it for sure does not change the population of the vibrational states with $n < \Delta n$. Subsequently, the push-out laser removes all atoms which have been transferred. After one iteration the vibrational states with $n \geq \Delta n$ are depleted by an amount determined by the Rabi frequencies $\Omega_{n,n-\Delta n}$ and by the pulse duration. In general however, none of these states is now completely empty. This can be accomplished by iterating the sequence until the population of the affected states is below a predefined threshold.

For a reliable performance the application of multiple push-out pulses must preserve both the total population of the hyperfine state $|33\rangle$ and its distribution among the vibrational states $P_{33,n}$. The adherence of these conditions is tested using motional Fock states as presented in figure 4.4. The Fock state $|33, n\rangle$ is prepared using a single gaussian pulse tuned to the n^{th} order blue sideband. Subsequently, the prepared state is probed by scanning the microwave frequency during the push-out process with 10 repetitions. The microwave pulses again possess a gaussian shape in order to ensure selectivity between different sideband transitions. The time required for the entire detection sequence amounts to 3.4 ms ($10\times$(100 μs for the microwave pulse + 150 μs for the push-out pulse + 90 μs delay)).

The demonstration of our detection technique using Fock states reveals 100% loss of atoms when the microwave pulses are resonant with a sideband transition

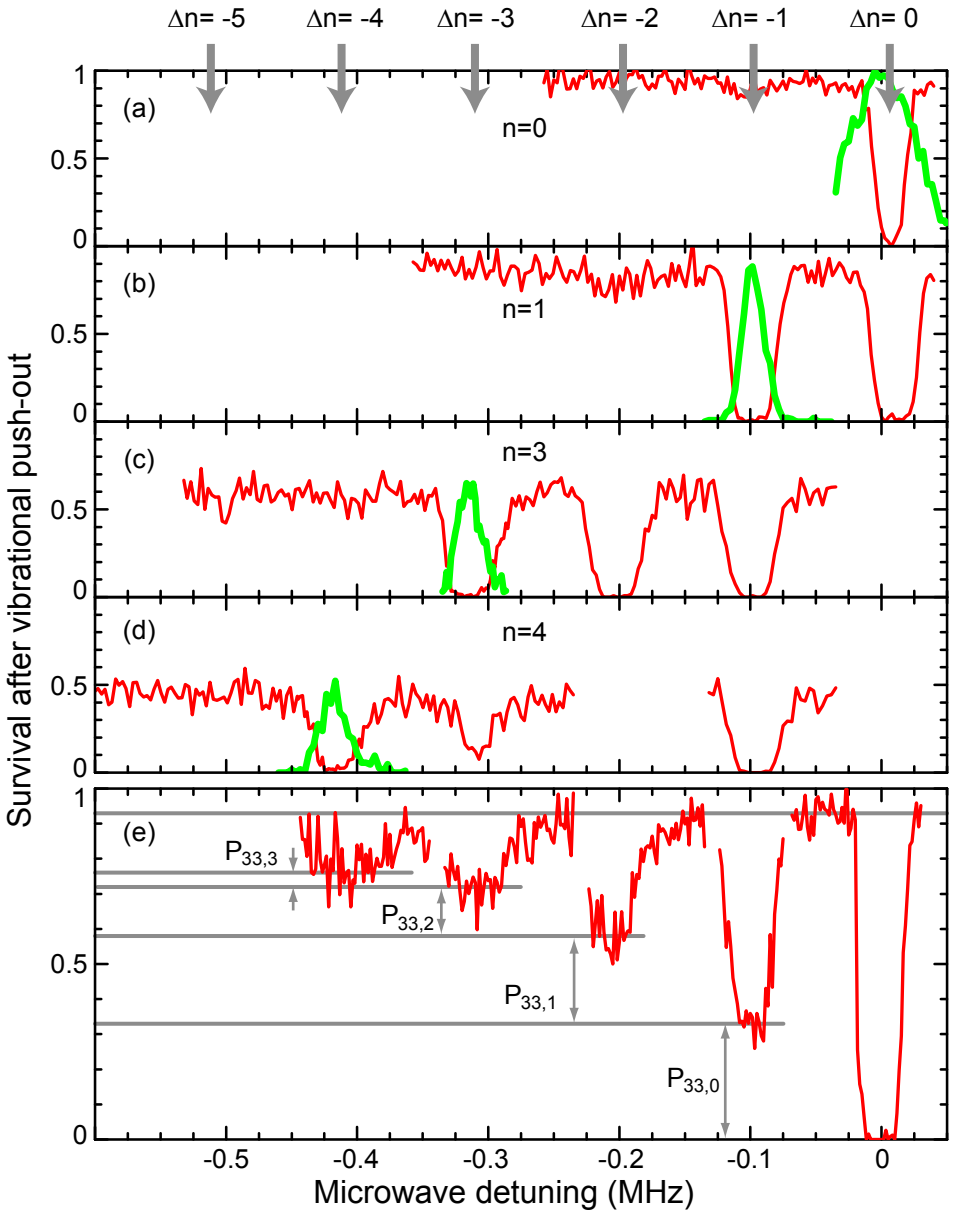

Fig. 4.4: (a-d) Push-out technique discriminating between motional states applied to an ensemble prepared in a vibrational Fock state with n={0, 1, 3, 4}, and (e) to a thermal distribution. The height of the peak shown in each panel (thick green line) determines the preparation efficiency of the Fock states. The thin red line indicates atomic loss depending on the microwave frequency during the push-out process.

satisfying $\Delta n \leq n$. On the other hand only little additive loss with respect to the preparation efficiency is observed when non of the sidebands is resonant, or, when the order of the sideband is larger than the motional quantum number $\Delta n > n$. In detail, a loss of (2±2)% is caused by the simple application of a 10 fold push-out. This is compatible to the relaxation time scale of the hyperfine state (100 ms). In order to quantify the push-out-induced heating and residual off-resonant excitation caused by the microwave pulses, we prepare a $|33, n = 0\rangle$ Fock state. An application of a 10 fold detection sequence including the first order sideband transition reveals a loss of (5±2)%. Taking into account a small impurity of the initial Fock state (3% of atoms in the state $|33, n = 1\rangle$) the observed loss is consistent with that caused by the push-out alone. Heating-induced by the detection procedure can thus be neglected at the level of the presented measurement statistics.

In principle, for any choice of Δn and for each microwave/push-out combination both the displacement and the duration of the microwave pulse can be adjusted separately. These parameters can be optimized by e.g. maximizing the depletion of the affected states after each iteration. In particular, displacements leading to a vanishing Franck-Condon factor must be avoided (see figure 2.24). For simplicity, in the presented measurement the same parameters have been used for all 10 pulses of the detection sequence. They have only been varied for different sideband orders Δn (note that the uncomplete removal of atoms for $\Delta n = -3$ in case of the Fock state n=4). This is the reason for the piecewise acquisition of the data presented in figure 4.4.

The result of the described method is an atomic sample for which all vibrational states with $n \geq k$ are empty. The method can however be easily extended to a projective filter for a single motional Fock state. One such approach is based on the application of microwave pulses which satisfy the 2π-pulse condition for the dedicated state [116, 39]. Our setup in principle allows two further approaches. The first one is based on the population transfer of the dedicated state to the motional ground state with a single microwave pulse. The procedure described above can then be used to deplete all states except for the ground state. The second option is based on the choice of a lattice displacement with a vanishing Franck-Condon factor for the dedicated state which is effectively equivalent to the 2π-pulse procedure (see also the preparation of a superposition state below). One future application of this method, which requires a projective filter for motional states, might be the verification of the quantum-thermodynacal Jarzynski equality using [38, 39].

4.2.1 Preparation of vibrational states

There exist several special vibrational states, such as the thermal, the coherent, the Fock and the squeezed states, which have been extensively studied due to their

special properties [37]. Using a step by step construction it is even possible to engineer a desired motional state [84, 96]. Here, we exemplarily investigate the population distribution of a thermal, a coherent and a Fock-state superposition state.

Figure 4.4(e) shows the 'depletion' spectrum for a not ground state cooled ensemble. It reveals the cumulative atom loss depending on the order of the sideband. The plateau like bottom level of each peak is used to define the fraction of the residual atoms. According to the statistics of the data the confidence interval for the plateau level is estimated to be ±2%. The difference between two consecutive plateaus determines the corresponding population of the individual Fock states. The histogram for the deduced probability distribution is shown in figure 4.5. For comparison, it shows the theoretical distributions of a thermal state and of a coherent state. The measurement reasonably agrees with an axial temperature of $T_{\mathrm{ax}} = 12\ \mu\mathrm{K}$.

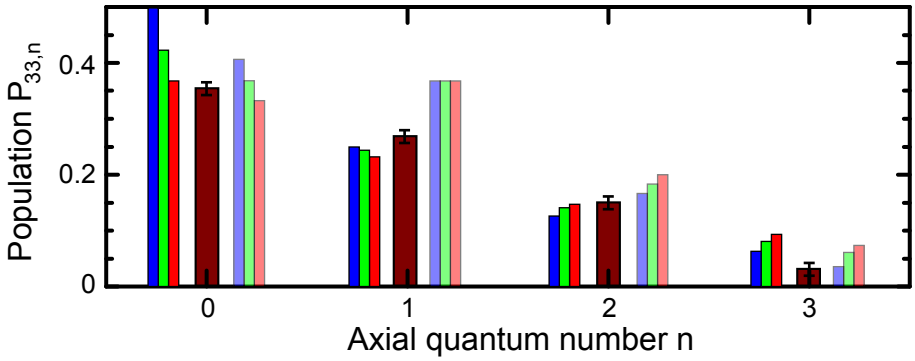

Fig. 4.5: The occupation probability of the vibrational Fock states deduced from the measurement in figure 4.4(e) (central bars). The bars on the left indicate the theoretical distribution of a thermal state with $T_{\mathrm{ax}} = 10 \pm 2\ \mu\mathrm{K}$) and that on the right the distribution for a coherent state with $\langle n \rangle = 1 \pm 0.1$.

The measurement with a thermal state also demonstrates the limitations of the push-out detection scheme. Due to the trap anharmonicity of the sinusoidal potential and due to the different trap depths of the potentials U_{44} and U_{33} in case of a displaced lattice sideband transitions of the same order do *not* have the same resonance frequency (see page 56). This broadening degrades the selectivity between adjacent sideband transitions. The radial motion is an additional broadening source in our setup (see page 58).

Finally, figure 4.6 presents the population measurement of a coherent motional state and a superposition between two Fock states. The coherent state is generated by projecting the initial state $|33, 0\rangle$ onto the states $|44, n\rangle$ by applying an optical pumping pulse while the lattice is displaced by a variable amount. Using

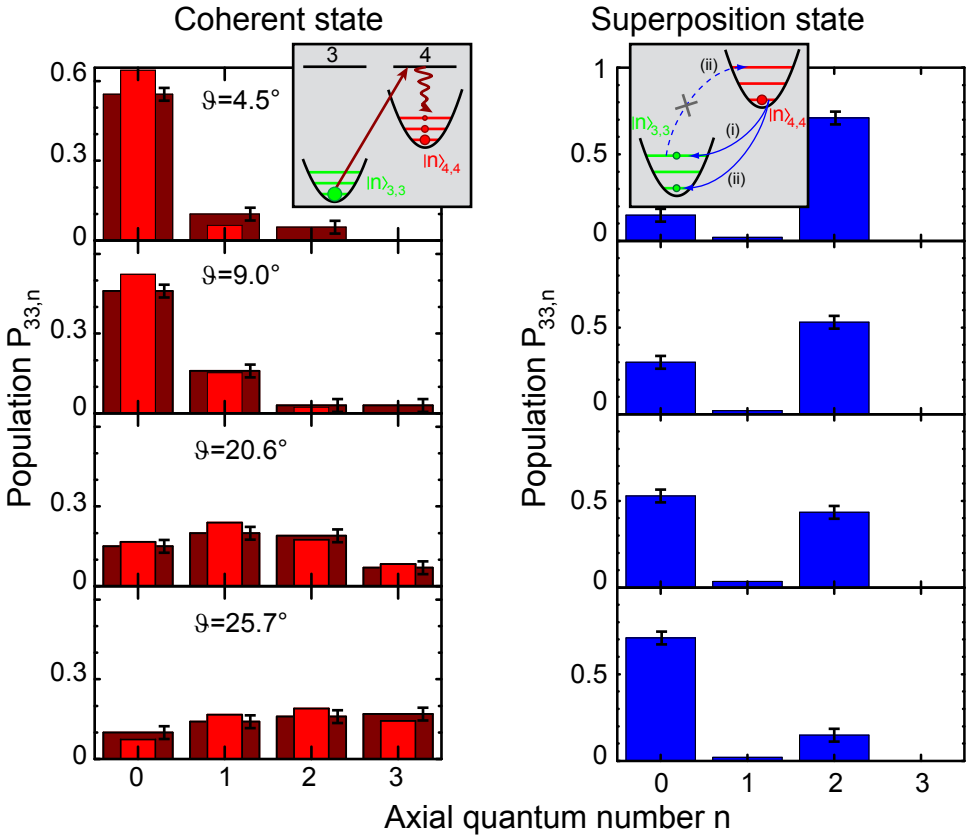

Fig. 4.6: (left) the population distribution of a coherent state with a variable oscillation amplitude (dark red) compared with the theoretical expectation (red, see text). (right) the verification of a superposition between the motional Fock states $|33,0\rangle$ and $|33,2\rangle$ with an adjustable ratio between the populations.

the 'repumper' laser resonant with the $F = 3 \rightarrow F'' = 4$ transition (see figure 1.2) indeed corresponds to a projection among motional states because the duration of the optical transition is negligible with respect to the axial oscillation period. According to the branching ratio of the optically excited state only 80% of the atoms are expected to be transferred to the $|44\rangle$ hyperfine state. The observed fraction of 70% agrees with this expectation taking into account the imperfect preparation of the initial state and atom losses during the detection procedure. The measurement, in particular, quantifies the projection heating present in our cooling scheme (see figure 3.4) and agrees with the theoretical expectation.

The superposition state between two Fock states shown in figure 4.6 is prepared using two subsequent microwave pulses. The first pulse is resonant to the second

red sideband $|44,0,\rangle \leftrightarrow |33,2\rangle$ and generates the state

$$\psi = c_{44,0}|44,0\rangle + c_{33,2}|33,2\rangle$$

with variable coefficients $c_{44,0}$ and $c_{33,2}$. The second pulse is tuned to the carrier transition and maps the population $|c_{44,0}|^2$ onto the state $|33,0\rangle$. For the second pulse the proper choice of the lattice displacement ensures that the Franc-Condon factor for the carrier transition $|33,2\rangle \leftrightarrow |44,2\rangle$ vanishes (compare to figure 2.24). In principle the entire procedure only includes coherent operations. This is thus the first step towards the employment of the vibrational state as the physical carrier for a qubit (see section 5.1) or the preparation of arbitrary motional states [96]. Due to the long duration of the pulse sequence (400 μs) used compared to the coherence time (150 μs [23]), though, the phase information is lost in the presented measurement.

Chapter 5

Outlook

The control over the motional state, in particular the preparation of the ground state, is a large step towards the investigation of atom-atom interactions [14]. For this, the experimental setup is currently upgraded in order to perform 3D ground state cooling. As outlined on page 74 the manipulation of the motional state itself also provides a rich variety of further applications. Here, I briefly outline a scheme for atom-atom entanglement which employs the techniques presented in this work.

5.1 Motional qubit state

The possibility to prepare the atomic wave function in a superposition of two vibrational Fock states (see figure 4.6) opens the way towards the exploitation of the motional degree of freedom as the physical carrier of a qubit [35]. This system is appealing because the qubit is not sensitive to fluctuations of external fields as it is encoded in the same atomic hyperfine state [36]. It, though, is still sensitive to fluctuations of the trapping potential and, in our case, to the thermal motion of the radial degree of freedom. 3D ground state cooling thus remains essential for high fidelity operations but this is also true for other systems (e.g. [27, 28]).

As outlined in figure 5.1 our experimental setup provides the tools for the realization of entanglement between two qubits encoded in the vibrational states of two or more atoms. For demonstration, let us assume that initially two atoms are located in neighboring wells of the optical lattice (the scheme presented in [117] can be readily used to rearrange the atoms until they fulfill this condition). Both atoms are prepared in the motional ground state but possess opposite spin orientation $|44, 0\rangle$ / $|33, 0\rangle$, respectively (see e.g. [17]). A tri-chromatic microwave field is used to flip the spin of both atoms and at the same time to prepare a vibrational superposition state. Thereby, the relative population of the motional states

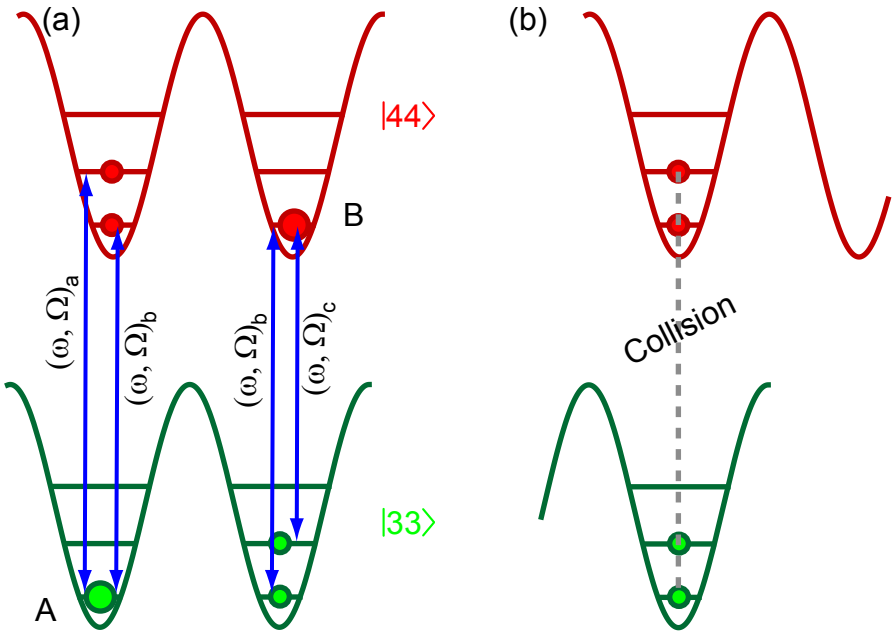

Fig. 5.1: (a) Two atoms A and B each prepared in a superposition between two motional Fock states. (b) The two atoms are merged using the spin dependent transport. Entanglement of the motional states of two atoms is generated via collisional interaction because the collisional phase depends on the motional state.

is defined by the Rabi frequencies of each field component (as field b is common for both qubits the relative population of both qubits will be identical when both spins are completely flipped). A arbitrary superposition state can alternatively be prepared using a pulse sequence (see figure 4.6). Employing the state dependent transport both atoms are subsequently shifted towards each other by merging the corresponding potential wells. Due to collisional interaction [12] which depends on the wave function overlap between the two atoms the phase accumulation for the two vibrational states is different. After the atoms are separated again their qubit states encoded in their motional are entangled.

The detection of the collisional phase can again be performed by the tri-chromatic microwave pulse. Here, the spin rotation of atom A (B) depends on its phase with respect to the phase of the beating signal between the fields a and b (b and c). The probability to find atom A and B in their initial states $|33\rangle$ and $|44\rangle$ after the second microwave pulse, respectively, will thus exhibit a variable correlation depending on the acquired collisional phase.

Bibliography

[1] Immanuel Bloch, Jean Dalibard, and Wilhelm Zwerger. Many-body physics with ultracold gases. *Reviews of Modern Physics*, 80(3):885, July 2008. (document)

[2] Michael A. Nielsen and Isaac L. Chuang. *Quantum Computation and Quantum Information*. Cambridge University Press, October 2000. (document)

[3] Immanuel Bloch. Ultracold quantum gases in optical lattices. *Nat Phys*, 1(1):23–30, October 2005. (document)

[4] Immanuel Bloch. Quantum coherence and entanglement with ultracold atoms in optical lattices. *Nature*, 453(7198):1016–1022, June 2008. (document)

[5] Worawarong Rakreungdet, Jae Hoon Lee, Kim Fook Lee, Brian E. Mischuck, Enrique Montano, and Poul S. Jessen. Accurate microwave control and real-time diagnostics of neutral-atom qubits. *Physical Review A*, 79(2):022316, February 2009. (document), 2.5.1

[6] S. Kuhr, W. Alt, D. Schrader, I. Dotsenko, Y. Miroshnychenko, W. Rosenfeld, M. Khudaverdyan, V. Gomer, A. Rauschenbeutel, and D. Meschede. Coherence properties and quantum state transportation in an optical conveyor belt. *Physical Review Letters*, 91(21):213002, November 2003. (document), 1.1

[7] Olaf Mandel, Markus Greiner, Artur Widera, Tim Rom, Theodor W. Hänsch, and Immanuel Bloch. Coherent transport of neutral atoms in Spin-Dependent optical lattice potentials. *Physical Review Letters*, 91(1):010407, July 2003. (document), 1.2.2, 3.1.2

[8] Michal Karski, Leonid Förster, Jai-Min Choi, Andreas Steffen, Wolfgang Alt, Dieter Meschede, and Artur Widera. Quantum walk in position space with single optically trapped atoms. *Science*, 325(5937):174–177, July 2009. (document), 2.2.1, 2.4

[9] S. E. Hamann, D. L. Haycock, G. Klose, P. H. Pax, I. H. Deutsch, and P. S. Jessen. Resolved-sideband raman cooling to the ground state of an optical lattice. *Physical Review Letters*, 80(19):4149, May 1998. (document), 2, 2.1.1, 3, 3.1.1, 3.1.2

[10] Markus Greiner, Olaf Mandel, Tilman Esslinger, Theodor W. Hansch, and Immanuel Bloch. Quantum phase transition from a superfluid to a mott insulator in a gas of ultracold atoms. *Nature*, 415(6867):39–44, 2002. (document)

[11] Gavin K. Brennen, Carlton M. Caves, Poul S. Jessen, and Ivan H. Deutsch. Quantum logic gates in optical lattices. *Physical Review Letters*, 82(5):1060, February 1999. (document)

[12] D. Jaksch, H.-J. Briegel, J. I. Cirac, C. W. Gardiner, and P. Zoller. Entanglement of atoms via cold controlled collisions. *Physical Review Letters*, 82(9):1975, March 1999. (document), 5.1

[13] Anders Sørensen and Klaus Mølmer. Spin-Spin interaction and spin squeezing in an optical lattice. *Physical Review Letters*, 83(11):2274, 1999. (document)

[14] Olaf Mandel, Markus Greiner, Artur Widera, Tim Rom, Theodor W. Hansch, and Immanuel Bloch. Controlled collisions for multi-particle entanglement of optically trapped atoms. *Nature*, 425(6961):937–940, October 2003. (document), 5

[15] David Hayes, Paul S. Julienne, and Ivan H. Deutsch. Quantum logic via the exchange blockade in ultracold collisions. *Physical Review Letters*, 98(7):070501–4, February 2007. (document)

[16] Marco Anderlini, Patricia J. Lee, Benjamin L. Brown, Jennifer Sebby-Strabley, William D. Phillips, and J. V. Porto. Controlled exchange interaction between pairs of neutral atoms in an optical lattice. *Nature*, 448(7152):452–456, July 2007. (document)

[17] D. Schrader, I. Dotsenko, M. Khudaverdyan, Y. Miroshnychenko, A. Rauschenbeutel, and D. Meschede. Neutral atom quantum register. *Physical Review Letters*, 93(15):150501, October 2004. (document), 5.1

[18] P. J. Lee, M. Anderlini, B. L. Brown, J. Sebby-Strabley, W. D. Phillips, and J. V. Porto. Sublattice addressing and Spin-Dependent motion of atoms in a Double-Well lattice. *Physical Review Letters*, 99(2):020402–4, July 2007. (document)

[19] Waseem S. Bakr, Jonathon I. Gillen, Amy Peng, Simon Folling, and Markus Greiner. A quantum gas microscope for detecting single atoms in a hubbard-regime optical lattice. *Nature*, 462(7269):74–77, November 2009. (document), 3.1.2

[20] M. Karski, L. Förster, J. M. Choi, W. Alt, A. Widera, and D. Meschede. Nearest-Neighbor detection of atoms in a 1D optical lattice by fluorescence imaging. *Physical Review Letters*, 102(5):053001–4, February 2009. (document), 1.1

[21] Michał Karski, Leonid Förster, Jai-Min Choi, Andreas Steffen, Noomen Belmechri, Wolfgang Alt, Dieter Meschede, and Artur Widera. Imprinting patterns of neutral atoms in an optical lattice using magnetic resonance techniques. *New Journal of Physics*, (in preparation), 2010. (document), 1.1

[22] J. Kempe. Quantum random walks: an introductory overview. *Contemporary Physics*, 44(4):307, 2003. (document), 2.2.1

[23] Michał Karski. *State sellective transport of single neutral atoms*. PhD thesis, Universität Bonn, 2010. (document), 1.1, 1.1, 1.1, 1.1.2, 1.2.2, 1.2.2, 2.4, 2.4, 4.2.1

[24] D. Leibfried, R. Blatt, C. Monroe, and D. Wineland. Quantum dynamics of single trapped ions. *Reviews of Modern Physics*, 75(1):281, March 2003. (document), 2, 3, 3.1.2

[25] H. Perrin, A. Kuhn, I. Bouchoule, and C. Salomon. Sideband cooling of neutral atoms in a far-detuned optical lattice. *EPL (Europhysics Letters)*, 42(4):395–400, 1998. (document), 3, 3.1.1

[26] Andrew J. Kerman, Vladan Vuleti, Cheng Chin, and Steven Chu. Beyond optical molasses: 3D raman sideband cooling of atomic cesium to high Phase-Space density. *Physical Review Letters*, 84(3):439, 2000. (document), 3, 3.1.1, 3.1.2, 3.1.2, 3.1.2

[27] D. Leibfried, E. Knill, S. Seidelin, J. Britton, R. B. Blakestad, J. Chiaverini, D. B. Hume, W. M. Itano, J. D. Jost, C. Langer, R. Ozeri, R. Reichle, and D. J. Wineland. Creation of a six-atom 'schrödinger cat' state. *Nature*, 438(7068):639–642, December 2005. (document), 2, 5.1

[28] H. Haffner, W. Hansel, C. F. Roos, J. Benhelm, D. Chek al kar, M. Chwalla, T. Korber, U. D. Rapol, M. Riebe, P. O. Schmidt, C. Becher, O. Guhne, W. Dur, and R. Blatt. Scalable multiparticle entanglement of trapped ions. *Nature*, 438(7068):643–646, December 2005. (document), 2, 5.1

[29] Leonid Förster, Michal Karski, Jai-Min Choi, Andreas Steffen, Wolfgang Alt, Dieter Meschede, Artur Widera, Enrique Montano, Jae Hoon Lee, Worawarong Rakreungdet, and Poul S. Jessen. Microwave control of atomic motion in optical lattices. *Physical Review Letters*, 103(23):233001–4, December 2009. (document), 2.5.2

[30] G. Sague, A. Baade, and A. Rauschenbeutel. Blue-detuned evanescent field surface traps for neutral atoms based on mode interference in ultrathin optical fibres. *New Journal of Physics*, 10(11):113008, 2008. (document), 3.1.2

[31] E. Vetsch, D. Reitz, G. Sagu, R. Schmidt, S. T Dawkins, and A. Rauschenbeutel. Optical interface created by laser-cooled atoms trapped in the evanescent field surrounding an optical nanofiber. *0912.1179*, December 2009. (document), 3.1.2

[32] W. Vogel and R. L. de Matos Filho. Nonlinear Jaynes-Cummings dynamics of a trapped ion. *Physical Review A*, 52(5):4214, November 1995. (document), 2.1.1, 2.5.2, 4

[33] A. B. Deb, G. Smirne, R. M. Godun, and C. J. Foot. A method of state-selective transfer of atoms between microtraps based on the FranckCondon principle. *Journal of Physics B: Atomic, Molecular and Optical Physics*, 40(21):4131–4142, 2007. (document), 2.5.2

[34] Brian Mischuck, Ivan H. Deutsch, and Poul S. Jessen. Coherent control of atomic transport in spinor optical lattices. *Physical Review A*, 81(2):023403, February 2010. (document), 2.5.2

[35] K. Eckert, J. Mompart, X. X. Yi, J. Schliemann, D. Bru, G. Birkl, and M. Lewenstein. Quantum computing in optical microtraps based on the motional states of neutral atoms. *Physical Review A*, 66(4):042317, October 2002. (document), 5.1

[36] N. Lundblad, J. M. Obrecht, I. B. Spielman, and J. V. Porto. Field-sensitive addressing and control of field-insensitive neutral-atom qubits. *Nat Phys*, 5(8):575–580, 2009. (document), 5.1

[37] D. M. Meekhof, C. Monroe, B. E. King, W. M. Itano, and D. J. Wineland. Generation of nonclassical motional states of a trapped atom. *Physical Review Letters*, 76(11):1796, March 1996. (document), 2, 2.1.1, 2.5.2, 4.1, 4.1, 4.2.1

[38] C. Jarzynski. Nonequilibrium equality for free energy differences. *Physical Review Letters*, 78(14):2690, April 1997. (document), 4.2

[39] Gerhard Huber, Ferdinand Schmidt-Kaler, Sebastian Deffner, and Eric Lutz. Employing trapped cold ions to verify the quantum jarzynski equality. *Physical Review Letters*, 101(7):070403, 2008. (document), 4.2

[40] Harold J. Metcalf and Peter van der Straten. *Laser Cooling and Trapping*. Springer, 1 edition, September 1999. 1.1, 3

[41] E. L. Raab, M. Prentiss, Alex Cable, Steven Chu, and D. E. Pritchard. Trapping of neutral sodium atoms with radiation pressure. *Physical Review Letters*, 59(23):2631, December 1987. 1.1

[42] L. Ricci, M. Weidemller, T. Esslinger, A. Hemmerich, C. Zimmermann, V. Vuletic, W. Knig, and T. W. Hnsch. A compact grating-stabilized diode laser system for atomic physics. *Optics Communications*, 117(5-6):541–549, June 1995. 1.1

[43] Wolfgang Alt. *Optical control of single neutral atoms*. PhD thesis, Universität Bonn, 2004. Available online at http://hss.ulb.uni-bonn.de/diss_online/. 1.1, 2.4

[44] C. P. Pearman, C. S. Adams, S. G. Cox, P. F. Griffin, D. A. Smith, and I. G. Hughes. Polarization spectroscopy of a closed atomic transition: applications to laser frequency locking. *Journal of Physics B: Atomic, Molecular and Optical Physics*, 35(24):5141–5151, 2002. 1.1

[45] Daniel A. Steck. Cesium d line data, 2008. 1.1

[46] Rudolf Grimm, Matthias Weidemüller, and Yurii B. Ovchinnikov. Optical dipole traps for neutral atoms. *Advances In Atomic, Molecular, and Optical Physics*, 42:95, 2000. 1.1, 1.2.1

[47] Florian Grenz. *Ein System zur entarteten Raman-Seitenbandkhlung einzelner Cäsium-Atome*. Diplomarbeit, Universität Bonn, 2008. 1.1

[48] Wolfgang Alt. An objective lens for efficient fluorescence detection of single atoms. *Optik - International Journal for Light and Electron Optics*, 113(3):142–144, 2002. 1.1

[49] Arne Härter. *Ein Aufbau zur kohrenten Manipulation und zum zustandsabhngigen Transport einzelner Atome*. Diplomarbeit, Universität Bonn, 2007. 1.1, 1.2.2

[50] Marshall T. DePue, Colin McCormick, S. Lukman Winoto, Steven Oliver, and David S. Weiss. Unity occupation of sites in a 3D optical lattice. *Physical Review Letters*, 82(11):2262, March 1999. 1.1.1

[51] Wolfgang Alt, Dominik Schrader, Stefan Kuhr, Martin Müller, Victor Gomer, and Dieter Meschede. Single atoms in a standing-wave dipole trap. *Physical Review A*, 67(3):033403, March 2003. 1.1.1, 4.1

[52] Leslie C. Allen and Joseph H. Eberly. *Optical Resonance and Two-Level Atoms*. Dover Pubn Inc, new edition edition, December 1988. 1.1.2, 1.1.2

[53] Bruce W. Shore. *The Theory of Coherent Atomic Excitation, Multilevel Atoms and Incoherence (Theory of Coherent Atomic Excitation Vol. 2)*, volume 2. Wiley-Interscience, 1990. 1.1.2, 3.1.2, 3.1.2

[54] Claude Cohen-Tannoudji, Jacques Dupont-Roc, and Gilbert Grynberg. *Atom-Photon Interactions: Basic Processes and Applications*. Wiley-VCH, March 1998. 1.1.2, 1.1.2, 2.1, 2.2.2, 2.2.2, 3.1.2

[55] W. Happer and B. S. Mathur. Effective operator formalism in optical pumping. *Physical Review*, 163(1):12, November 1967. 1.2.1

[56] P.S. Jessen and I.H. Deutsch. Optical lattices. *Advances in Atomic, Molecular and Optical Physics*, 37:95, 1996. 1.2.1, 2.2.1

[57] P. Rosenbusch, S. Ghezali, V. A. Dzuba, V. V. Flambaum, K. Beloy, and A. Derevianko. ac stark shift of the cs microwave atomic clock transitions. *Physical Review A (Atomic, Molecular, and Optical Physics)*, 79(1):013404–8, 2009. 1.2.1, 2.1.2, 2.4

[58] Daniel Döhring. *Ein Experiment zum zustandsabhngigen Transport einzelner Atome*. Diplomarbeit, Universität Bonn, 2007. 1.2.1

[59] Jai Min Choi and D. Cho. Elimination of inhomogeneous broadening for a ground-state hyperfine transition in an optical trap. *Journal of Physics: Conference Series*, 80:012037, 2007. 1.2.2

[60] M. Abarkan, J.P. Salvestrini, M.D. Fontana, and M. Aillerie. Frequency and wavelength dependences of electro-optic coefficients in inorganic crystals. *Applied Physics B: Lasers and Optics*, 76(7):765–769, July 2003. 1.2.2

[61] Wolfgang Ketterle, N.J. Van Druten, Benjamin Bederson, and Herbert Walther. Evaporative cooling of trapped atoms. *Advances In Atomic, Molecular, and Optical Physics*, 37:181, 1996. 2

[62] G. Modugno, G. Ferrari, G. Roati, R. J. Brecha, A. Simoni, and M. Inguscio. Bose-einstein condensation of potassium atoms by sympathetic cooling. *Science*, 294(5545):1320–1322, November 2001. 2

[63] O. Zobay and B. M. Garraway. Two-dimensional atom trapping in field-induced adiabatic potentials. *Physical Review Letters*, 86(7):1195, February 2001. 2

[64] N. Lundblad, P. J. Lee, I. B. Spielman, B. L. Brown, W. D. Phillips, and J. V. Porto. Atoms in a radio-frequency-dressed optical lattice. *Physical Review Letters*, 100(15):150401–4, April 2008. 2

[65] T. Schumm, S. Hofferberth, L. M. Andersson, S. Wildermuth, S. Groth, I. Bar-Joseph, J. Schmiedmayer, and P. Kruger. Matter-wave interferometry in a double well on an atom chip. *Nat Phys*, 1(1):57–62, October 2005. 2

[66] Pascal Bohi, Max F. Riedel, Johannes Hoffrogge, Jakob Reichel, Theodor W. Hnsch, and Philipp Treutlein. Coherent manipulation of Bose-Einstein condensates with state-dependent microwave potentials on an atom chip. *Nat Phys*, 5(8):592–597, 2009. 2

[67] D. J. Wineland and Wayne M. Itano. Laser cooling of atoms. *Physical Review A*, 20(4):1521, October 1979. 2, 2.1, 2.1, 2.1.1, 2.1.1, 3.1.1, 3.1.2

[68] D. Leibfried, D.M. Meekhof, C. Monroe, B.E. King, W.M.Itano, and D.J.Wineland. Experimental preparation and measurement of quantum states of motion of a trapped atom. *Journal of Modern Optics*, 44:2485–2505, November 1997. 2, 2.1, 4.1

[69] R. Blatt, J. I. Cirac, and P. Zoller. Trapping states of motion with cold ions. *Physical Review A*, 52(1):518, July 1995. 2, 2.1

[70] M. Morinaga, I. Bouchoule, J.-C. Karam, and C. Salomon. Manipulation of motional quantum states of neutral atoms. *Physical Review Letters*, 83(20):4037, November 1999. 2

[71] I. B. Spielman, P. R. Johnson, J. H. Huckans, C. D. Fertig, S. L. Rolston, W. D. Phillips, and J. V. Porto. Collisional deexcitation in a quasi-two-dimensional degenerate bosonic gas. *Physical Review A*, 73(2):020702, February 2006. 2

[72] Torben Müller, Simon Fölling, Artur Widera, and Immanuel Bloch. State preparation and dynamics of ultracold atoms in higher lattice orbitals. *Physical Review Letters*, 99(20):200405, November 2007. 2

[73] P. Carruthers and M. M. Nieto. Coherent states and the forced quantum oscillator. *American Journal of Physics*, 33(7):537–544, July 1965. 2, 2.1.2

[74] M. C. Fischer, K. W. Madison, Qian Niu, and M. G. Raizen. Observation of rabi oscillations between bloch bands in an optical potential. *Physical Review A*, 58(4):R2648, October 1998. 2, 2.1.2

[75] Marco Anderlini, Jennifer Sebby-Strabley, Jens Kruse, James V. Porto, and William D. Phillips. Controlled atom dynamics in a double-well optical lattice. *Journal of Physics B: Atomic, Molecular and Optical Physics*, 39(10):S199–S210, 2006. 2

[76] Cheng Chin. *Cooling, collisions and coherence of cold cesium atoms in a trap*. PhD thesis, Stanford University, 2001. 2, 3.1.2

[77] M. Johanning, A. Braun, N. Timoney, V. Elman, W. Neuhauser, and Chr. Wunderlich. Individual addressing of trapped ions and coupling of motional and spin states using rf radiation. *Physical Review Letters*, 102(7):073004–4, February 2009. 2, 2.1.1, 2.4

[78] Worawarong Rakreungdet. *Quantum information science with netural atoms*. PhD thesis, The University of Arizona, 2008. 2, 2.5.2

[79] Edward Condon. A theory of intensity distribution in band systems. *Physical Review*, 28(6):1182, December 1926. 2.1

[80] M. Born and R. Oppenheimer. Zur quantentheorie der molekeln. *Annalen der Physik*, 389(20):457–484, 1927. 2.1

[81] I. Marzoli, J. Cirac, R. Blatt, and P. Zoller. Laser cooling of trapped three-level ions: Designing two-level systems for sideband cooling. *Physical Review A*, 49(4):2771–2779, 1994. 2.1, 3.1.1, 3.1.2

[82] Wolfgang P. Schleich. *Quantum Optics in Phase Space*. Wiley-VCH, illustrated edition edition, March 2001. 2.1.1

[83] Jia-Lin Chang. A new formula to calculate Franck-Condon factors for displaced and distorted harmonic oscillators. *Journal of Molecular Spectroscopy*, 232(1):102–104, July 2005. 2.1.1

[84] D. Leibfried, B. DeMarco, V. Meyer, M. Rowe, A. Ben-Kish, J. Britton, W. M. Itano, B. Jelenkovi, C. Langer, T. Rosenband, and D. J. Wineland. Trapped-Ion quantum simulator: Experimental application to nonlinear interferometers. *Physical Review Letters*, 89(24):247901, November 2002. 2.1.1, 2.5.2, 4, 4.2.1

[85] M. E. Gehm, K. M. OHara, T. A. Savard, and J. E. Thomas. Dynamics of noise-induced heating in atom traps. *Physical Review A*, 58(5):3914, November 1998. 2.1.2

[86] T. A. Savard, K. M. OHara, and J. E. Thomas. Laser-noise-induced heating in far-off resonance optical traps. *Physical Review A*, 56(2):R1095, 1997. 2.1.2

[87] S. Wilkinson, C. Bharucha, K. Madison, Qian Niu, and M. Raizen. Observation of atomic Wannier-Stark ladders in an accelerating optical potential. *Physical Review Letters*, 76(24):4512–4515, 1996. 2.1.2

[88] A. Alberti, G. Ferrari, V. V Ivanov, M. L Chiofalo, and G. M Tino. Coherent transport of atomic wave packets in amplitude-modulated vertical optical lattices. *0903.0724*, March 2009. 2.1.2

[89] H. Schmitz, R. Matjeschk, Ch. Schneider, J. Glueckert, M. Enderlein, T. Huber, and T. Schaetz. Quantum walk of a trapped ion in phase space. *Physical Review Letters*, 103(9):090504, 2009. 2.1.2, 4.1

[90] Charles Kittel. *Einführung in die Festkörperphysik*. Oldenbourg Wissensch.Vlg, September 2002. 2.2.1, 2.2.1

[91] Neil W. Ashcroft and David N. Mermin. *Festkörperphysik*. Oldenbourg, June 2007. 2.2.1, 2.2.1

[92] Markus Greiner. *Ultracold quantum gases in three-dimensional optical lattice potentials*. PhD thesis, Ludwig-Maximilians-Universität München, 2003. 2.2.1

[93] D. L. Haycock, P. M. Alsing, I. H. Deutsch, J. Grondalski, and P. S. Jessen. Mesoscopic quantum coherence in an optical lattice. *Physical Review Letters*, 85(16):3365, October 2000. 2.2.1

[94] C. Monroe, D. M. Meekhof, B. E. King, W. M. Itano, and D. J. Wineland. Demonstration of a fundamental quantum logic gate. *Physical Review Letters*, 75(25):4714, December 1995. 2.5.2, 4

[95] D. Leibfried, D. M. Meekhof, B. E. King, C. Monroe, W. M. Itano, and D. J. Wineland. Experimental determination of the motional quantum state of a trapped atom. *Physical Review Letters*, 77(21):4281, November 1996. 2.5.2, 4.1

[96] L. F. Wei, Yu xi Liu, and Franco Nori. Engineering quantum pure states of a trapped cold ion beyond the Lamb-Dicke limit. *Physical Review A*, 70(6):063801, December 2004. 2.5.2, 4.2.1, 4.2.1

[97] Ren Stock, Ivan Deutsch, and Eric Bolda. Quantum state control via Trap-Induced shape resonance in ultracold atomic collisions. *Physical Review Letters*, 91(18):183201, 2003. 2.5.2

[98] Jrgen Eschner, Giovanna Morigi, Ferdinand Schmidt-Kaler, and Rainer Blatt. Laser cooling of trapped ions. *Journal of the Optical Society of America B*, 20(5):1003–1015, May 2003. 3

[99] F. Diedrich, J. C. Bergquist, Wayne M. Itano, and D. J. Wineland. Laser cooling to the zero-point energy of motion. *Physical Review Letters*, 62(4):403, 1989. 3

[100] A. Schliesser, R. Riviere, G. Anetsberger, O. Arcizet, and T. J. Kippenberg. Resolved-sideband cooling of a micromechanical oscillator. *Nat Phys*, 4(5):415–419, May 2008. 3, 3.1.2

[101] Ch. Roos, Th. Zeiger, H. Rohde, H. C. Ngerl, J. Eschner, D. Leibfried, F. Schmidt-Kaler, and R. Blatt. Quantum state engineering on an optical transition and decoherence in a paul trap. *Physical Review Letters*, 83(23):4713, December 1999. 3

[102] David E. Pritchard. Cooling neutral atoms in a magnetic trap for precision spectroscopy. *Physical Review Letters*, 51(15):1336, October 1983. 3, 3.1.2

[103] J. Janis, M. Banks, and N. P. Bigelow. rf-induced sisyphus cooling in a magnetic trap. *Physical Review A*, 71(1):013422, 2005. 3, 3.1.2

[104] Christof Wunderlich, Giovanna Morigi, and Dirk Rei. Simultaneous cooling of axial vibrational modes in a linear ion trap. *Physical Review A*, 72(2):023421, 2005. 3

[105] Kurt W. Miller, Stephan Drr, and Carl E. Wieman. rf-induced sisyphus cooling in an optical dipole trap. *Physical Review A*, 66(2):023406, 2002. 3, 3.1.2

[106] Stig Stenholm. The semiclassical theory of laser cooling. *Reviews of Modern Physics*, 58(3):699, July 1986. 3.1.1, 3.1.2

[107] C. Monroe, D. M. Meekhof, B. E. King, S. R. Jefferts, W. M. Itano, D. J. Wineland, and P. Gould. Resolved-Sideband raman cooling of a bound atom to the 3D Zero-Point energy. *Physical Review Letters*, 75(22):4011, November 1995. 3.1.1, 3.1.2

[108] J. Javanainen, M. Lindberg, and S. Stenholm. Laser cooling of trapped ions: dynamics of the final stages. *Journal of the Optical Society of America B*, 1(1):111–115, March 1984. 3.1.2, 3.1.2

[109] R. L. de Matos Filho and W. Vogel. Second-sideband laser cooling and nonclassical motion of trapped ions. *Physical Review A*, 50(3):R1988, 1994. 3.1.2

[110] E. Peik, J. Abel, Th. Becker, J. von Zanthier, and H. Walther. Sideband cooling of ions in radio-frequency traps. *Physical Review A*, 60(1):439, July 1999. 3.1.2

[111] Vladan Vuletić, Cheng Chin, Andrew J. Kerman, and Steven Chu. Degenerate raman sideband cooling of trapped cesium atoms at very high atomic densities. *Physical Review Letters*, 81(26):5768, December 1998. 3.1.2

[112] Tai Hyun Yoon, Sergei A. Pulkin, Jong Rak Park, Myung Sai Chung, and Hai-Woong Lee. Theoretical analysis of resonances in the polarization spectrum of a two-level atom driven by a polychromatic field. *Physical Review A*, 60(1):605, July 1999. 3.1.2

[113] G. Morigi, J. I. Cirac, M. Lewenstein, and P. Zoller. Ground-state laser cooling beyond the Lamb-Dicke limit. *EPL (Europhysics Letters)*, 39(1):13–18, 1997. 3.1.2

[114] G. Morigi, J. Eschner, J. I. Cirac, and P. Zoller. Laser cooling of two trapped ions: Sideband cooling beyond the Lamb-Dicke limit. *Physical Review A*, 59(5):3797, May 1999. 3.1.2

[115] Peng Xue, Barry C. Sanders, and Dietrich Leibfried. Quantum walk on a line for a trapped ion. *Physical Review Letters*, 103(18):183602, October 2009. 4.1

[116] R. L. de Matos Filho and W. Vogel. Quantum nondemolition measurement of the motional energy of a trapped atom. *Physical Review Letters*, 76(24):4520, June 1996. 4.2

[117] D. S. Weiss, J. Vala, A. V. Thapliyal, S. Myrgren, U. Vazirani, and K. B. Whaley. Another way to approach zero entropy for a finite system of atoms. *Physical Review A*, 70(4):040302, October 2004. 5.1